UILU-ENG 85-3605

Report No. 121

PROPORTIONAL AND NON-PROPORTIONAL BIAXIAL FATIGUE OF INCONEL 718

by

Justin Lee Koch
Materials and Design Division
Department of Mechanical and Industrial Engineering

A Report of the

MATERIALS ENGINEERING - MECHANICAL BEHAVIOR

College of Engineering, University of Illinois at Urbana-Champaign

July 1985

ABSTRACT

A multiaxial LCF (low cycle fatigue) parameter is proposed for materials that fail in a shear strain dominated mode. Three bulk loading parameters have been identified to assess fatigue damage--maximum shear strain amplitude, and both the strain amplitude and mean stress normal to the plane of maximum shear strain amplitude.

Biaxial strain controlled tests were conducted on thin walled tubular specimens of Inconel 718 at room temperature. Forty-six specimens were tested at fatigue lives of less than 10^5 cycles. Fifteen loading paths were employed to systematically identify the critical fatigue damage parameters. Proportional, non-proportional, and out-of-phase loading cases were considered. Selection of strain paths and damage parameters were dictated by extensive observations of the cracking behavior. Shear crack initiation and growth dominated the fatigue damage process. Fatigue lives were correlated by the proposed damage parameter to within a factor of two.

ACKNOWLEDGMENTS

Dr. Peter Kurath is gratefully acknowledged for both the quality and quantity of time invested in this investigation. Dr. Darrell F. Socie, my advisor, is acknowledged for his superb experimental insight and technical guidance. Dr. James W. Fash is thanked for his patience, insights, and answers to unending questions, while he labored feverishly on his own thesis.

The Department of Mechanical and Industrial Engineering Publications Office, particularly June Kempka and Tammy Lawhead, are gratefully acknowledged for aiding in the preparation of this manuscript. Suzanne Palmer's graphics expertise was invaluable in the preparation of the document.

Finally, my friends, Jess Comer, Julie Barrantine, Tom Fugger, and Gary Marquis are especially thanked for both the academic and moral support they gave.

TABLE OF CONTENTS

LIST OF TABLES

Page

Table

LIST OF FIGURES

LIST OF SYMBOLS

A'	Cyclic torsional strength coefficient
b	Fatigue strength exponent
c	Fatigue ductility exponent
E	Linear elastic modulus
G	Shear modulus
K, K'	Monotonic, cyclic axial strength coefficient
k	Biaxial material property
S	Biaxial material property
$2N_f, N_f$	Number of reversals, cycles to failure
$2N_{1.0}, 2N_{0.1}$	Number of reversals to 1.0 mm, 0.1 mm crack length
n, n'	Monotonic, cyclic strain hardening exponent
α	Biaxial material property
$\hat{\gamma}$	Maximum shear strain amplitude
$\hat{\gamma}_p$	Maximum plastic shear strain amplitude
γ_f'	Torsional fatigue shear ductility coefficient
γ'	Maximum shear strain at any point along the loading path
γ^*	Maximum shear strain into specimen surface
γ_{max}	Maximum shear strain experienced during a complete load cycle
ε	Applied axial strain
ε	Von Mises effective strain
$\hat{\varepsilon}_n$	Strain amplitude normal to the plane of maximum shear strain amplitude
$\hat{\varepsilon}_{np}$	Plastic strain amplitude normal to the plane of maximum shear strain amplitude
ε_f'	Fatigue ductility coefficient
ε^*	Strain amplitude normal to the γ^* plane

$\varepsilon_1, \varepsilon_2, \varepsilon_3$	Principle strains
θ	Angle between a shear direction and the plane normal to the specimen axis
λ	Strain ratio, shear strain amplitude/axial strain amplitude
σ'_f	Fatigue strength coefficient
σ_{no}	Mean stress normal to the plane of maximum shear strain amplitude
τ'_f	Torsional fatigue shear strength coefficient
Φ	Phase difference between axial and torsional strain maximums

1. INTRODUCTION

Fatigue damage evaluation of components is a design consideration within the manufacturing industry today. A portion of a typical design cycle is shown in Fig. 1. The critical location(s) on a component is/are often subject to three-dimensional stress-strain states. Numerical methods may be employed in the analysis of the complex deformation response. Advances in both computer software and hardware technology offer a promising future for this type of analysis. Finite fatigue life estimation procedures being developed employ the results of deformation modeling to predict the expected longevity of the component. Current multiaxial fatigue models are unable to accurately predict fatigue life for any given strain path and material. Experimental results from select biaxial strain paths have aided in the identification of the proper damage parameter for a given material.

1.1 Background

Early fatigue design focused exclusively on the elastic, infinite life region. Experimental testing was performed entirely with uniaxial stress controlled specimens. Results were compiled in the form of stress-life (S-N) curves and/or Goodman diagrams. Emphasis was placed on determining the fatigue limit (the value of stress below which a material would not fail). Early multiaxial research attempted to employ stress controlled uniaxial specimen data to predict the fatigue life of more realistic states of stress. Extensions of static yield theories, such as maximum shear stress (i.e., Tresca and Von Mises) were employed when analyzing "ductile" materials. The maximum principle stress formulation was used for "brittle" materials. A review of these and additional theories can be found in [1-3].*

Correlation of plastic strain with fatigue behavior was first introduced by Coffin [4] and Manson [5]. They established a linear relationship between fatigue life and plastic strain with log-log coordinates. This relationship opened the field of finite-life or low cycle fatigue (LCF) design. As technology progressed, testing was conducted in strain control and data compiled as strain-life (ϵ - N_f) diagrams. Correspondingly, initial multiaxial theories were modified from previous stress-based models to strain-based equivalents. No generally accepted model was found that could correlate data for all strain states and materials. Few models were formulated to reflect a physical damage mechanism.

The fatigue damage process is often divided into two phases: "initiation" and "propagation". Initiation is a process of repeated slip on crystallographic planes that coincide with the plane of maximum shear strain, resulting in the formation of slip bands. Ewing and Humphrey [6] observed that under repeated loading, intrusions and extrusions formed at these slip bands. Forsyth [7] referred to this phenomenon as stage I crack growth. Fatigue crack propagation has been observed to occur in one of two modes: (1) crack extension on planes of maximum shear strain or (2) crack growth on planes normal to maximum principle strain (Mode I direction). Forsyth [7] viewed the Mode I extension as stage II crack growth. Fracture mechanics concepts are often employed

---

*Numbers in brackets refer to entries in REFERENCES.

to estimate the crack growth behavior (i.e., propagation) for a given nominal loading. When calculating the total fatigue life, Miller [8] proposed the elimination of the crack initiation life altogether. Several researchers [9-11] investigated the demarcation between initiation and propagation. No constant crack length was identified for any material and/or geometry. The crack length identified was often employed as a starting point for fracture mechanics analysis. Different materials and strain levels exhibit various combinations of these types of fatigue crack formation and growth.

1.2 Purpose and Scope

Correlation of physical mechanisms should coincide with development of fatigue damage models. To this end, fatigue crack growth on the outer specimen surface was employed in this research to characterize overall fatigue damage. Inconel 718, a material displaying shear dominated crack growth at the strain amplitudes under investigation, was chosen for further study. A damage parameter based on bulk stress-strain response was identified. Based on the direction of surface crack growth, shear deformation was selected as the primary damage variable. Experimental strain paths were chosen to identify the form of secondary non-shear terms in the damage parameter. The strain paths chosen included proportional, non-proportional, and out-of-phase loadings to simulate anticipated design conditions.

2. EXPERIMENTAL PROGRAM

2.1 Material and Equipment

Inconel 718, a nickel based superalloy strengthened by γ' and γ'' precipitates (precipitate size ~ 300 400Å), was the material employed in the testing program. Chemical composition and heat treatment for the alloy under consideration are reported in Table 1. Tubular specimens were machined from sections of a forged ring. Specimen axes coincided with the longitudinal direction of the ring. Metallographic examination of the microstructure revealed grain size diameters ranging from 0.01 mm to 0.2 mm. The tube specimen design (Fig. 2) was dictated by the desire to allow a minimum of 10 grains through the wall thickness. Radial, tangential, and longitudinal microstructural isotropy was inferred from Fig. 3 (inverted glycergia etchant; 5 · Hcl, 1 · glycerol, 1 · HNO_3). Small uniaxial fatigue specimens were machined from both the longitudinal and radial directions of the forged ring. Testing of these specimens revealed no substantial difference in fatigue lives for similar strain amplitudes [12]. Therefore, no preferred orientation for damage was anticipated during the biaxial testing. Baseline material properties for IN 718 are presented in Table 2.

A stiffened MTS 806 tension-torsion test frame was utilized to conduct strain-controlled biaxial tests. Control signal generation and data acquisition were accomplished with an MTS 463 processor-interface that coupled the analog signal conditioners to a PDP 11/23 computer.

2.2 Surface Crack Growth Observation

Formation and growth of fatigue cracks have often been observed on the surface of fatigue specimens. Data to investigate these phenomena were obtained by acetate tape replication of the specimen surface at regular intervals during the fatigue life. A 0.3μ specimen surface finish eliminated confusion between fatigue cracks and machining marks. The use of an internal extensometer left the outside of the specimen gauge section unencumbered, facilitating the replication procedure. Specific details of this acetate tape replication procedure are given by Fash [13].

2.3 Testing Program

Fifteen strain paths (Fig. 4) comprise the test program for this investigation. Fatigue lives for tests conducted are presented in Table 3. Strain paths A through G are proportional, Paths H-I are non-proportional, and Paths M-O are non-proportional out-of-phase loadings. A more thorough discussion of these paths follows in a subsequent section.

Effective strain amplitudes, $\bar{\varepsilon}$, of 0.005 and 0.01 were arbitrarily chosen to set test control limits. The choice of this variable should not be misconstrued to indicate an adequate damage parameter, rather a convenient method by which to base initial testing levels.

3. ANALYSIS

3.1 Development of a Shear Damage Parameter

Shear dominated LCF crack growth has been observed for the material under consideration [14]. Tresca's formulation of maximum shear stress was one possible extension of static yield theories that could correlate shear crack growth. Fatigue damage predicted by this bulk parameter was anticipated to occur on planes of maximum shear stress. An additional non-shear term was needed to model the differences in shear crack growth due to a stress normal to the maximum shear stress plane. Nadai [15] quoted Mohr: "The shearing stress, S_s, in the planes of slip reaches, at the limit, a maximum value dependent on the normal stress, S_n, in the same planes." Findley [16] later stated, "The principle stress (maximum shear stress) theory modified by the influence of the complimentary normal stress may be the most satisfying theory for combined stress fatigue." Similar arguments have been forwarded by Orowan [17] with regard to dislocation motion. As previously discussed, plastic deformation occurring during fatigue induced a conversion from stress-based models to strain-based equivalents. Tresca's formulation modified to a strain-based approach in conjunction with a uniaxial strain life damage criteria, was:

$$\Delta\gamma_{max}/2 = 1.5\ \varepsilon_f' \ (2N_f)^c + \frac{1.3\ \sigma_f'}{E}\ (2N_f)^b. \qquad (1)$$

Brown and Miller classified shear cracks to be one of two types, denoted A and B, and developed a strain-based equivalent of Mohr's original stress-based formulation for type A cracks [2]. In a subsequent paper, Kandil, Brown, and Miller [18] refined the model to the following form

$$\hat{\gamma}^{\alpha} + S\,\hat{\varepsilon}_n^{\alpha} = \text{constant} \tag{2}$$

with

$$\hat{\gamma} = \frac{\Delta(\varepsilon_1 - \varepsilon_3)}{2} \text{ and; } \hat{\varepsilon}_n = \frac{\Delta(\varepsilon_1 + \varepsilon_3)}{2} \tag{3}$$

where S and α are material constants. The term $\hat{\varepsilon}_n$ reflects the strain normal to the maximum shear strain amplitude ($\hat{\gamma}$) direction on which crack growth is anticipated. Lohr and Ellison [19] proposed that the critical shear plane for structural applications was into the specimen surface (i.e. type B cracks). A damage parameter in a similar format to that forwarded by Brown and Miller resulted.

$$\gamma^{*} + k\varepsilon_n^{*} = \text{constant} \tag{4}$$

and

$$\gamma^{*} = \frac{\Delta(\varepsilon_1 - \varepsilon_2)}{2} \quad \text{and} \quad \varepsilon_n^{*} = \frac{\Delta(\varepsilon_1 - \varepsilon_2)}{2} \tag{5}$$

Strains normal to the critical shear direction identified by Lohr and Ellison were incorporated into the damage formulation via the ε_n^{*} term. These latter two theories are discussed in APPENDIX A, with regard to anticipated crack growth directions for the tubular specimen (Fig. 2).

3.2 Proposed Shear Damage Parameter

Based on crack growth observations, Socie, et al. [20], combined the Brown and Miller parameter with the Coffin-Manson equation to estimate fatigue lives. The constants α and S in Eq. (2) were taken to be unity. A mean stress modification to Brown and Miller's formulation was introduced, considering only the plastic strain components of the deformation. This resulted in the following form [21]:

$$\hat{\gamma}_p + \hat{\varepsilon}_{np} + \sigma_{no}/E = 1.75\ \varepsilon_f'(2N_f)^c. \qquad (6)$$

The equation was subsequently modified to correlate with total strain torsional data:

$$\hat{\gamma} + \hat{\varepsilon}_n + \sigma_{no}/E = \gamma_f'(2N_f)^c + \frac{\tau_f'}{G}(2N_f)^b. \qquad (7)$$

Material constants on the right hand side of Eq. (7) were generated from fully reversed torsion tests. Determination of whether the terms on the left hand side of Eq. (7) are amplitude or maximum stress-strain quantities remains to be clarified.

Three bulk shear quantities may be employed to characterize fatigue damage:

(1) γ', the maximum shear strain at an arbitrary "snap-shot" point along the load path;

(2) γ_{max}, the maximum shear strain encountered over the entire load path; and

(3) the shear strain amplitude experienced by a specific plane over the entire load path, designating the $\hat{\gamma}$ plane as the maximum.

To illustrate the three quantities, Mohr's strain circle is examined for two torsional strain paths, B ($R_\gamma = -1$) and E ($R_\gamma = 0$), in Fig. 5. The maximum shear strain, γ_{max}, represented by the largest radius of Mohr's circle, is twice as large for path E as for path B considering identical applied shear strain ranges. Shear strain amplitudes, $\hat{\gamma}$, however, are identical for both paths. It should be noted that these two representations $\hat{\gamma}$ and γ_{max}, are equivalent for fully reversed loading. Sines [22] inferred that mean torsional strains should have little influence on the fatigue performance of ductile materials. Therefore, $\hat{\gamma}$, the maximum shear strain amplitude, was chosen as a representative damage parameter.

For proportional loading, the direction of γ_{max} and $\hat{\gamma}$ are coincident for the entire strain excursion. Proportional loadings correspond to the expansion and contraction of Mohr's circle about a given point as the strain path is traversed in time. (Note: a proportional strain path is both linear in ε-γ space and passes through the strain-space origin).

For non-proportional loading, the γ' planes are continually changing orientation with regard to the specimen axis. Orientation and movement of these planes are further illustrated by analyzing the non-proportional linear strain path J (Fig. 6). Path J includes an initial axial offset strain equal to half the axial strain amplitude, then an in-phase cyclic excursion with $\lambda = (3)^{1/2}$. (Note: The initial axial offset strain causes this path to be non-proportional.) For non-proportional strain paths, the ratio of axial and torsional strain of different snapshot points will not be a constant. However, λ is defined as the ratio of the respective amplitudes. Mohr's circle for strain is employed to illustrate strain state "snapshots" for eight points during the cyclic loading. An infinitesimal element of the tubular specimen is considered with the positive x-face being parallel to the specimen axis. The maximum shear strain, γ', for each of these snapshot strain points is illustrated in Fig. 6. Continual movement of the γ' plane is noted. (This occurs for any non-proportional strain path when applied strains are cyclic). Figure 7 illustrates a similar sequence for a 90° out-of-phase loading (also a non-proportional loading). Mohr's circle analysis was adequate for these simple illustrations. The maximum value of γ' experienced during the strain cycle is designated γ_{max}. During a loading cycle all planes are monitored for changes in γ', with the $\hat{\gamma}$ direction being the plane of maximum shear strain alternation. Tensor notation (see APPENDIX B) was employed to identify both magnitude and direction for the $\hat{\gamma}$ and γ_{max} planes.

In light of the strain paths utilized in this investigation, the proportional paths A-G had stationary γ' planes with the $\hat{\gamma}$ and γ_{max} planes being coincident. Non-proportional, linear paths H-J experienced changing orientation of the γ' planes, with the $\hat{\gamma}$ and γ_{max} planes coincident only for paths H, I, K, and L. Non-proportional out-of-phase paths M-O also experienced changing orientation of γ' planes; however, paths M and N exhibited coincident $\hat{\gamma}$ and γ_{max} planes.

4. RESULTS AND DISCUSSION

4.1 Biaxial Strain Path Selection

Selection of fifteen strain paths was a continuous process, based on results from prior testing. As the investigation progressed, physical characteristics of crack growth were evaluated in light of the known stress/strain states to identify additional critical strain paths. Some critical tests were proposed to isolate one variable from Eq. (7) at a time.

Cracking characteristics and other biaxial material baseline data were obtained from fully-reversed proportional paths A through C. Torsion tests (path B) provided data where the maximum shear strain amplitude planes had zero normal strains and stresses. Crack formation and growth were observed on $\hat{\gamma}$ planes [14]. This test allowed evaluation of the biaxial damage criteria (Eq. (7)) without consideration of non-shear terms. Fully reversed tension tests (path A) were employed to observe correlation between thin wall tubes and uniaxial smooth specimens. Again, nearly all fatigue crack growth (i.e. majority of fatigue life) was observed on $\hat{\gamma}$ planes [14]. Strains normal to the $\hat{\gamma}$ plane were present for these tests, and the $\hat{\varepsilon}_n$ term of Eq. (7) allowed correlation with previous torsional data. Proportional combined tension-torsion tests with $\lambda = (3)^{1/2}$ (path C) followed as the simplest combination of paths A and B. These tests further established the crack growth direction as occurring on planes of maximum shear strain amplitude.

Further investigation of non-shear effects was accomplished with proportional mean strain paths D and F. The mean stress term of Eq. (7) was isolated for study. Directions and magnitudes of $\hat{\gamma}$ and $\hat{\varepsilon}_n$ were not altered by the mean strains, allowing comparison with paths A and C. Effects of different mean strains and stresses were evaluated through simple modifications of path C. Paths G-J had identical axial and torsional strain amplitudes, and $\lambda = (3)^{1/2}$. These tests strengthened the confidence in the form of non-shear terms in Eq. (7). Crack growth for these mean stress and strain paths was in the $\hat{\gamma}$ direction [21].

In the current investigation, five additional strain paths (L through O) were introduced. Paths K and L were employed to identify the form of the normal strain term, $\hat{\varepsilon}_n$. If $\hat{\varepsilon}_n$ was an amplitude term, damage predicted from static axial strains would be zero. Mean stresses due to mean strains resulted on the 0° plane (normal to the specimen axis), but were zero on the 90° plane. Out-of-phase paths M-O were employed to evaluate time-dependent interaction of the proposed parameters. Rotating γ' planes with respect to specimen orientation (Fig. 7) would result in non-zero values of shear strain for all planes. However, two perpendicular $\hat{\gamma}$ planes were always preferred for long crack growth. Because all planes experienced shear deformation to some degree, the role of non-shear terms became more significant.

4.2 Cracking Characteristics

Two characteristics of fatigue cracks, direction and growth rate, were evaluated in this investigation. Fatigue crack initiation and growth were observed to occur on or near planes of maximum shear strain amplitude ($\hat{\gamma}$). Only tension tests displayed stage II behavior late in the fatigue life [14,23]. This deviation in crack direction accounted for approximately 5 percent of the 1.0 mm fatigue life, and is considered to be insignificant for this material at the strain ranges investigated. Typical directions of fatigue crack surface growth for all 15 strain paths are illustrated in APPENDIX C. Polar plots were employed to illustrate the amount of shear strain amplitude for each plane, and $\hat{\gamma}$ was designated as the maximum. Orientation of the polar plots and micrographs with regard to the specimen axis coincide.

Crack growth for fully reversed proportional paths A-C occurred on both $\hat{\gamma}$ planes. Mean strain, proportional paths D-F demonstrated fatigue crack growth behavior similar to paths A-C, differing only by preferred crack growth on the $\hat{\gamma}$ plane with the larger non-shear terms of Eq. (7). Fatigue crack growth for non-proportional linear strain paths G-J followed suit closely with cracks growing near $\hat{\gamma}$ planes [21]. When both $\hat{\gamma}$ planes experienced tensile normal mean stresses (path J), the orientation with the larger mean stress experienced accelerated crack growth, in comparison to the cracks growing on the other $\hat{\gamma}$ plane. Conversely, when both planes experienced compressive normal mean stresses, (path G) crack growth was retarded. Crack growth on the plane with the least compressive mean stress was retarded to a lesser degree. Crack density for this case was much higher on both $\hat{\gamma}$ planes than for those tests with tensile mean stresses across the $\hat{\gamma}$ planes [21].

Fatigue cracks in torsion have been observed to form on both maximum shear planes and then propagate to failure on the plane parallel to the specimen axis (90° plane). The preference to the 90° plane may be due to a slight tensile mean hoop stress that is ignored in simple thin tube analysis. Torsion tests with a static axial strains, paths K-

L, demonstrated similar crack formation behavior. Fully reversed torsion (path B) and torsion with a static compressive mean stress (path B) displayed identical cracking direction. Late in the fatigue life of path K, which had a static axial stress, the crack that propagated to failure was on the $\hat{\gamma}$ plane normal to the specimen axis (0° plane). This behavior was attributed to the tensile normal mean stress across the 0° plane, whereas path L had a compressive mean stress across this plane. Figures 8 through 10 display the failure cracks for paths B, K and L.

Fatigue crack direction for the out-of-phase loadings M-O is shown in Figs. 11-14. For all cases, the cracks propagated on or near the $\hat{\gamma}$ plane experiencing the larger normal stresses and strains. Path M (Fig. 15) experienced tensile components of normal stress and strain on both $\hat{\gamma}$ planes but preferred the plane with the greater normal values. For paths N-O one of the $\hat{\gamma}$ plane coincides with $\theta = 0$. The 0° plane (normal to the specimen axis) experienced the entire applied axial strain and stress while the 90° plane (parallel to the specimen axis) experienced only a poissons strain and zero stress (due to plane stress assumption.) For path N at larger strain amplitudes (Fig. 16), many cracks formed early in the fatigue life, with no preferred direction. Upon reaching 0.1 mm, subsequent crack growth was preferred on planes 2° to 5° away from the 0° plane. At lower strain amplitudes (Fig. 17), nearly all cracks formed and propagated on the 0° plane. Crack density was an order of magnitude less for the smaller amplitude. Fatigue crack growth direction for path O (Fig. 18) was similar to the smaller amplitude case of path N. The greater mean stress on the 0° plane accelerated failure growth for path O, resulting in reduced fatigue life in comparison to a similar strain excursion for path N. Crack density for path O was less than that for path N at identical effective strain amplitudes (Fig. 19).

Growth of the failure cracks on maximum shear strain amplitude planes ($\hat{\gamma}$) versus the number of cycles (N) for all fifteen strain paths is reported in APPENDIX D. Similar effective strain amplitudes, $\bar{\varepsilon}$, were used to compare different strain paths. Previous investigations included similar comparisons between proportional paths A-F [14]. Subsequently, paths C, F, and G were contrasted with non-proportional linear paths H-J [21]. For completeness, a comparison of crack growth for all fifteen paths(A-O) was compiled in APPENDIX E. Only non-proportional paths conducted in this investigation (K-O) and pertinent reference to previous work are discussed.

Growth of the failure crack for imposed static axial strains (paths B, K, and L) is compared in Fig. 20. No systematic differences were identified. Stress states on the 90° plane (i.e. coincident with the specimen axis) were identical for paths B, K, and L (no imposed hoop stress). A tensile mean stress for path L on the 0° plane (i.e. normal to the specimen axis) was sufficient to switch the failure plane, but insufficient to cause noticeable difference in propagation. In other words, the $\hat{\gamma}$ plane with the most tensile normal stress was preferred for propagation. Second-order stress terms neglected in the stress deformation analysis may be responsible for the slight differences in crack growth between paths B and L.

Non-proportional out-of-phase paths M, N, and O were compared with combined tension-torsion paths C and J, respectively. Test results with identical axial and torsional strain amplitudes were employed for these comparisons, differing only by the phase angle (Φ).

Out-of-phase path M (Φ = 45°) is compared to the path C in Fig. 21. Initial crack growth increments were similar for both strain paths. At a crack length of approximately 0.2 mm, accelerated crack growth occurred for the out-of-phase tests. Mean stresses and strain amplitudes normal to the crack plane were deemed to be responsible for this behavior. In out-of-phase loading, the crack experienced a larger shear amplitude while the crack is being opened by normal strains and stresses. Fracture mechanics arguments support the notion that the normal stresses and strains become more significant with increasing crack length. Therefore, the differences in crack growth that became more evident at longer crack lengths (i.e. > 0.2 mm) were expected.

Out-of-phase strain path N (Φ = 90°) was also contrasted with proportional strain path C. Two amplitudes of applied axial and torsional strain are available for comparison (Figs. 22 and 23). Trends similar to those observed between paths M and C were noted at either amplitude. Arguments analogous to those previously forwarded were employed to explain the accelerated crack growth later in the fatigue lives. Due to the nature of the phase angle for path N, Φ = 90°, a greater shear strain amplitude was experienced by the failure crack plane while the crack was being opened by normal stresses and strains than for Φ = 45° tests (Path M). Damage characteristics were similar, only more severe for Path N.

Out-of-phase path O experienced even greater normal strains and mean stresses on the failure crack plane than did Path N. Comparisons with linear path J are shown in Fig. 24. Crack growth for path O closely matched path J. Path J experienced a damaging combination of shear strain with tensile normal strains and mean stresses, similar to path O. Therefore, the combination of shear excursion with a tensile strain and mean stress normal to the crack plane caused increased damage, not the out-of-phase loading. However, out-of-phase loadings are more conducive to the damaging situations responsible for this phenomena.

The increasing damage observed from path M through O is reflected by the accelerated crack growth shown in Fig. 25. Cracks for each path initiated in a similar fashion, but with increasing crack length; differences in the normal strains and stresses were manifested by accelerated crack propagation.

4.3 Life Prediction

An arbitrary crack length of 1.0 mm was employed as a reference to compare fatigue lives from all testing. Figures 26 and 27 contrast the scatter for both the 0.1 mm and 1.0 mm lives versus the maximum shear strain amplitude, $\hat{\gamma}$, respectively. Due to the cracking direction, the maximum shear strain amplitude should in a broad sense reflect the damage accumulation. Series 1 testing represents paths A-C, Series 2 for paths D-F, Series 3A and 3B for paths G-J, and Series 4 for paths K-O. Less scatter for the 1.0 mm life ($N_{1.0}$) than for the 0.1 mm life ($N_{0.1}$) resulted in subsequent damage correlations being made with a 1.0 mm crack length. The damage model (Eq. (7)) was employed to evaluate the experimental results. Total shear strain amplitude from fully reversed torsional tests (Path B) were employed to generate the baseline damage curve in Fig. 28. Baseline data were taken from strain path B because stresses and strains normal to the $\hat{\gamma}$ planes are zero. Elastic and plastic strains were fit by a least squares method to obtain material constants and then summed in a similar fashion to uniaxial ε-N_f diagrams. Total damage summed from each of the three terms of Eq. (7) was plotted versus the 1.0 mm fatigue life. The symbols employed in these figures for each test correspond to the designations for the different strain paths. The solid line in each of these figures represents the fully reversed torsional baseline data. Paths A-C are plotted in Fig. 29, Paths D-G in Fig. 30, Paths H-L in Fig. 31, and Paths M-O in Fig. 32. A comprehensive plot of all data is given in Fig. 33. Most tests demonstrated good correlation with this damage model. Exceptions included a systematic inability to account for large amounts of plasticity in out-of-phase tests (Path N).

Weighting for each of the three component parameters for the proposed damage model is illustrated with bar graphs in Figs. 34 and 35. The three components of Eq. (7), $\hat{\gamma}$, $\hat{\varepsilon}_n$, and σ_{no}/ε are represented by the uncrosshatched, single crosshatched, and double crosshatched section, respectively. Dominance of the $\hat{\gamma}$ component for most tests is evident. Out-of-phase paths M-O had larger $\hat{\varepsilon}_n$ values. Even more significant were the large mean stresses in Paths J and O, resulting in accelerated crack propagation.

A comprehensive view of the consistency of the damage parameter is seen in Fig. 36. Bar graphs are given for the ratio of N(actual)/N(predicted) for all paths. Ratios less than one represented non-conservative predictions. All fatigue lives were correlated to within a factor of two.

5. CONCLUSIONS

Fifteen strain paths were investigated employing thin wall tubes of Inconel 718. The low cycle fatigue behavior ($<10^5$ cycles) was examined with regard to physical damage mechanism and life prediction accuracy.

(1) Fatigue lives were dominated by crack formation and growth at the amplitudes under investigation.

(2) Cracking direction for the material and strain ranges under investigation occurred on the plane of maximum shear strain amplitude, $\hat{\gamma}$.

(3) The secondary terms of Eq. (7), $\hat{\varepsilon}_n$, and mean stress, σ_{no}, normal to the maximum shear amplitude, $\hat{\gamma}$, identified the preferred direction for crack propagation. This situation arose for strain paths where there were differences in $\hat{\varepsilon}_n$ and σ_{no} values between the two $\hat{\gamma}$ planes.

(4) The proposed damage parameter correlated the data for all the strain paths to within a factor of two. Constant amplitude fully reversed torsion tests (path B) were employed to generate the material constants for Eq. (7).

(5) The proposed damage parameter was consistently non-conservative for out-of-phase strain paths with large plastic strains.

Many materials exhibit a change in cracking direction for strain excursions resulting in high cycle fatigue. Also, cracking behavior dominates a smaller percentage of the total fatigue life for these loadings. Whether the proposed damage model is appropriate in this life regime remains to be verified. Longer life testing will also clarify whether material constants as proposed by Brown and Miller are needed for the secondary non-shear terms since they are anticipated to comprise a greater percentage of the damage quantity at longer fatigue lives. Since the least satisfying correlation of the data occurred for out of phase loadings, further investigation should be instigated to determine whether the model is appropriate for these paths.

Table 1 Chemical Composition and Heat Treatment, IN-718

a) Chemical Composition

Element	Actual	AMS 5663B min.		AMS 5663B max.
Carbon	0.034			0.08
Manganese	0.09			0.35
Silicon	0.06			0.35
Phosphorous	0.007(1)			0.015
Sulfur	0.001			0.015
Chromium	18.23	17.00	-	21.00
Nickel	52.12	50.00	-	55.00
Molybdenum	2.89	2.80	-	3.30
Columbium + Tantalum	5.03	4.75	-	5.50
Titanium	1.01	0.65	-	1.15
Aluminum	0.54	0.20	-	0.80
Cobalt	0.28			1.00
Boron	0.0035			0.006
Copper	0.05			0.30
Iron	19.48	remainder		

(1) included in Iron fraction

b) Heat Treatment

Solution tread at 968°C (1775°F) for 1 hr, oil quench; age at 832°C (1325°F) for 8 hr; furnace cool at 55°C (100°F) per hr to 635°C (1175°F); hold at 635°C (1175°F) for 8 hr + air cool.

Table 2 Baseline Material Properties, IN-718

Monotonic Tensile Properties

E,	Elastic Modulus	208,500 MPa
$\sigma_{y.2\%}$,	.2 Percent Offset Yield Strength	1,160 MPa
σ_u,	Ultimate Strength	1,420 MPa
σ_f,	True Fracture Strength	1,850 MPa
ε_f,	True Fracture Strain	.33
% RA,	% Reduction in Area	28
K,	Strength Coefficient	1,910 MPa
n,	Strain Hardening Exponent	0.08
R_c,	Rockwell Hardness	40

Axial Cyclic Properties ($R_\varepsilon = -1$)

E,	Elastic Modulus	208,500 MPa
σ_f,	Fatigue Strength Coefficient	1,640 MPa
b,	Fatigue Strength Exponent	-0.060
ε_f,	Fatigue Ductility Coefficient	2.67
c,	Fatigue Ductility Exponent	-0.820
K',	Cyclic Strength Coefficient	1,530 MPa
n',	Cyclic Strain Hardening Exponent	0.073

Torsional Cyclic Properties ($R_\gamma = -1$)

G,	Torsional Modulus	77,800 MPa
τ_f,	Fatigue Strength Coefficient	1,030 MPa
b,	Fatigue Strength Exponent	-0.074
γ'_f,	Fatigue Ductility Coefficient	3.62
c,	Fatigue Ductility Exponent	-0.778
A',	Cyclic Strength Coefficient	860 MPa
n',	Cyclic Strain Hardening Exponent	0.079

Table 3 Biaxial Fatigue Data, IN-718

MIDSECTION VALUES

PATH CODE	SPEC I.D.	CONTROL PARAMETERS $\frac{\Delta\varepsilon}{2}$	ε_o	$\frac{\Delta\gamma}{2}$	γ_o	STEADY STATE STRESSES $\frac{\Delta\sigma}{2}$ (MPa)	σ_o (MPa)	$\frac{\Delta\tau}{2}$ (MPa)	τ_o (MPa)	$N_{1.0}$ (cycles)	N_f (cycles)
A	B-33	0.0100	0	0	0	1090	-30	0	0	1,000	1,230
	B-14	0.0100	0	0	0	1100	-23	0	0	1,050	1,330
	B-6	0.0050	0	0	0	924	-19	0	0	13,500	14,200
	B-12	0.0050	0	0	0	931	-30	0	0	11,000	13,400
B	B-7	0	0	0.0176	0	0	0	605	5	890	1,690
	B-13	0	0	0.0176	0	0	0	596	0	800	1,670
	B-3	0	0	0.0087	0	0	0	538	1		10,600
	B-8	0	0	0.0087	0	0	0	535	-12	7,000	12,900
	A-35	0	0	0.0054	0	0	0	416	10		41,400
	A-30	0	0	0.0054	0	0	0	414	-20	35,700	45,200
C	B-35	0.0071	0	0.0123	0	752	-29	435	34	1,000	1,370
	B-11	0.0071	0	0.0123	0	758	-26	427	- 3	1,200	1,580
	B-26	0.0035	0	0.0061	0	633	-87	376	34	8,000	12,900
	B-4	0.0035	0	0.0061	0	633	-26	400	- 2	7,000	12,100

Table 3 (Cont'd) Biaxial Fatigue Data, IN-718

		MIDSECTION VALUES									
		CONTROL PARAMETERS				STEADY STATE STRESSES					
PATH CODE	SPEC I.D.	$\frac{\Delta\varepsilon}{2}$	ε_0	$\frac{\Delta\gamma}{2}$	γ_0	$\frac{\Delta\sigma}{2}$ (MPa)	σ_0 (MPa)	$\frac{\Delta\tau}{2}$ (MPa)	τ_0 (MPa)	$N_{1.0}$ (cycles)	N_f (cycles)
D	B-5	0.0100	0.0100	0	0	1083	19	0	0	800	936
	B-9	0.0100	0.0100	0	0	1089	22	0	0	800	959
	B-36	0.0050	0.0050	0	0	965	215	0	0	7,000	7,030
	B-15	0.0050	0.0050	0	0	944	215	0	0	6,000	8,000
E	B-99	0	0	0.0173	0.0173	0	0	580	14	1,000	1,690
	B-16	0	0	0.0173	0.0173	0	0	568	14	800	1,740
	B-32	0	0	0.0087	0.0087	0	0	507	76	4,500	9,530
	B-25	0	0	0.0087	0.0087	0	0	502	81	6,500	10,800
F	B-98	0.0071	0.0071	0.0123	0.0123	751	119	419	-71	1,050	1,330
	B-10	0.0071	0.0071	0.0123	0.0123	779	8	432	7	1,000	1,500
	B-34	0.0035	0.0035	0.0063	0.0063	646	170	396	52	4,800	5,960
	B-17	0.0035	0.0035	0.0063	0.0063	632	68	383	102	7,500	9,500

Table 3 (Cont'd) Biaxial, Fatigue Data, IN-718

		MIDSECTION VALUES									
		CONTROL PARAMETERS				STEADY STATE STRESSES					
PATH CODE	SPEC I.D.	$\frac{\Delta\varepsilon}{2}$	ε_o	$\frac{\Delta\gamma}{2}$	γ_o	$\frac{\Delta\sigma}{2}$ (MPa)	σ_o (MPa)	$\frac{\Delta\tau}{2}$ (MPa)	τ_o (MPa)	$N_{1.0}$ (cycles)	N_f (cycles)
G	B-31	0.0035	-0.0035	0.0063	-0.0063	598	-190	381	-43	6,000	14,100
	B-23	0.0035	-0.0035	0.0063	-0.0063	594	-213	375	-29	7,000	16,000
H	B-18	0.0035	0	0.0063	0.0063	631	-216	386	139	5,000	9,140
	B-19	0.0035	0	0.0063	0.0063	632	-189	381	138	5,000	7,420
I	B-21	0.0035	0	0.0063	0.0063	637	84	389	126	4,000	7,680
	B-30	0.0035	0	0.0063	0.0063	631	97	398	120	4,000	8,000
J	B-24	0.0035	0.0035	0.0063	0	638	218	394	-71	3,000	5,150
	B-29	0.0035	0.0035	0.0063	0	637	279	413	-85	3,000	3,490

Table 3 (Cont'd) Biaxial Fatigue Data, IN-718

		MIDSECTION VALUES									
		CONTROL PARAMETERS				STEADY STATE STRESSES					
PATH CODE	SPEC I.D.	$\frac{\Delta\varepsilon}{2}$	ε_o	$\frac{\Delta\gamma}{2}$	γ_o	$\frac{\Delta\sigma}{2}$ (MPa)	σ_o (MPa)	$\frac{\Delta\tau}{2}$ (MPa)	τ_o (MPa)	$N_{1.0}$ (cycles)	N_f (cycles)
K	A-36	0	0.0010	0.0086	0	0	75	504	-42	6,500	8,370
	A-34	0	0.0010	0.0086	0	0	63	505	- 4	7,470	10,900
L	A-31	0	-0.0010	0.0086	0	0	-172	507	0	3,890	8,000
	A-33	0	-0.0010	0.0086	0	0	-161	513	0	9,090	13,100
M	A-32	0.0035	0	0.0062	0	520	-10	495	31	5,550	6,700
	A-29	0.0035	0	0.0062	0	510	-28	496	25	6,080	6,990
N	B-97	0.0071	0	0.0123	0	999	-29	552	1	430	565
	B-20	0.0071	0	0.0123	0	999	-32	567	- 8	450	560
	B-28	0.0035	0	0.0062	0	758	-19	463	-10	4,370	5,810
	B-27	0.0035	0	0.0062	0	758	-34	463	1	3,350	5,150
O	A-28	0.0035	0.0035	0.0062	0	724	283	450	- 7	3,550	4,450
	A-27	0.0035	0.0035	0.0062	0	724	308	450	- 4	3,330	3,850

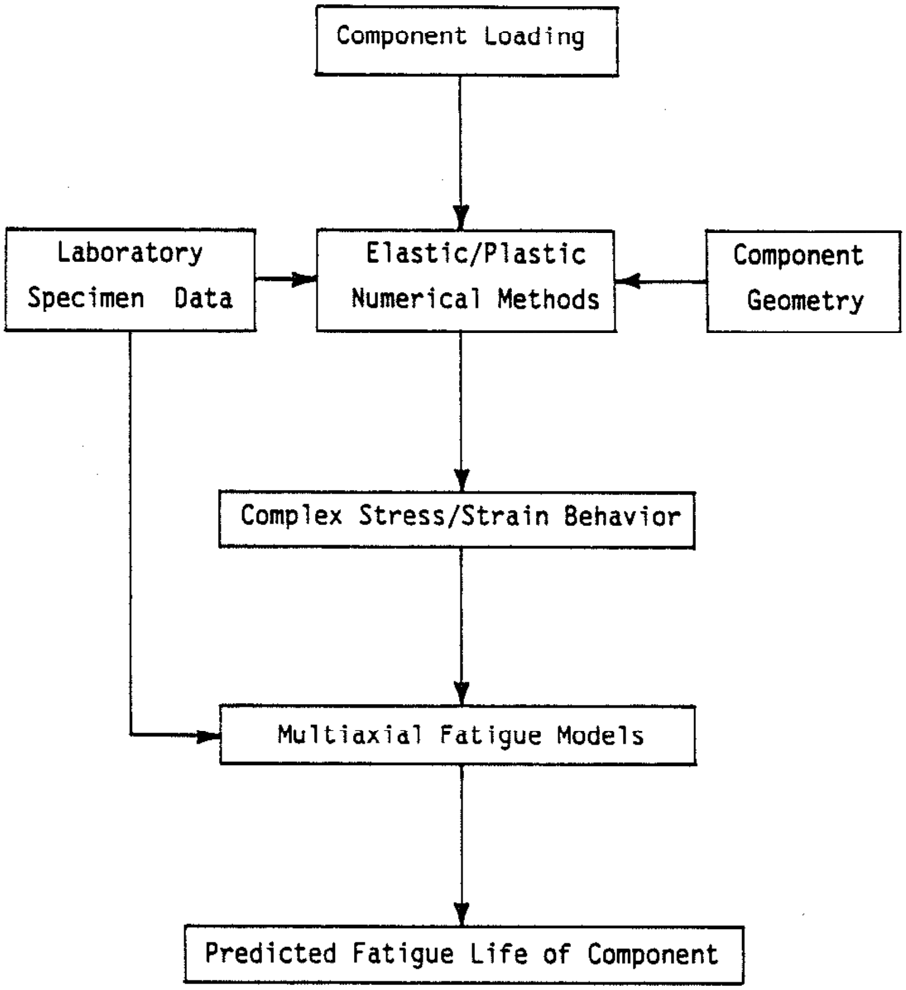

Figure 1 Design Flowchart

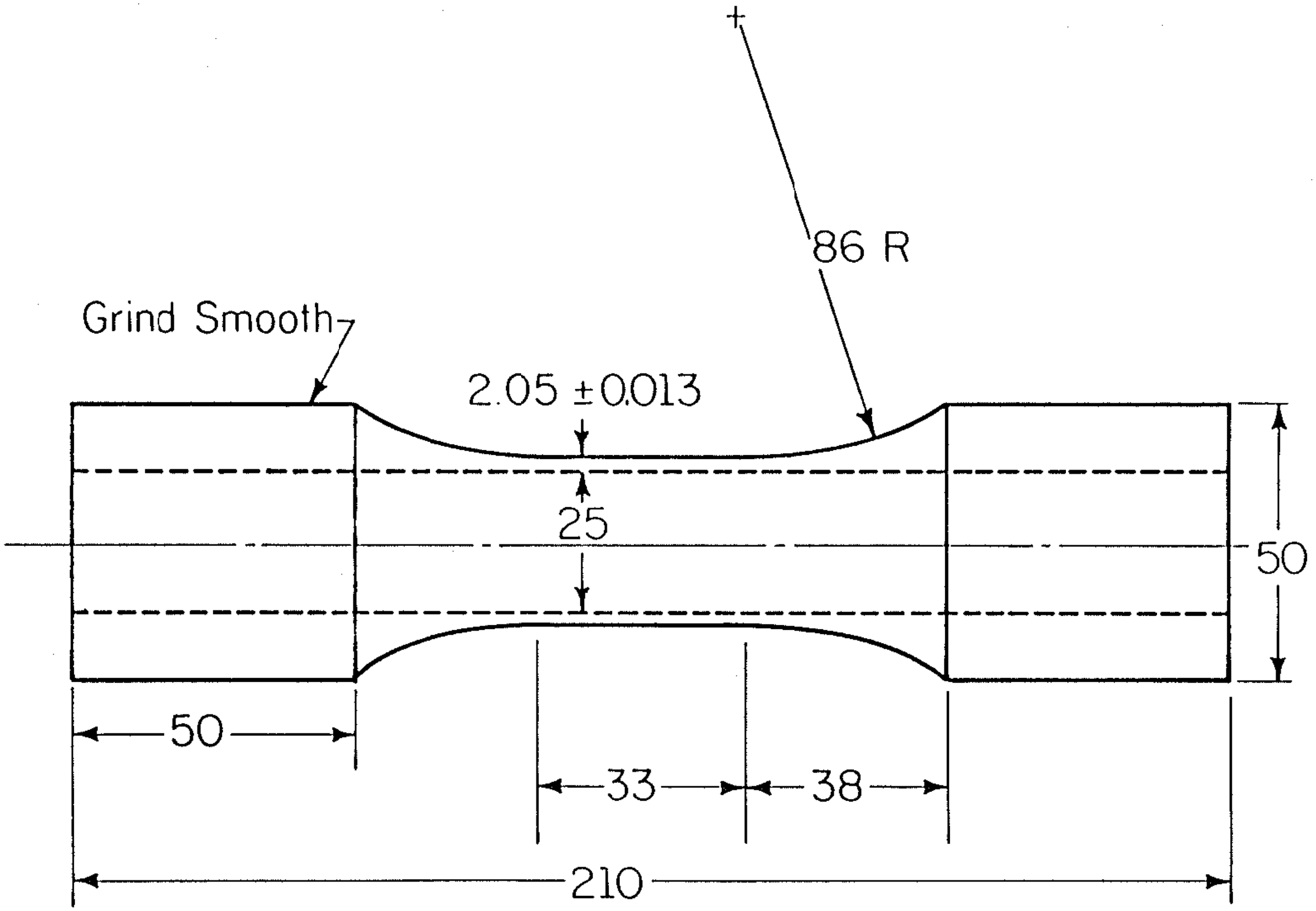

Figure 2 Biaxial Specimen Dimensions

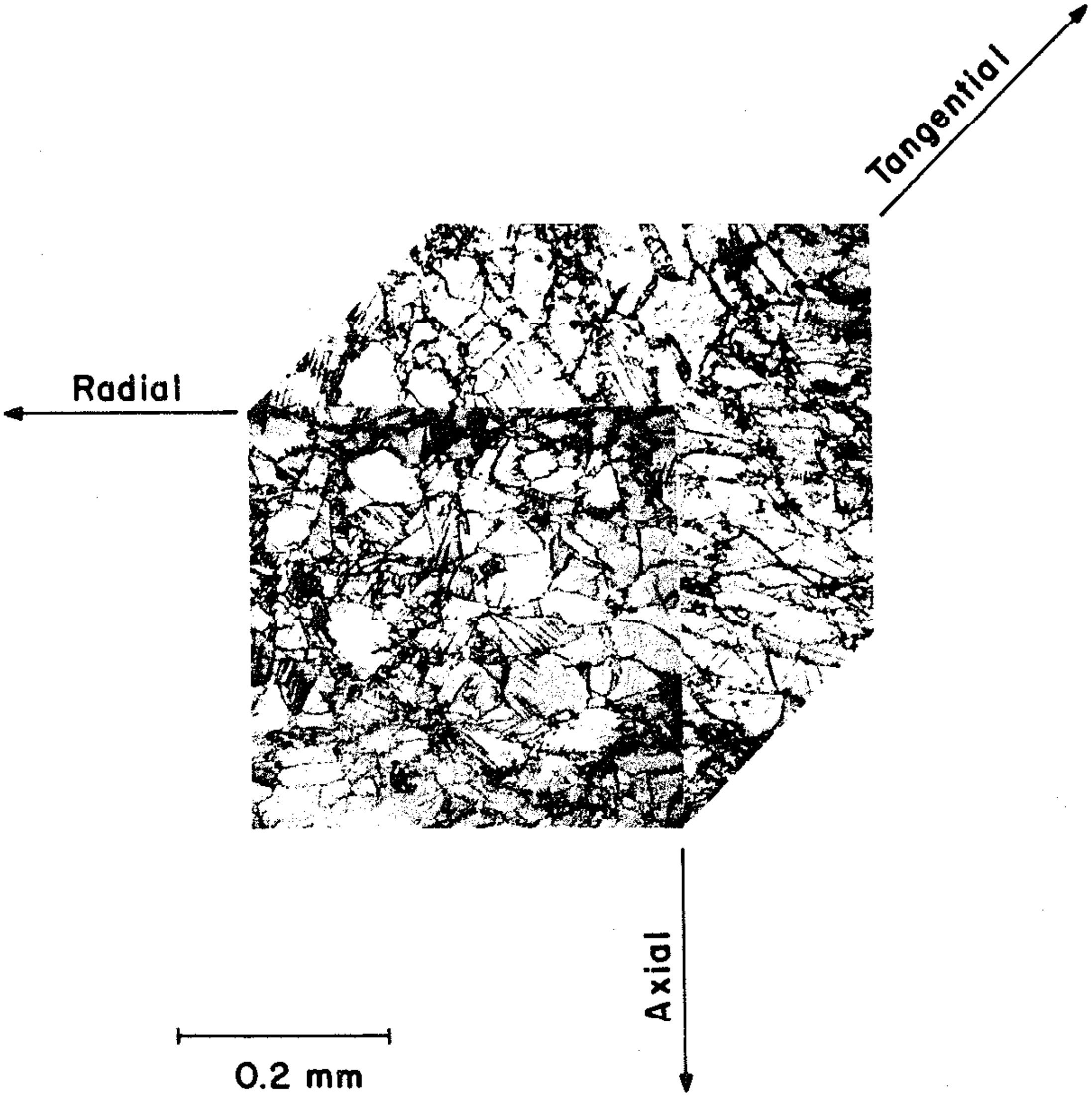

Figure 3   Microstructure of IN-718

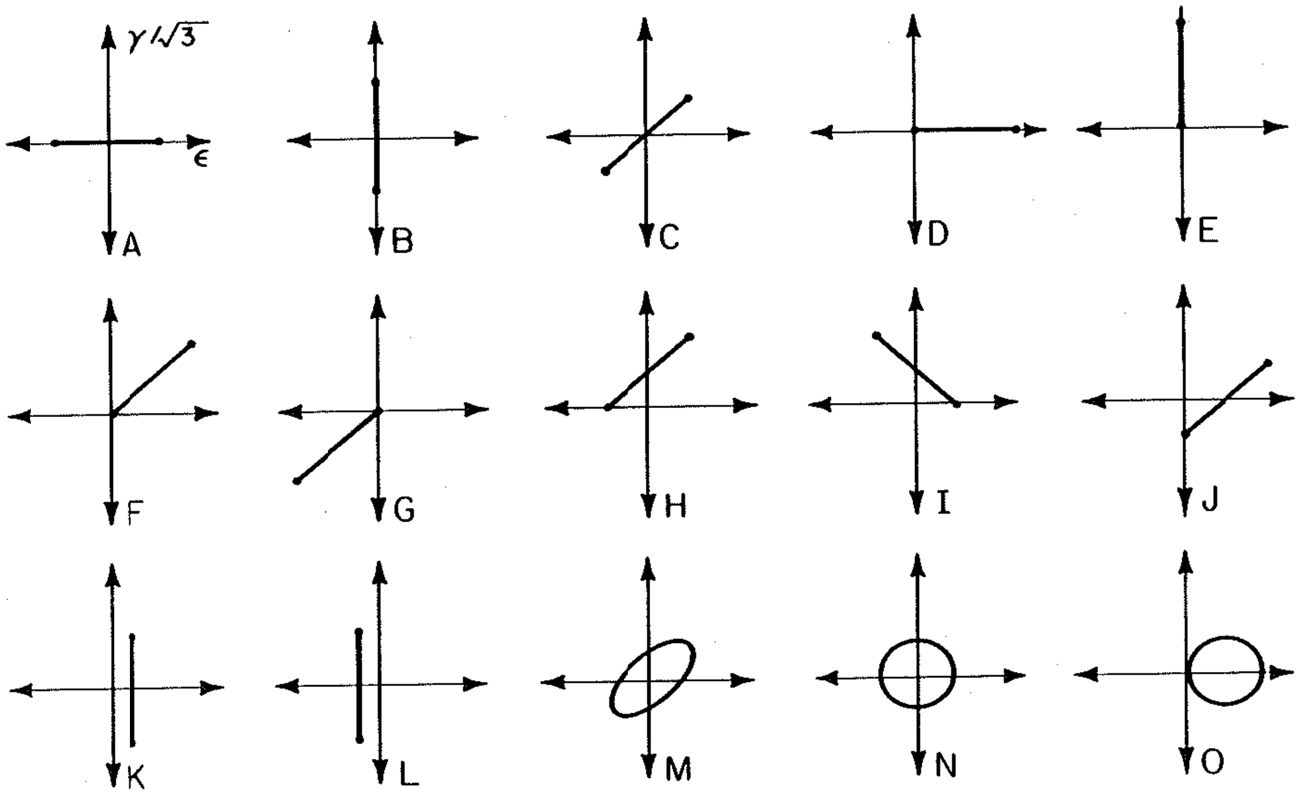

Figure 4 Biaxial Strain Paths

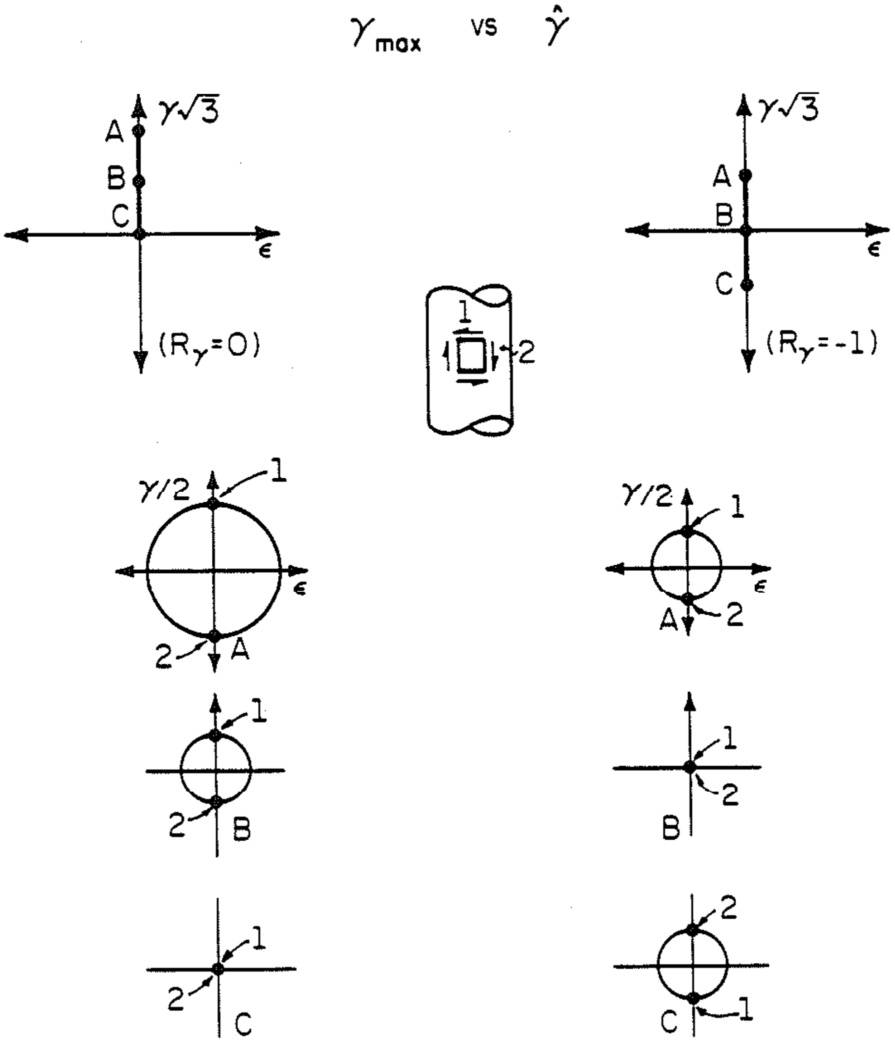

Figure 5 Comparison of γ and γ_{max}, Proportional Loading

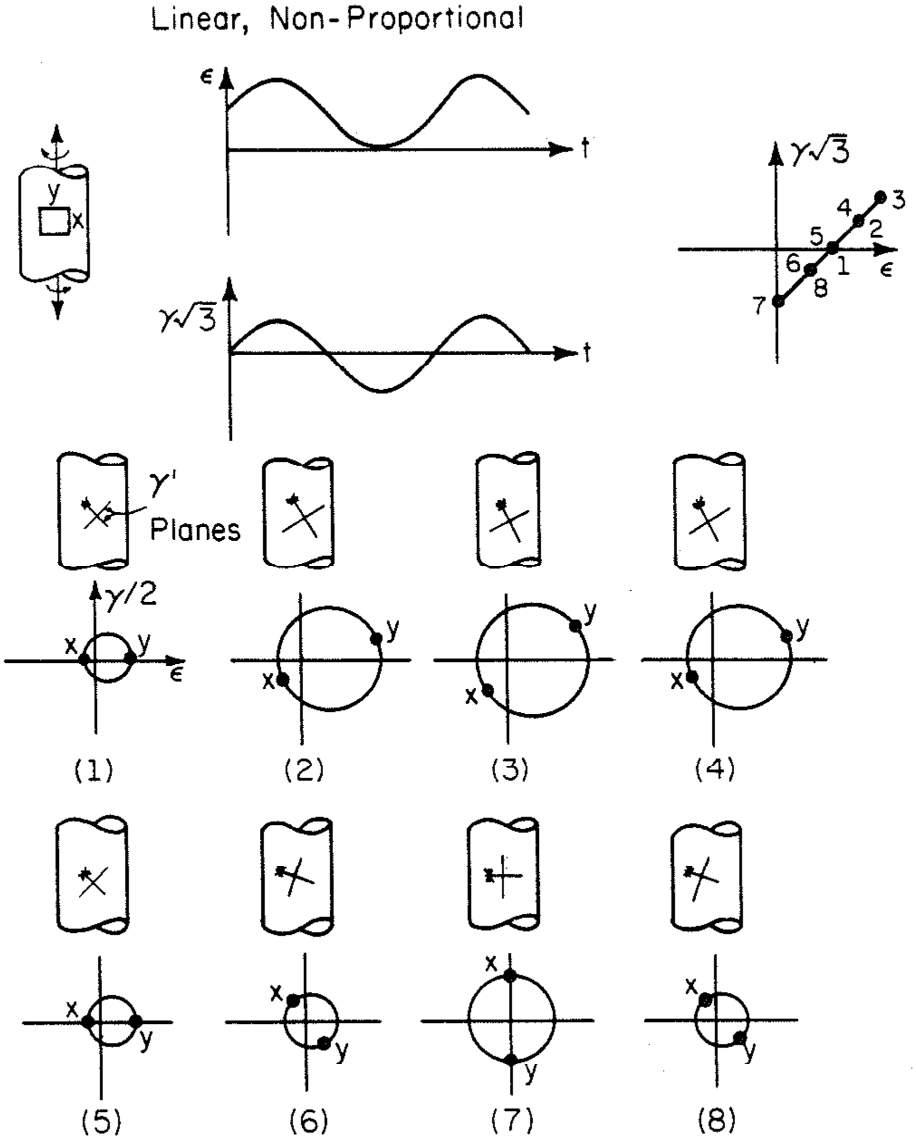

Figure 6 γ' Plane Illustration for Non-proportional Loading

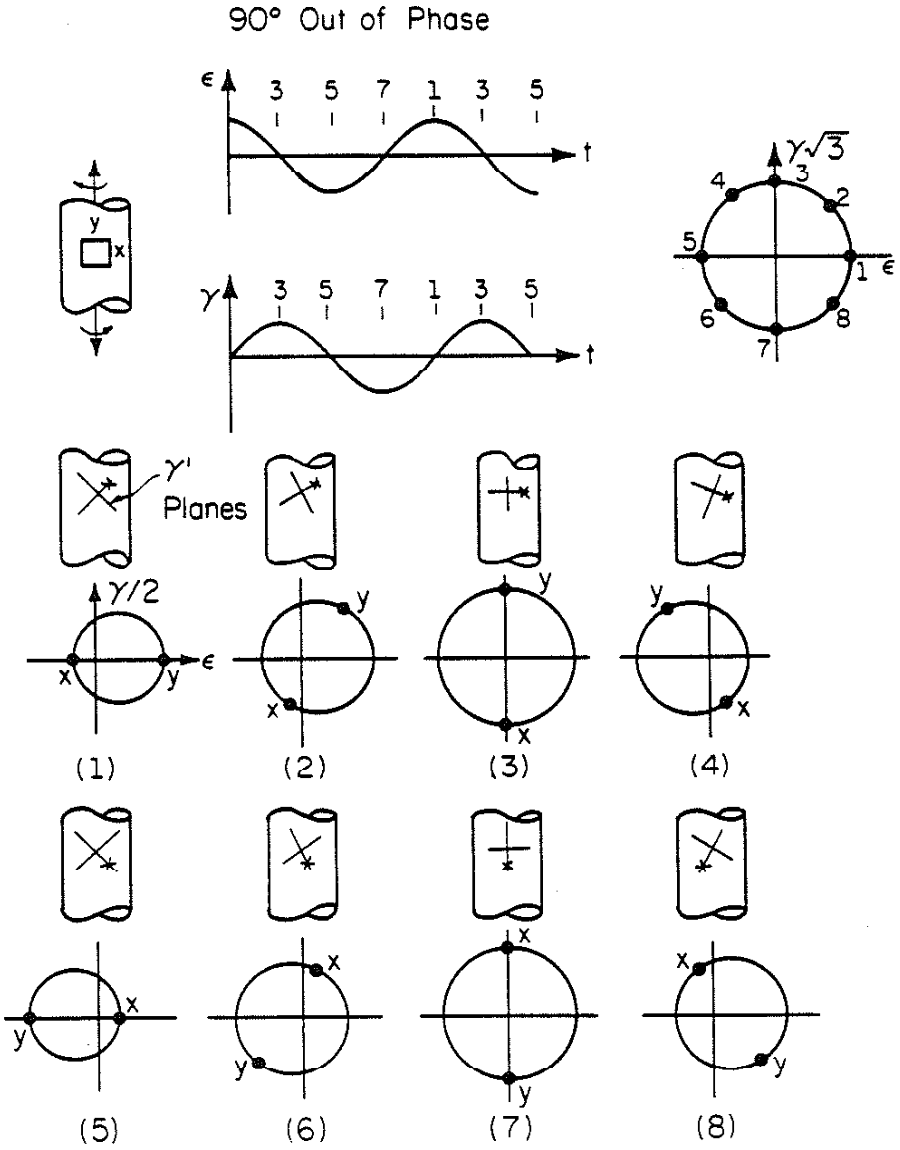

Figure 7 γ' Plane Illustration for Out-of-Phase Loading

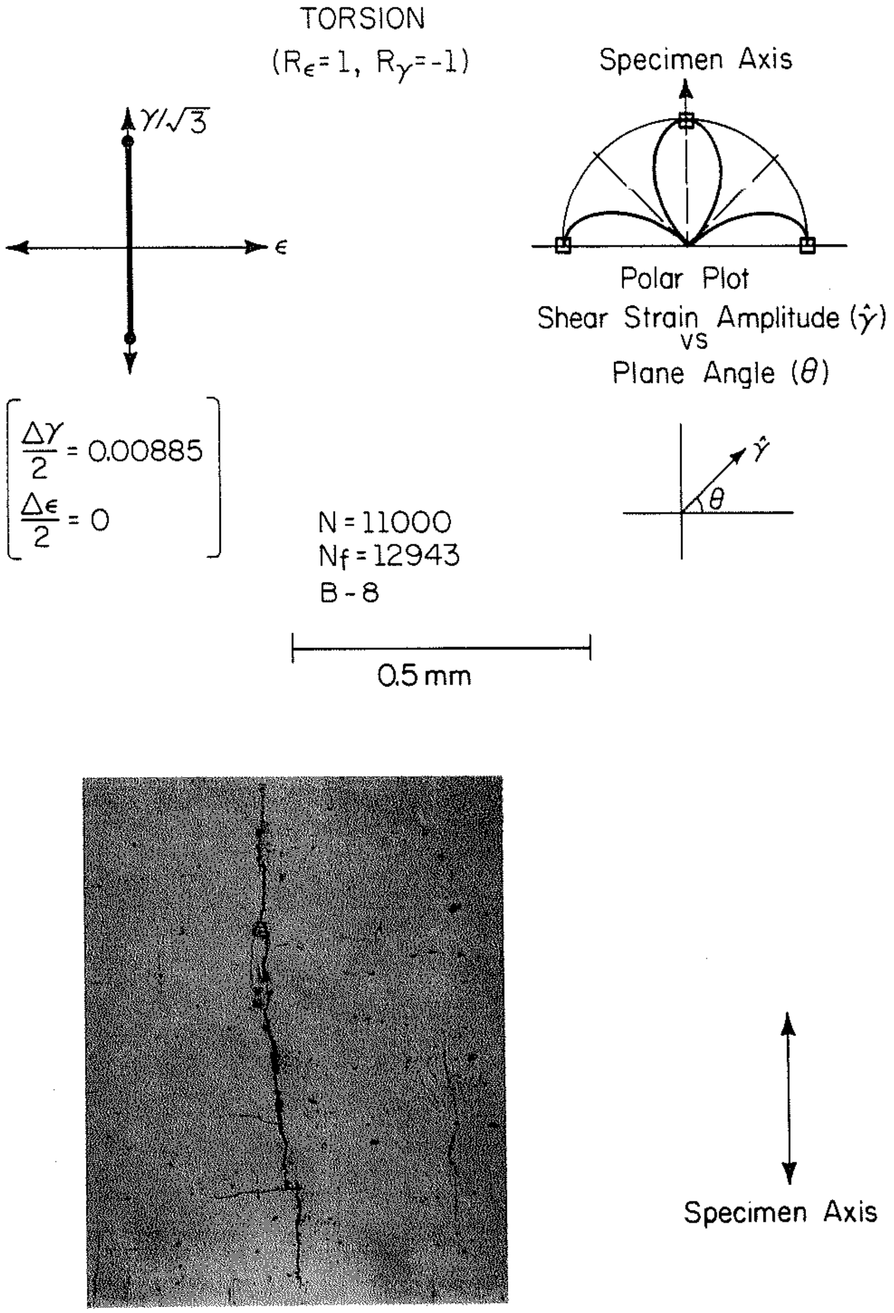

Figure 8 Strain Path B, $\bar{\varepsilon}$ = 0.005, Failure Crack Direction

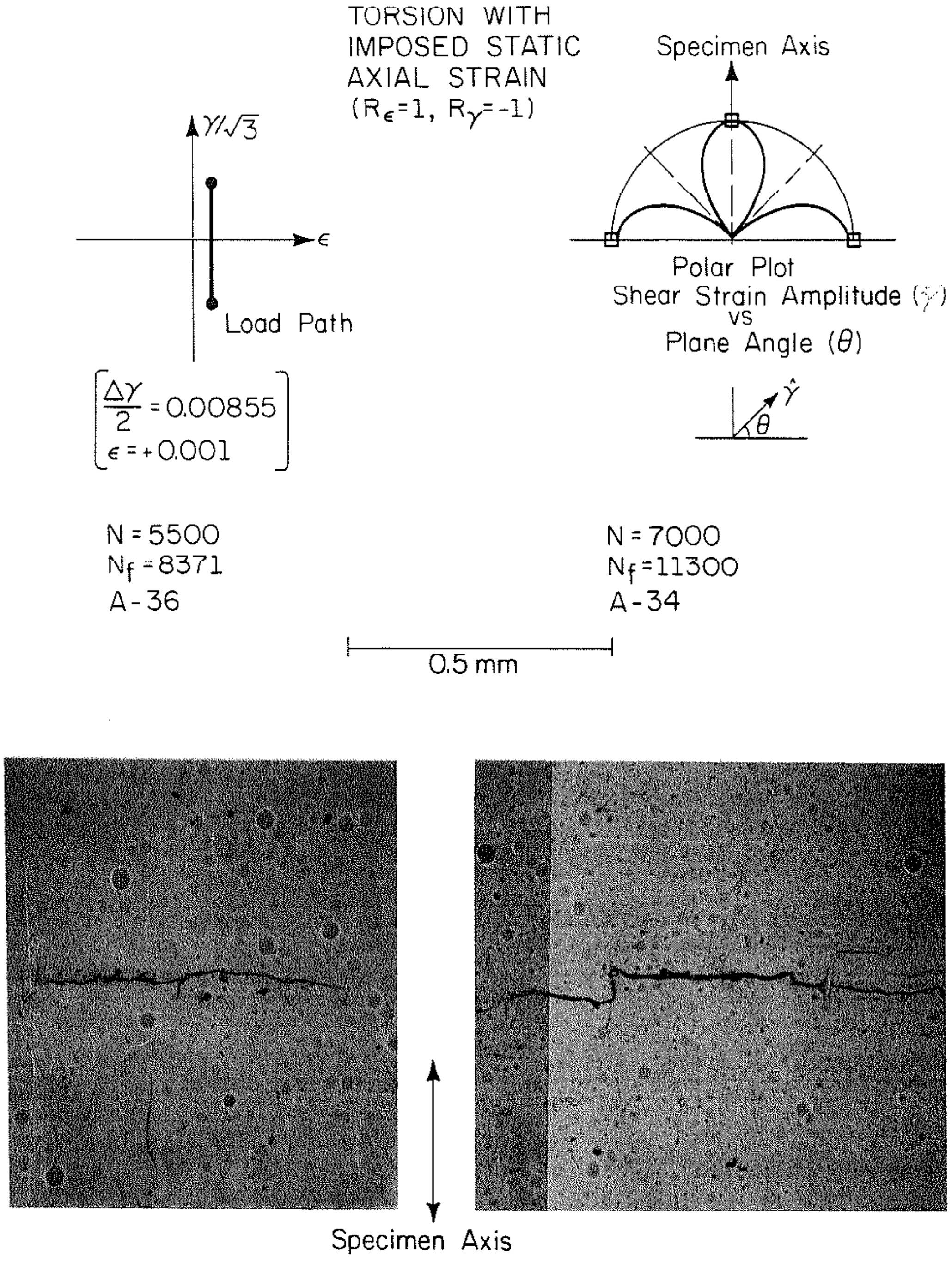

Figure 9 Strain Path K, $\bar{\varepsilon}$ = 0.005, Failure Crack Direction

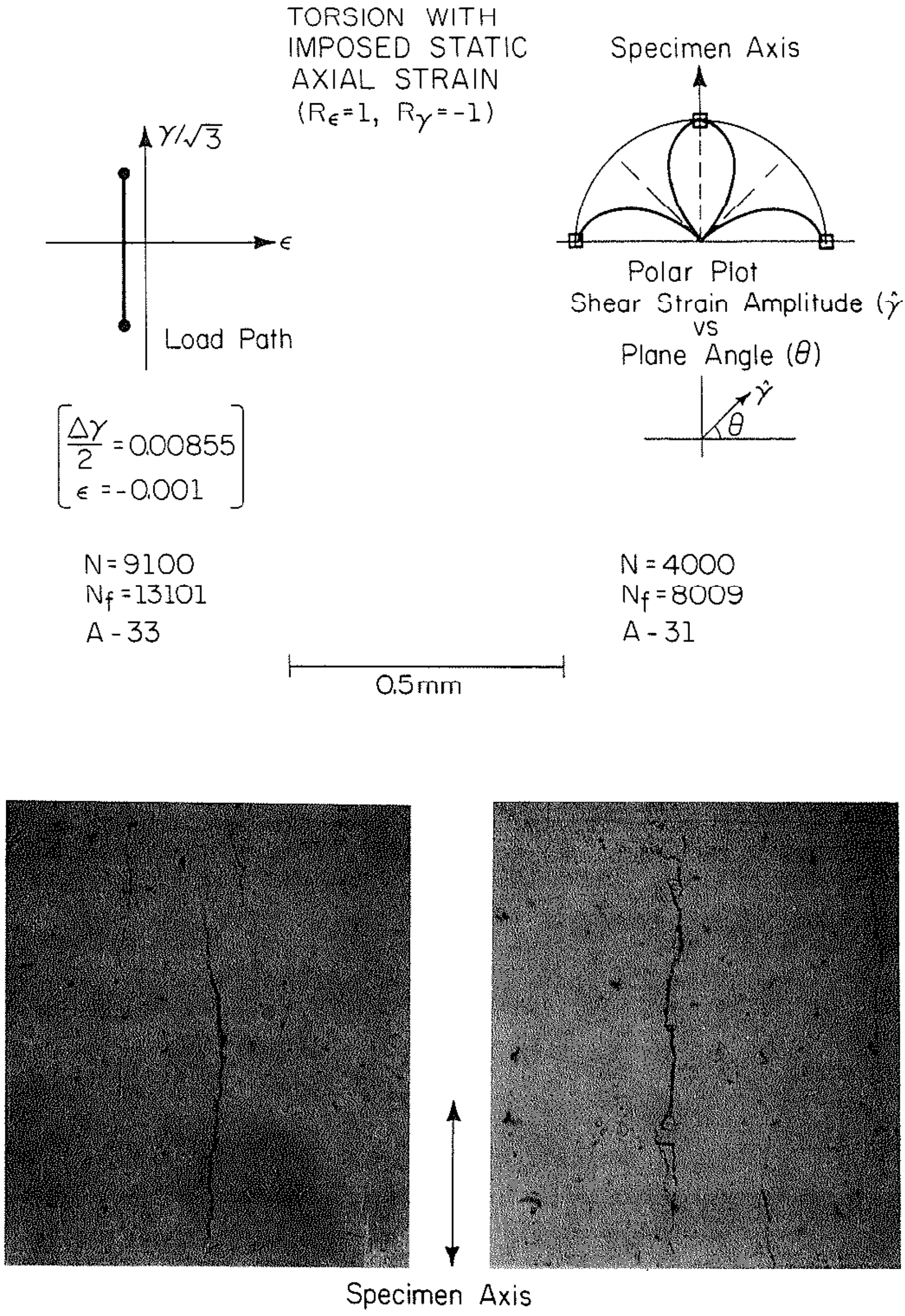

Figure 10 Strain Path L, $\bar{\epsilon}$ = 0.005, Failure Crack Direction

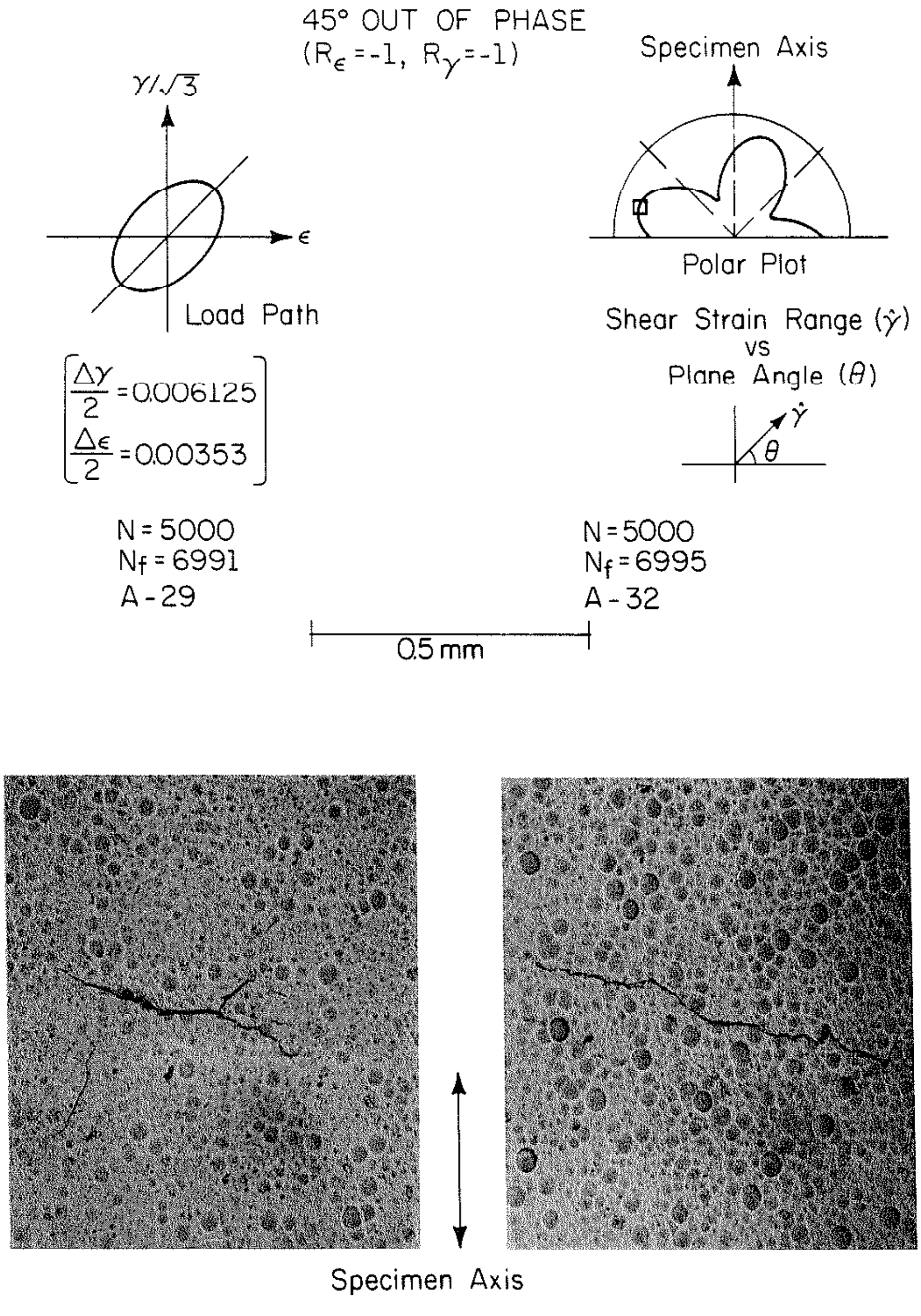

Figure 11 Strain Path M, $\bar{\varepsilon}$ = 0.005, Failure Crack Direction

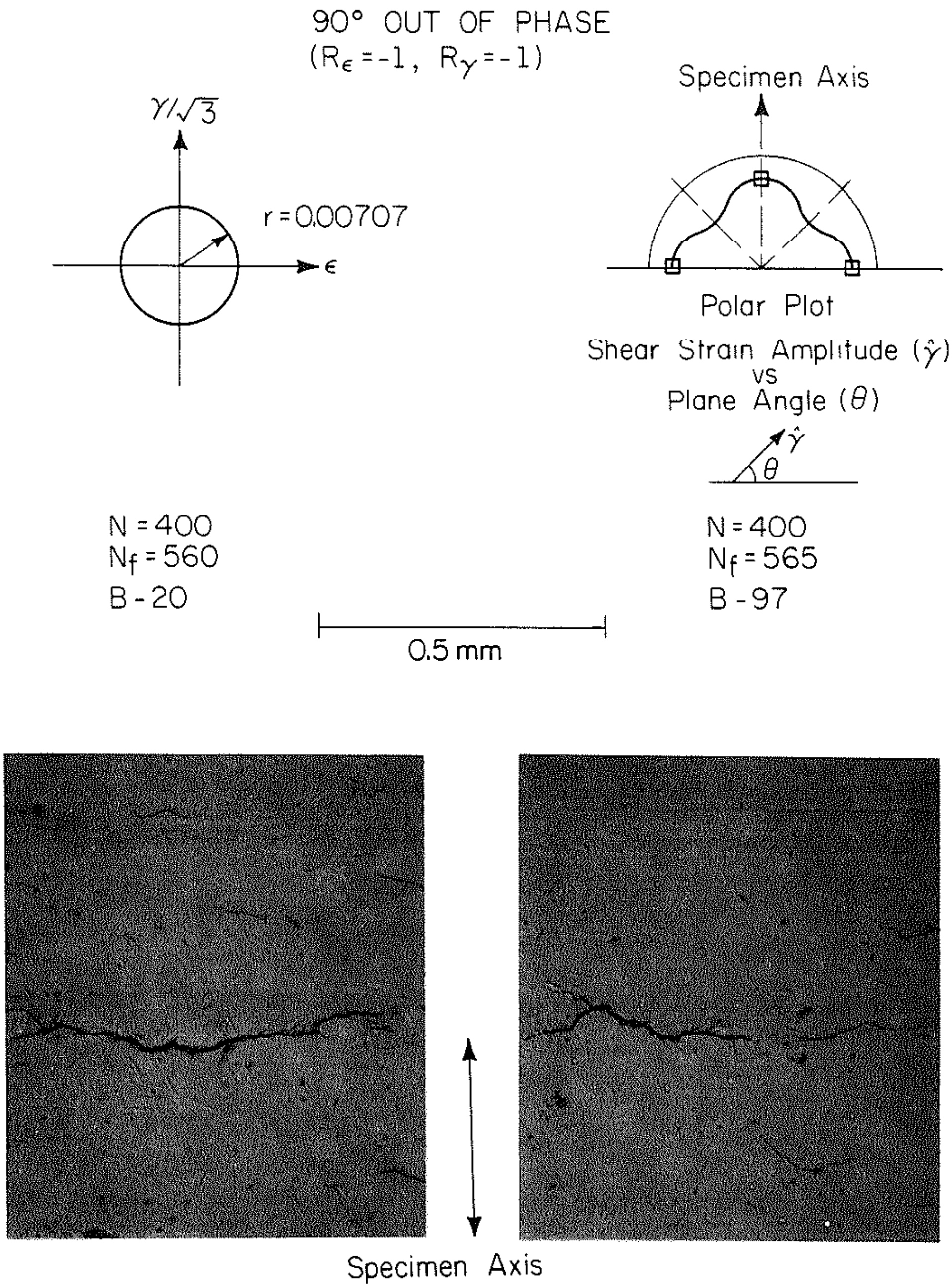

Figure 12 Strain Path N, $\bar{\varepsilon}$ = 0.01, Failure Crack Direction

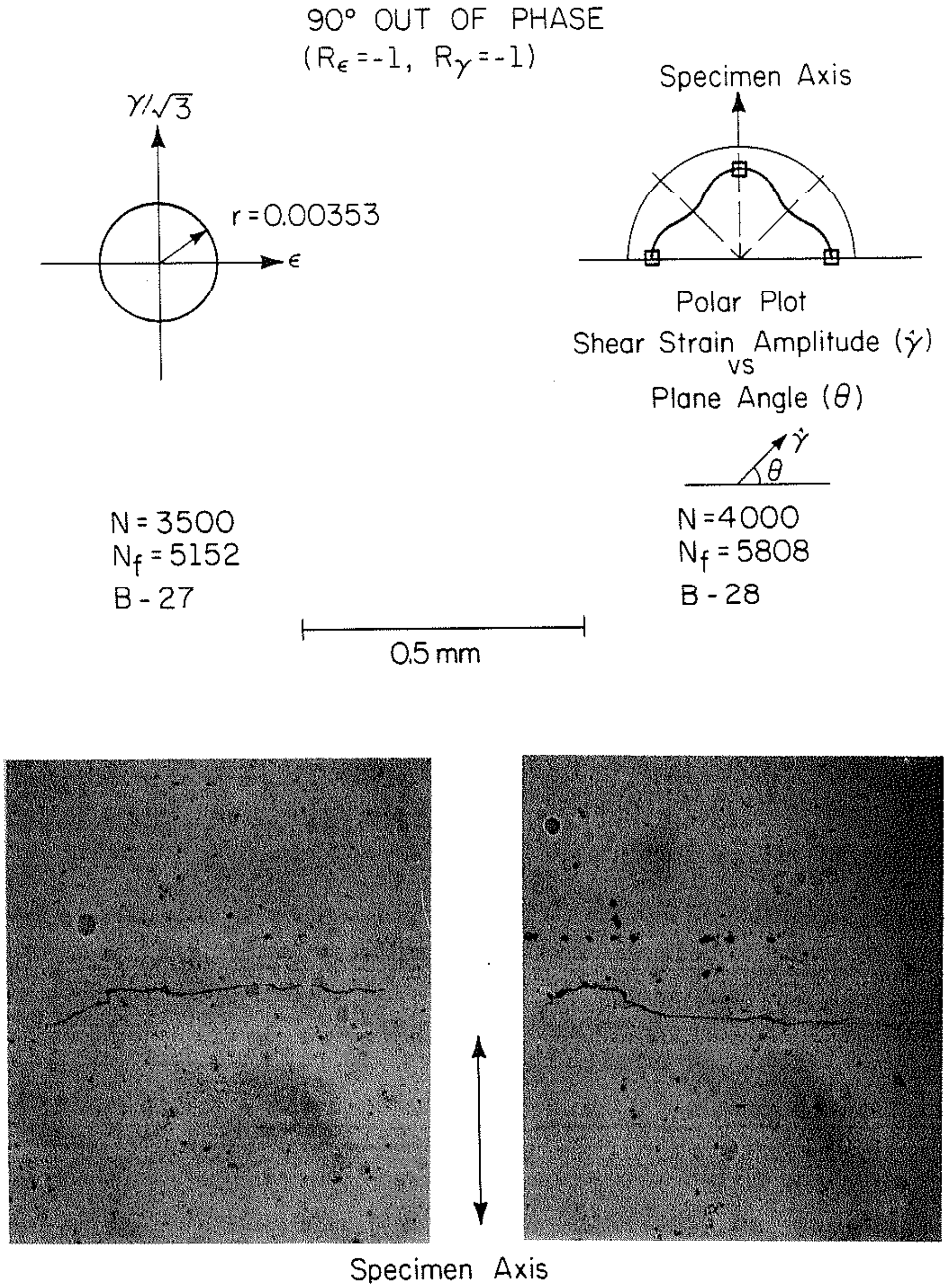

Figure 13 Strain Path N, $\overline{\varepsilon}$ = 0.005, Failure Crack Direction

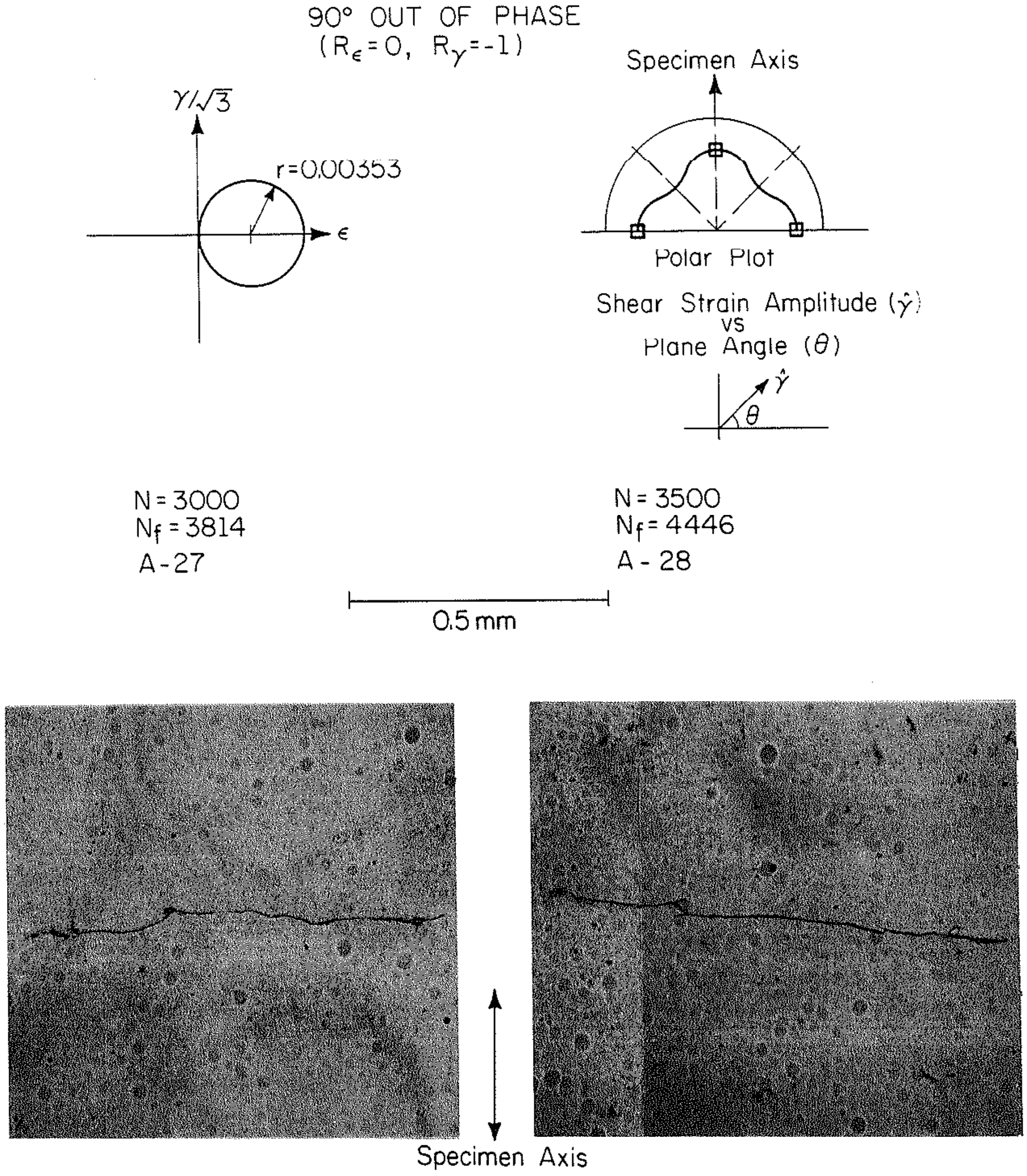

Figure 14 Strain Path 0, $\overline{\epsilon}$ = 0.005, Failure Crack Direction

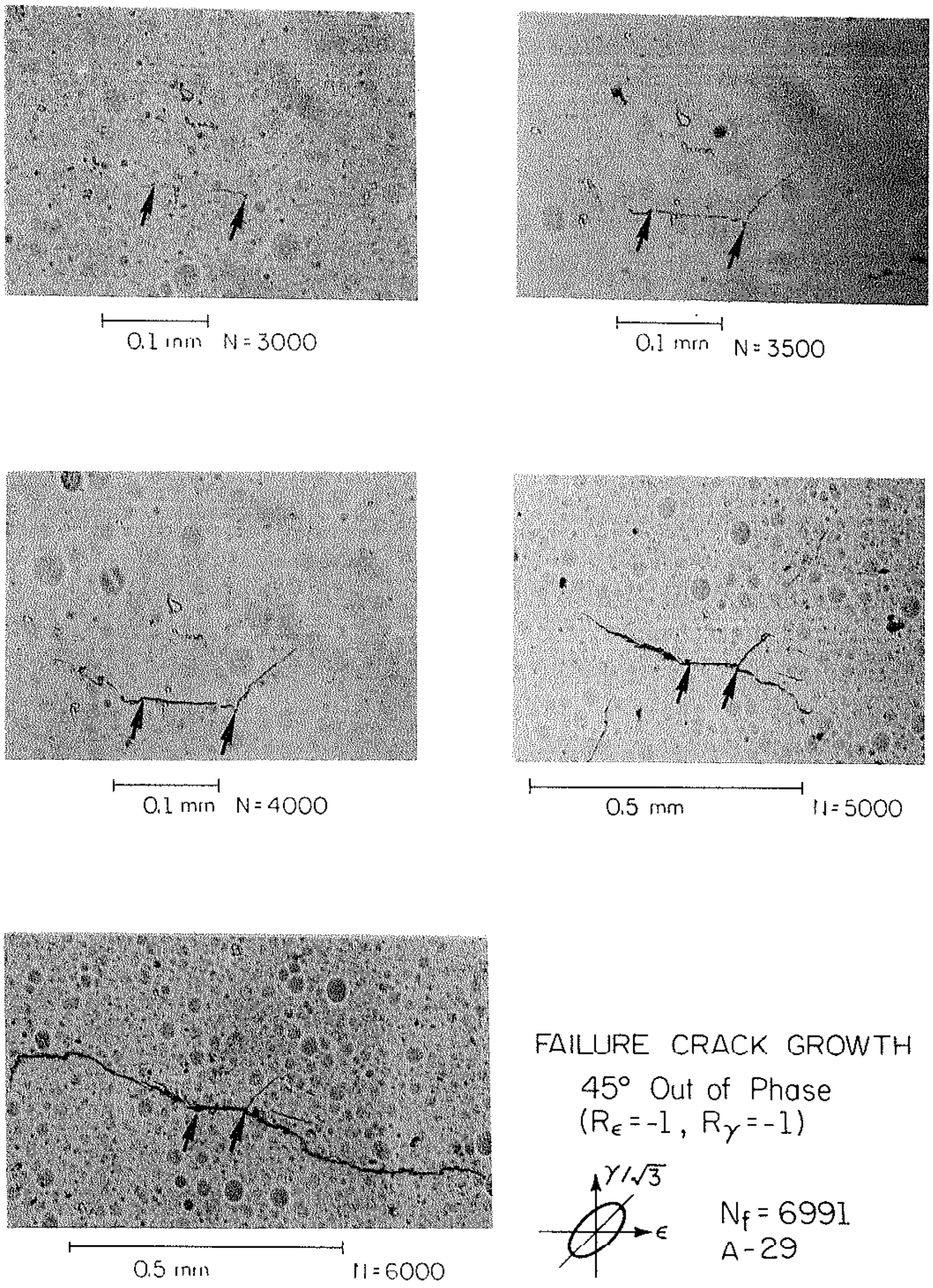

Figure 15 Strain Path M, $\bar{\varepsilon} = 0.005$, Failure Crack Growth

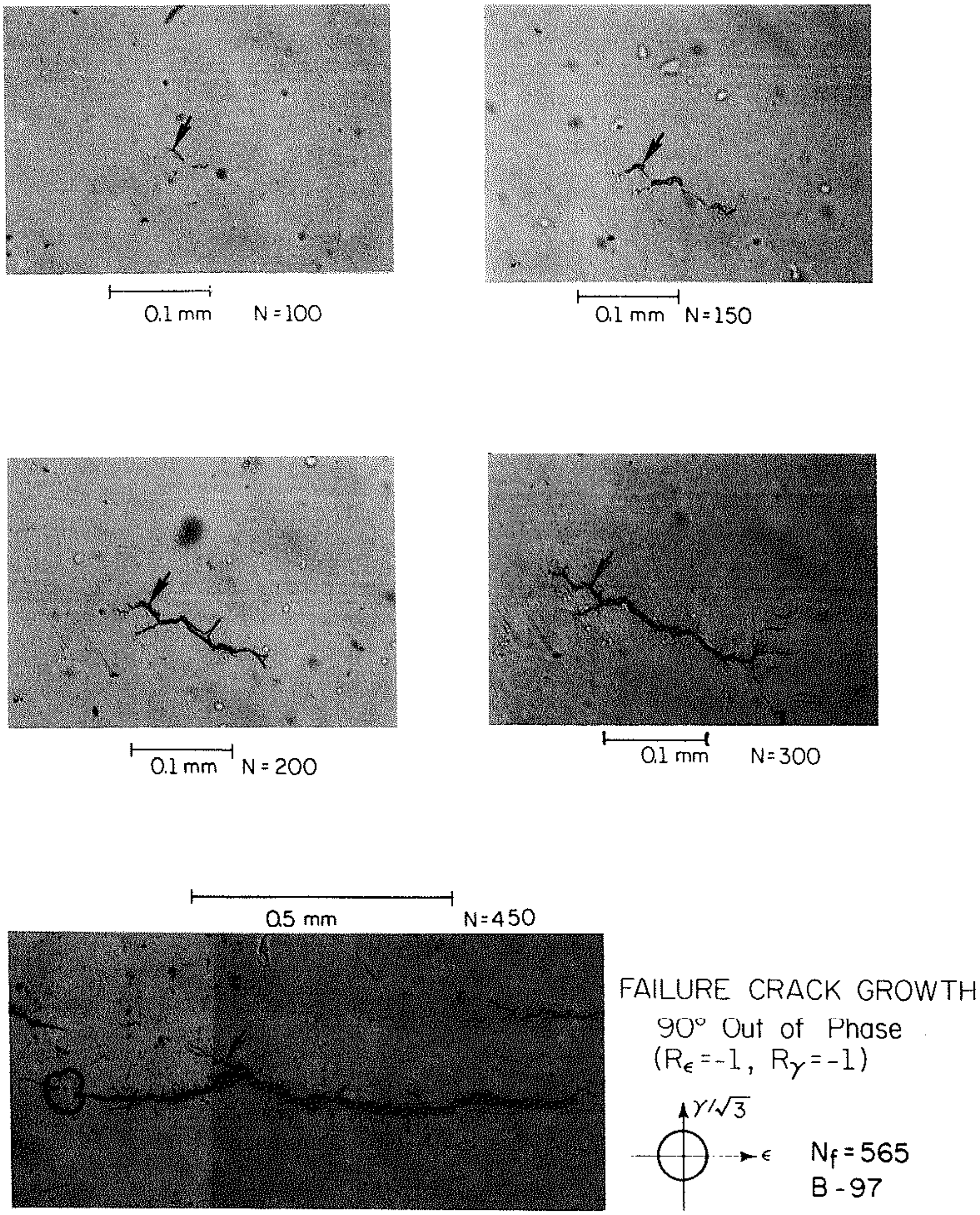

Figure 16 Strain Path N, $\overline{\varepsilon} = 0.01$, Failure Crack Growth

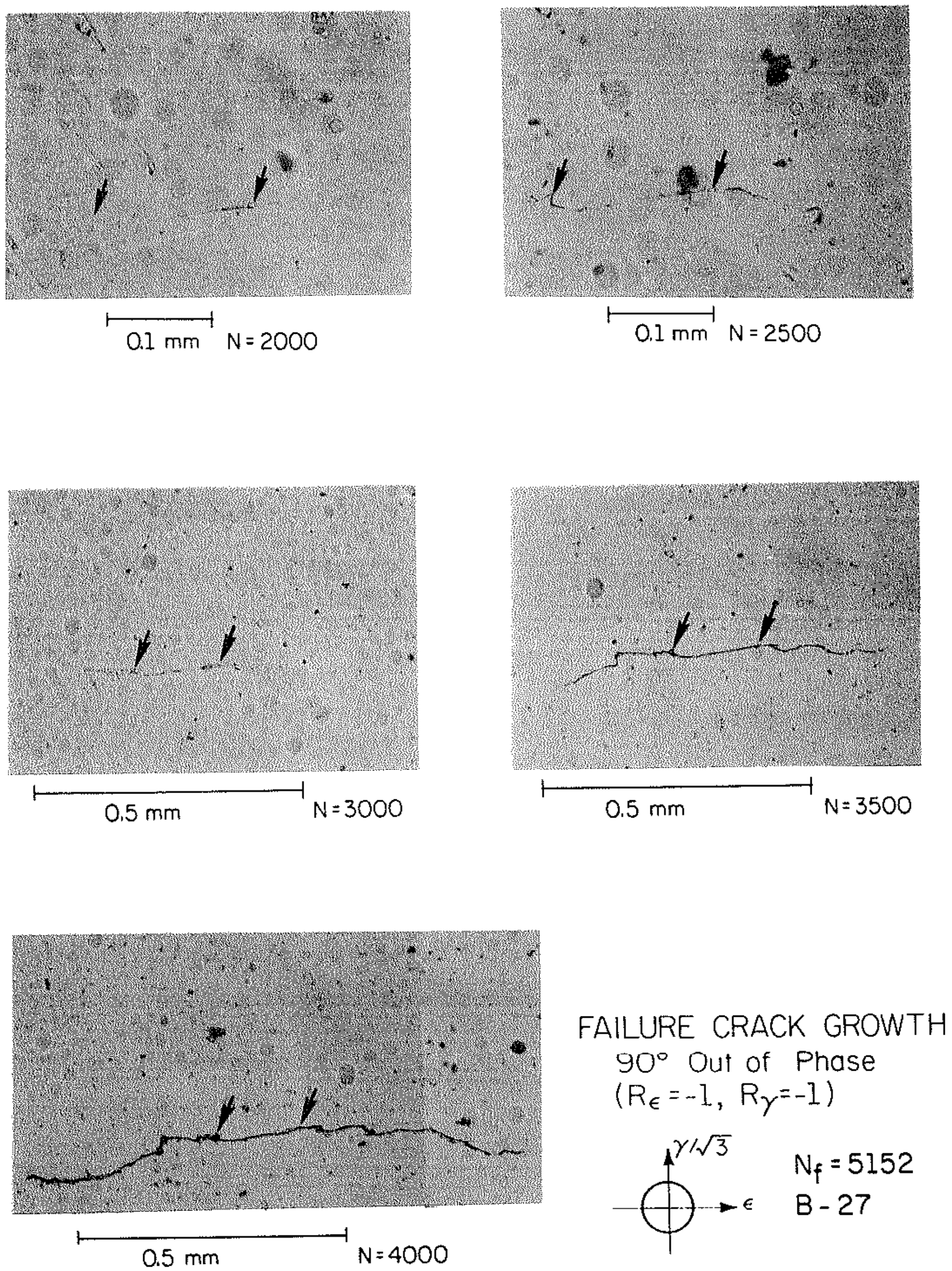

Figure 17 Strain Path N, $\bar{\varepsilon}$ = 0.005, Failure Crack Growth

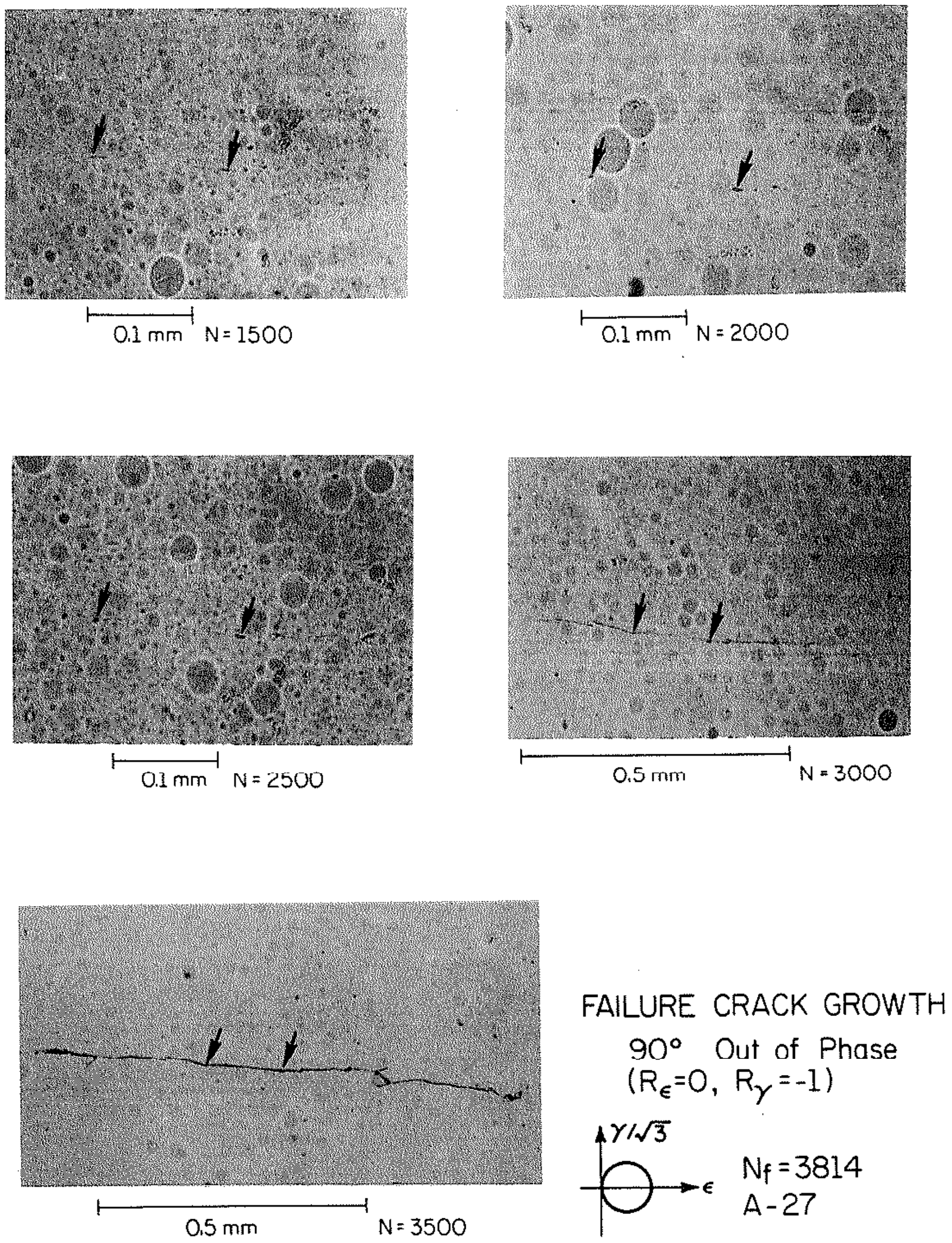

Figure 18 Strain Path 0, $\bar{\varepsilon}$ = 0.005, Failure Crack Growth

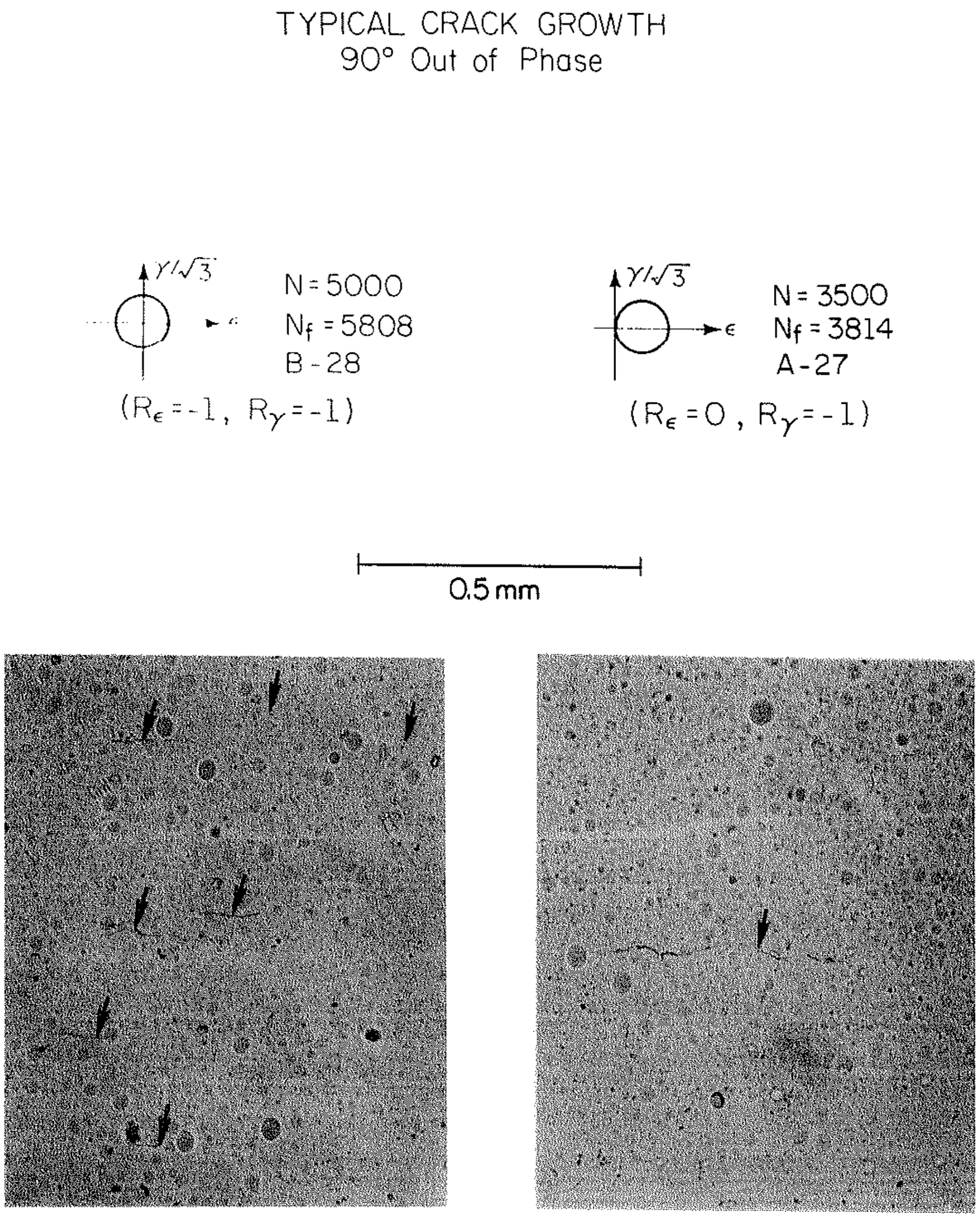

Figure 19 Strain Paths and N and 0, $\overline{\varepsilon}$ 0 0.005, Typical Crack Density

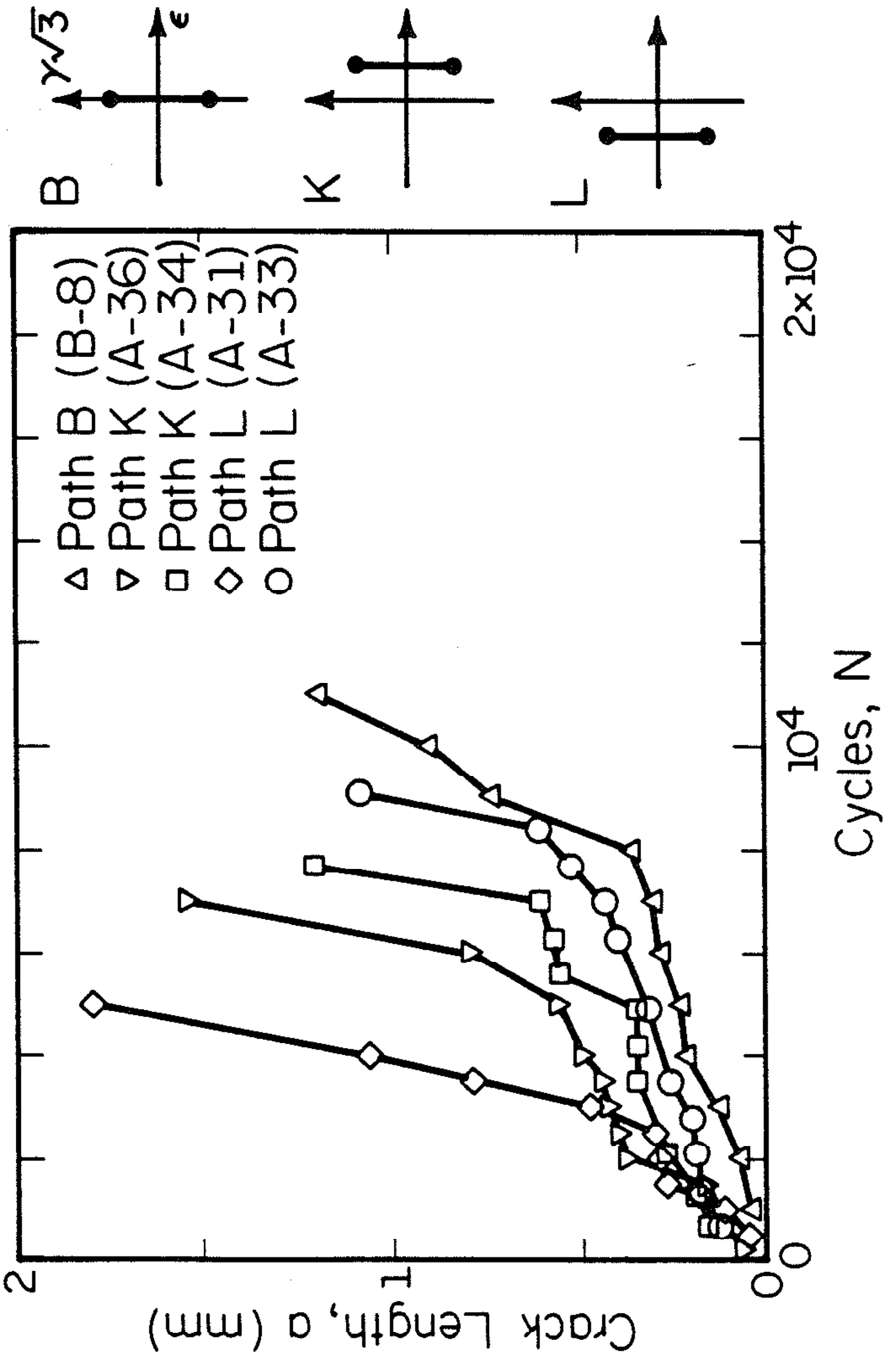

Figure 20 Strain Paths B, K, and L, $\bar{\epsilon}$ = 0.005, Crack Growth Comparison

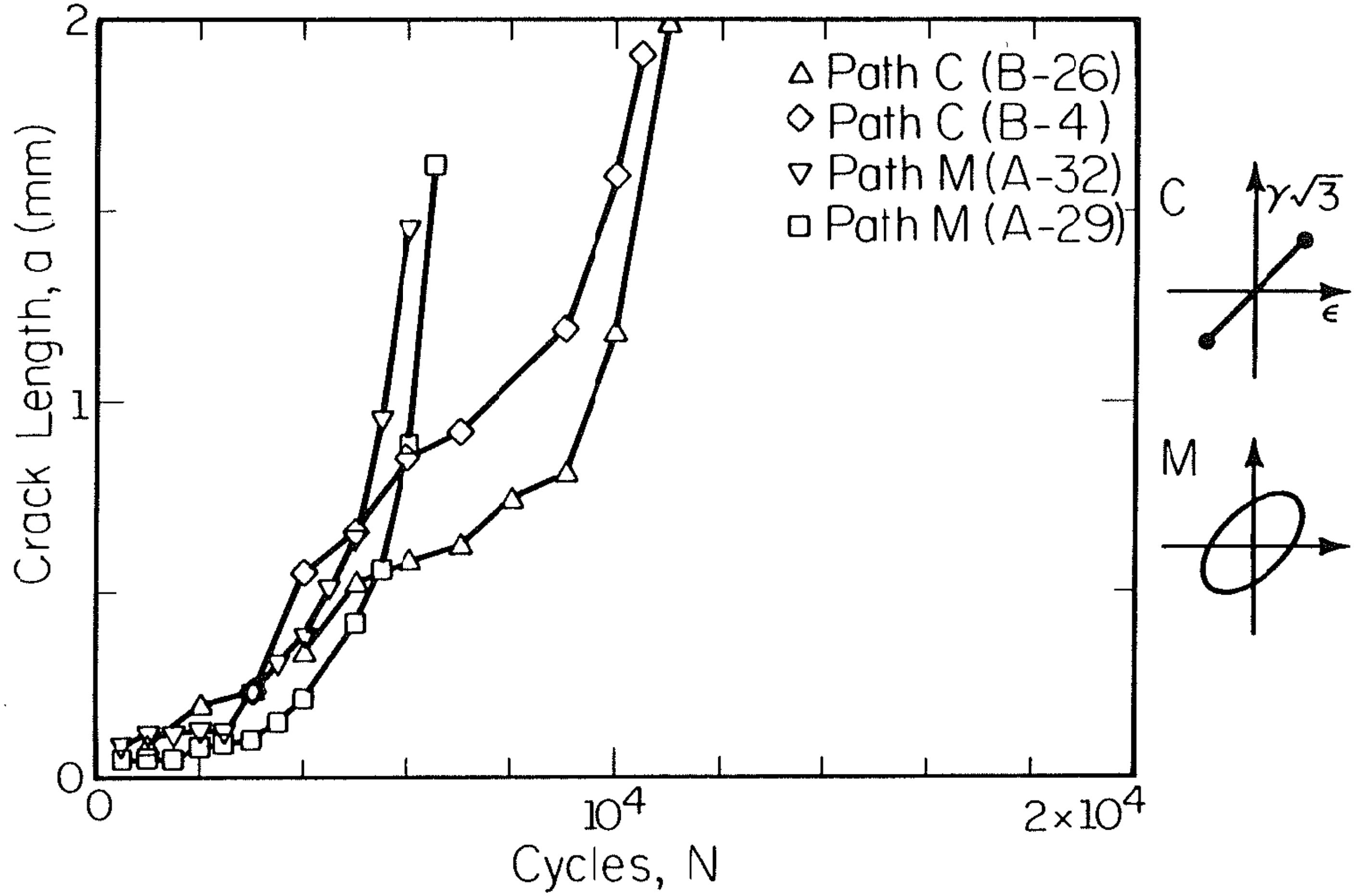

Figure 21 Strain Paths C and M, $\bar{\varepsilon} = 0.005$, Crack Growth Comparison

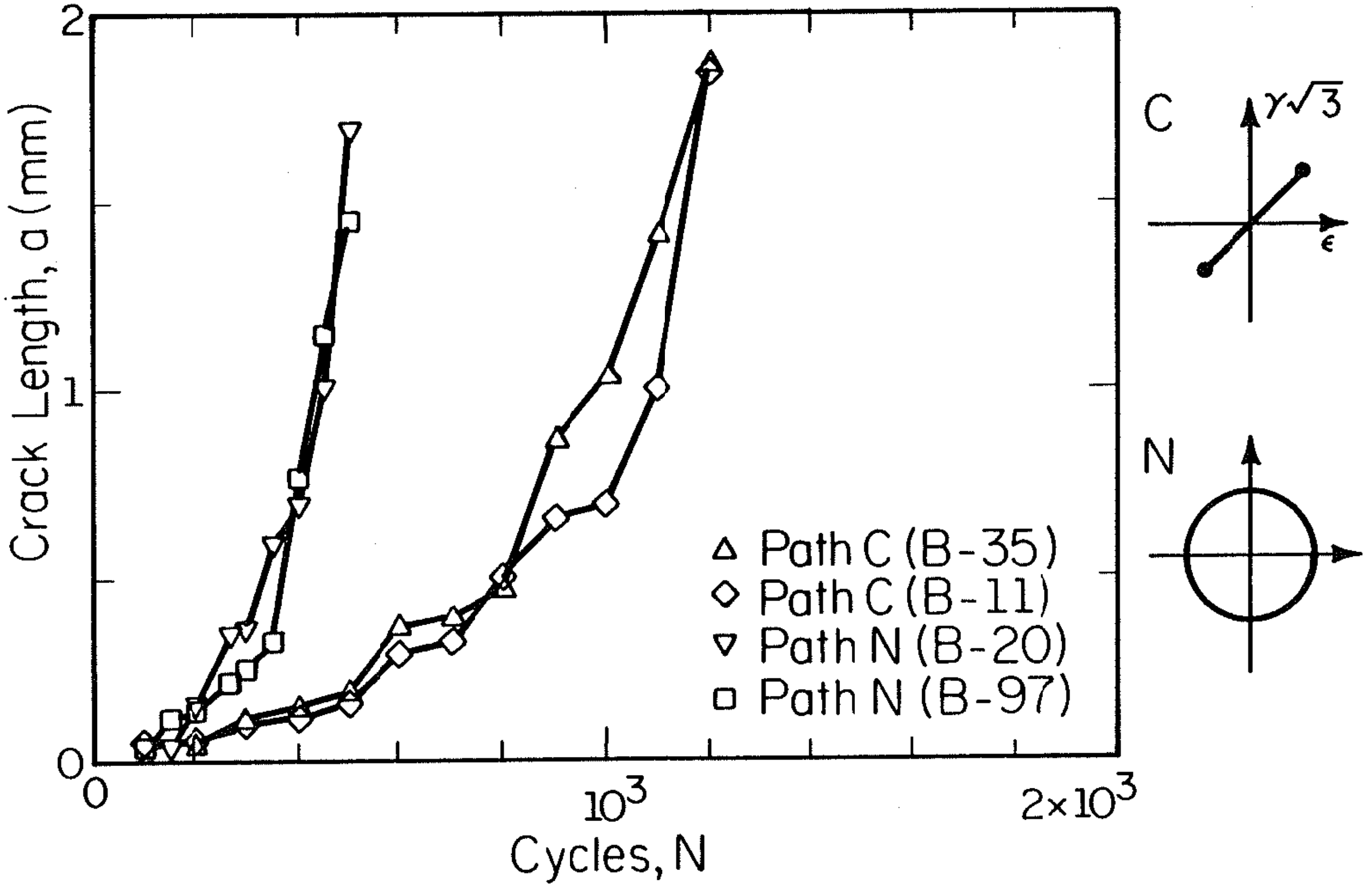

Figure 22 Strain Paths C and N, $\bar{\varepsilon}$ = 0.01, Crack Growth Comparison

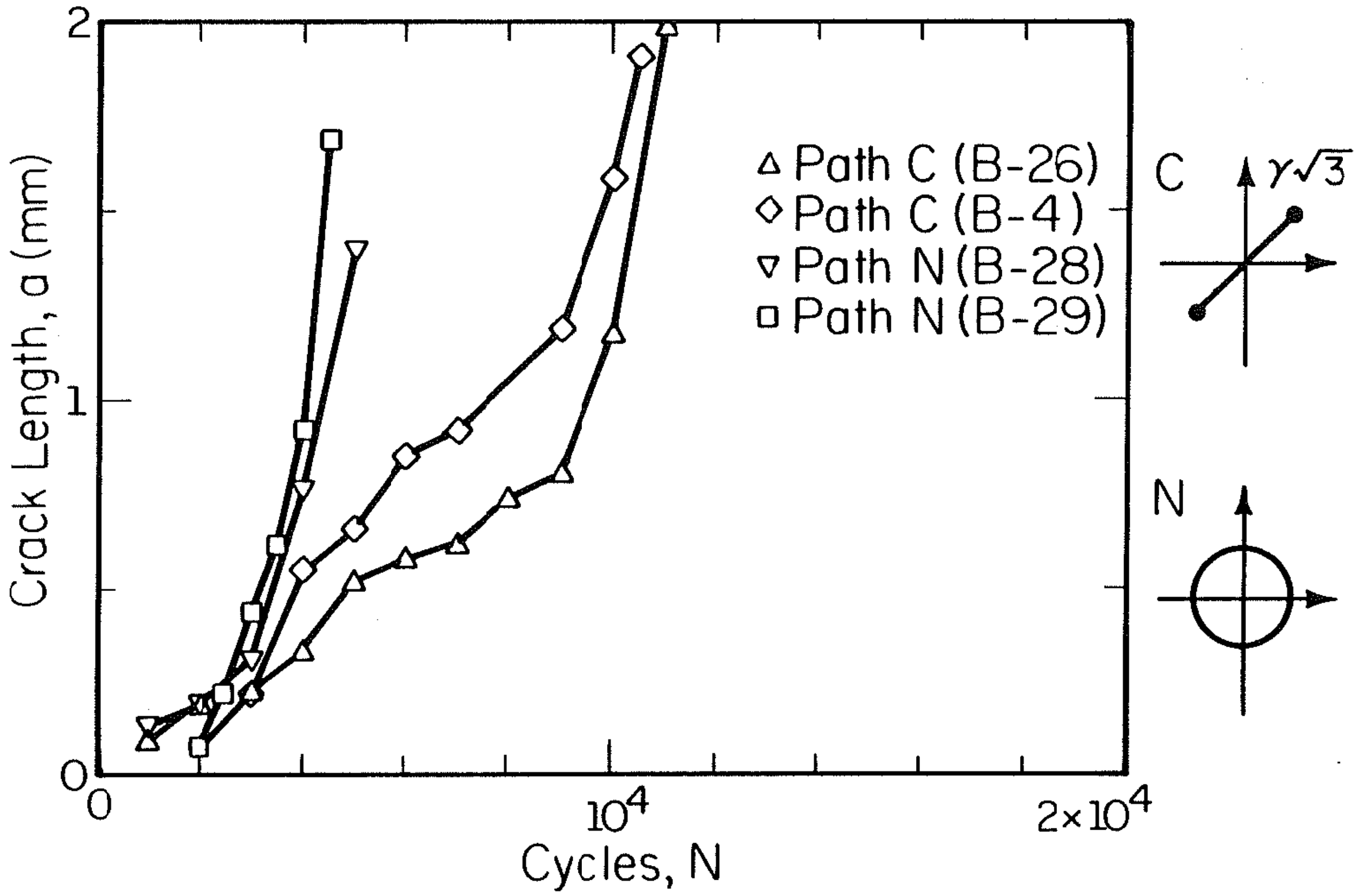

Figure 23 Strain Paths C and N, $\bar{\epsilon}$ = 0.005, Crack Growth Comparison

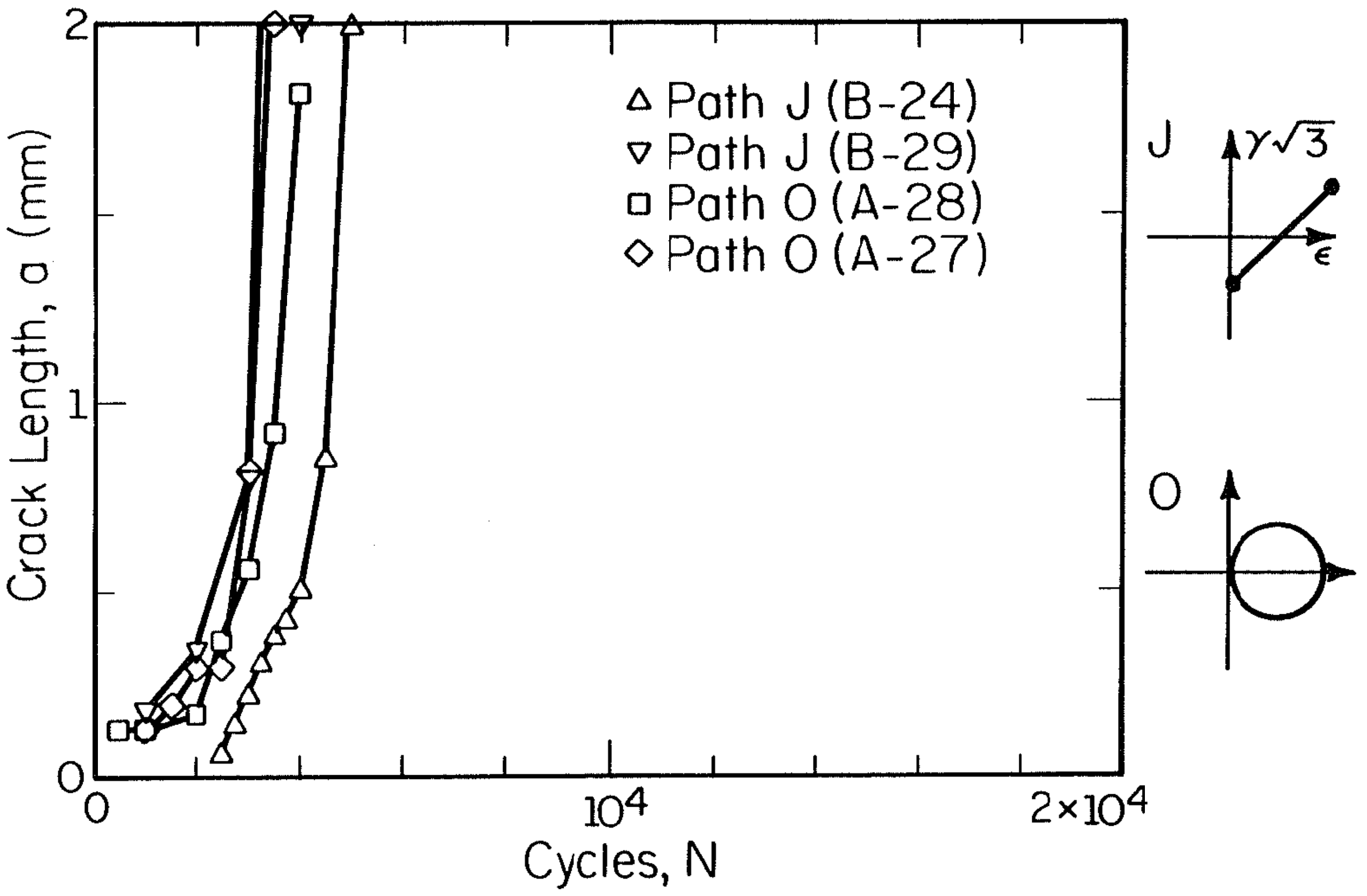

Figure 24 Strain Paths J and O, $\bar{\epsilon} = 0.005$, Crack Growth Comparison

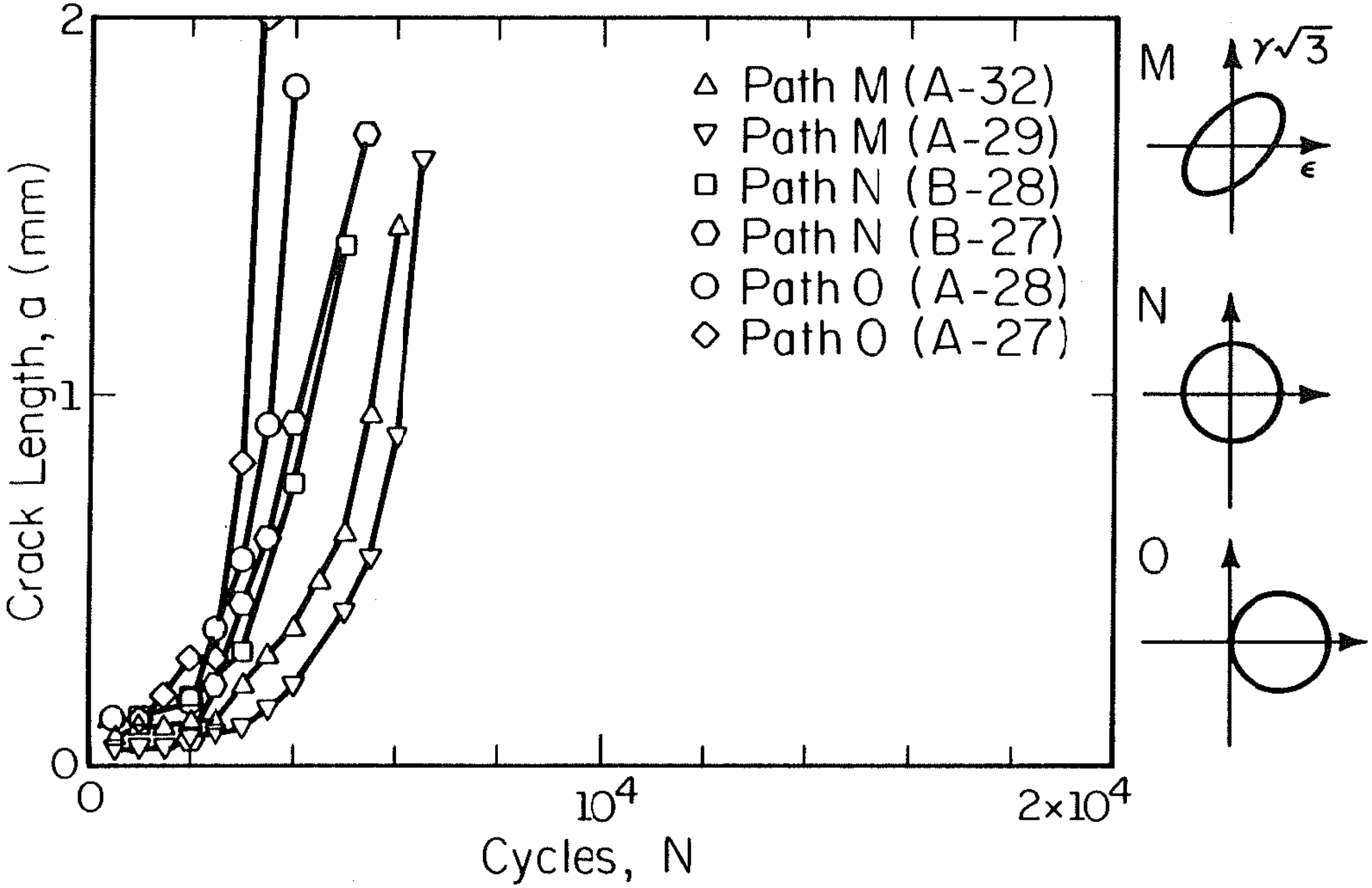

Figure 25 Strain Paths M, N, and O, $\bar{\varepsilon}$ = 0.005, Crack Growth Comparison

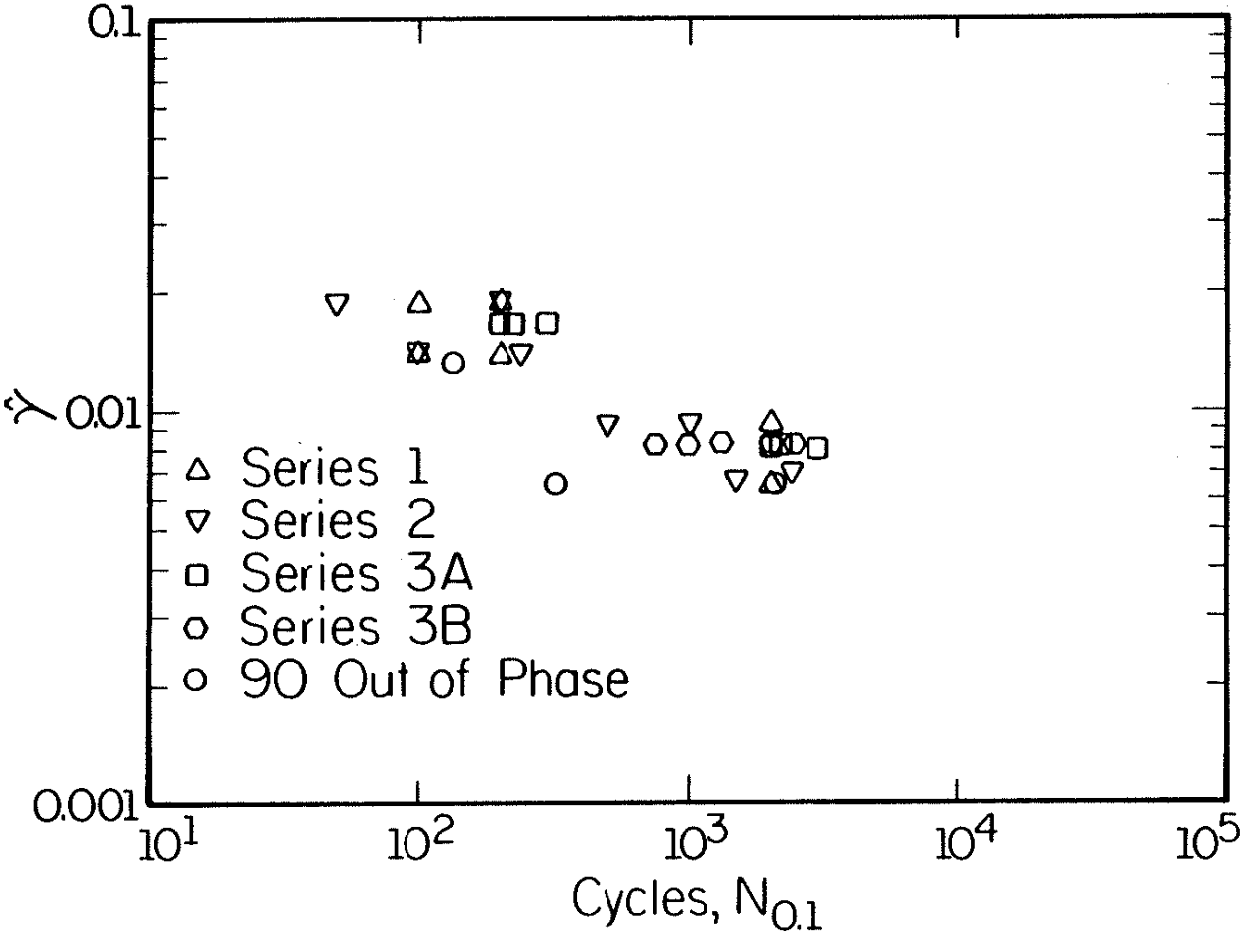

Figure 26 Maximum Shear Strain Amplitude versus 0.1 mm Crack Life

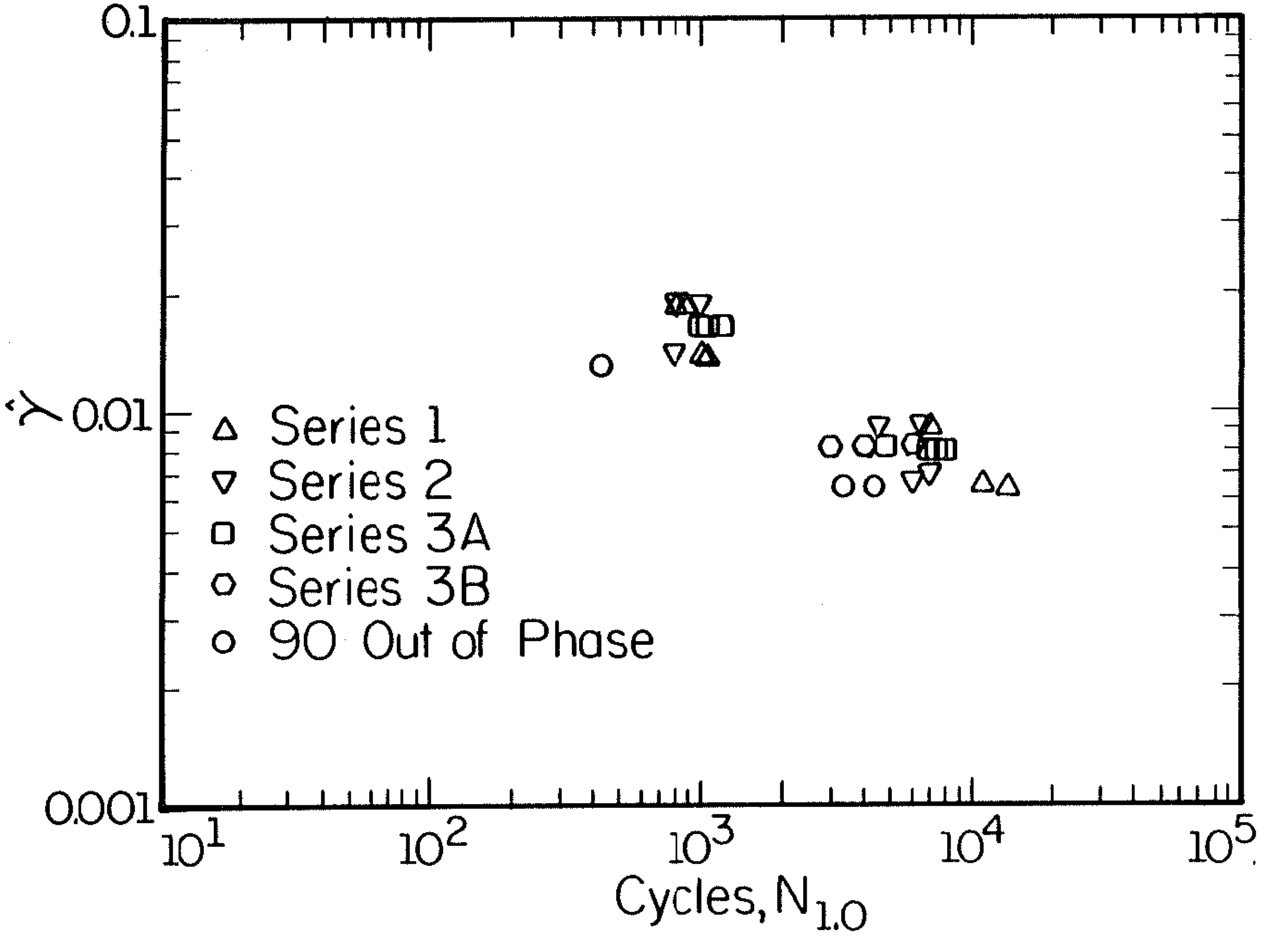

Figure 27 Maximum Shear Strain Amplitude versus 1.0 mm Crack Life

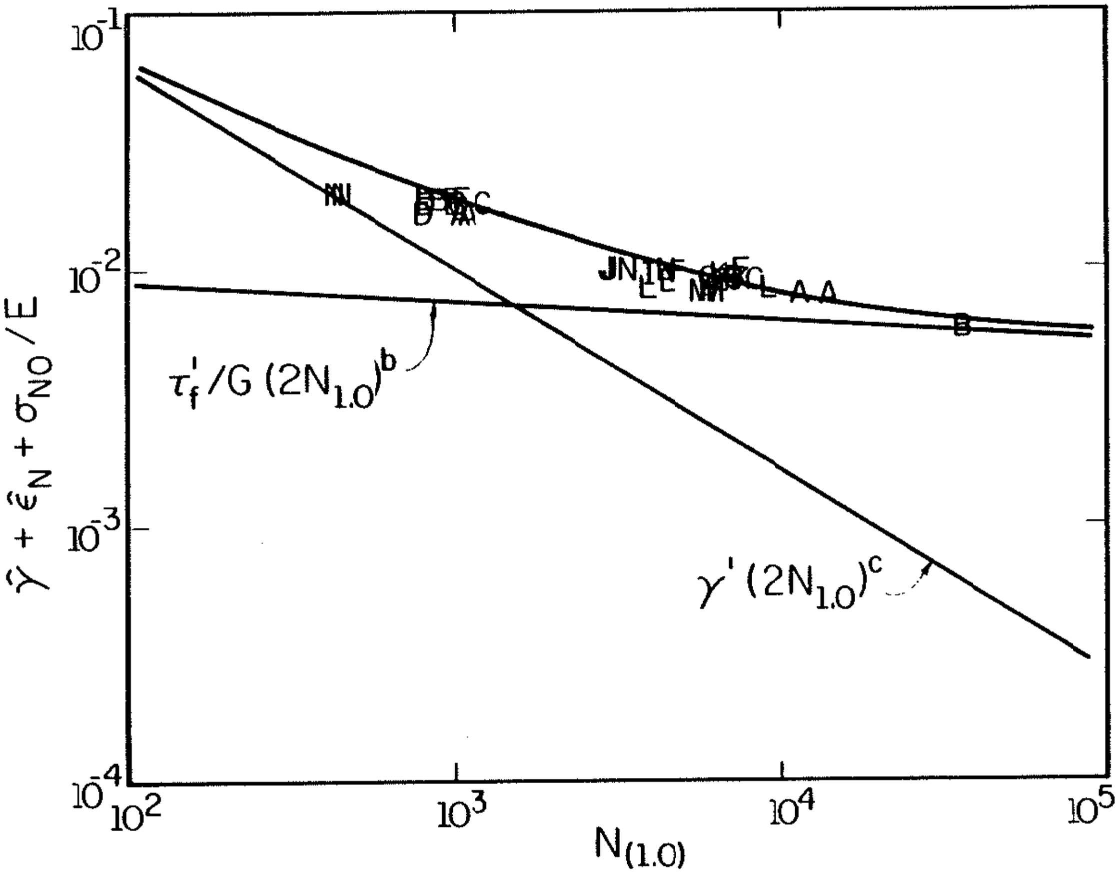

Figure 28 Torsional Baseline Data

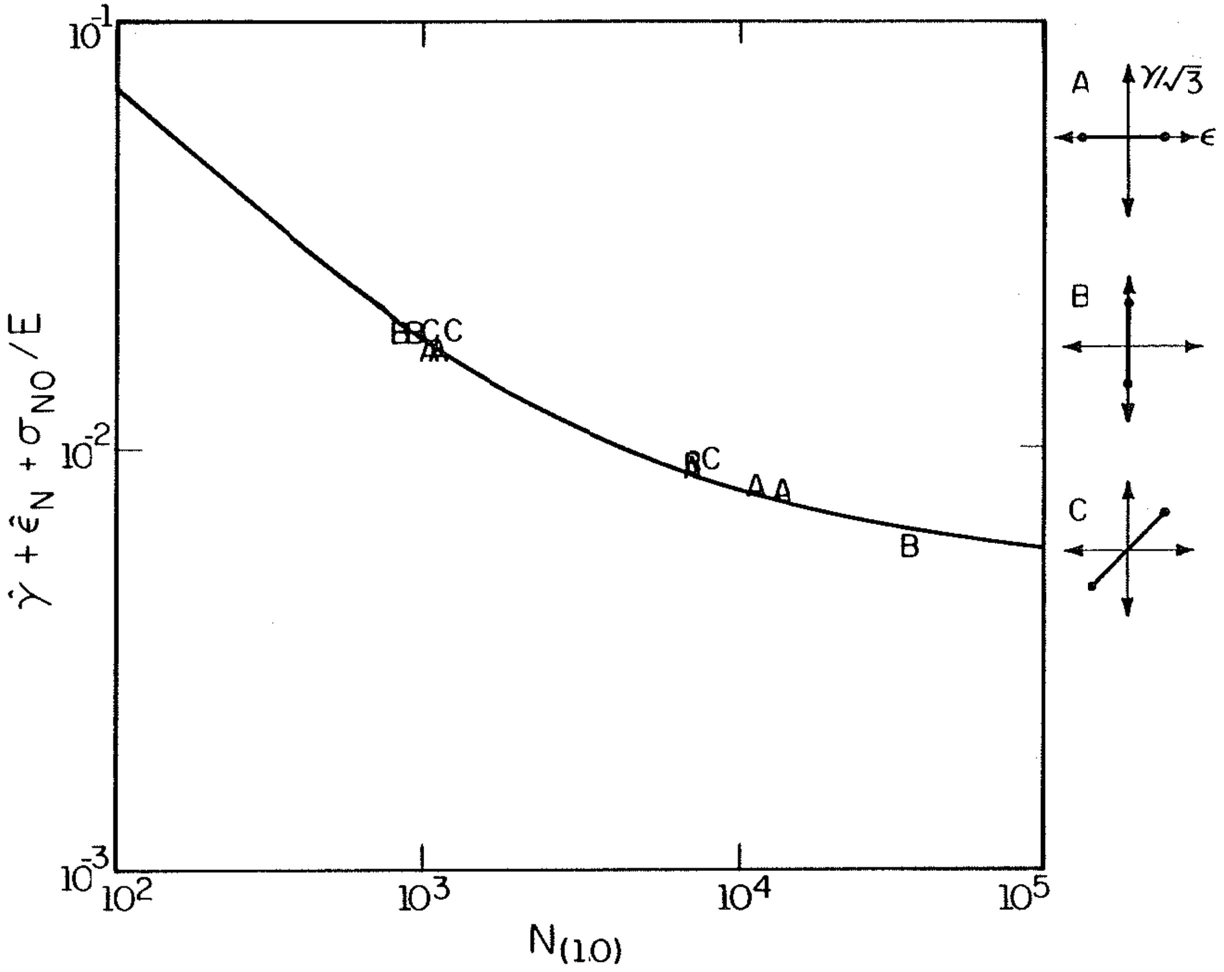

Figure 29 Data Correlation for Strain Paths A-C

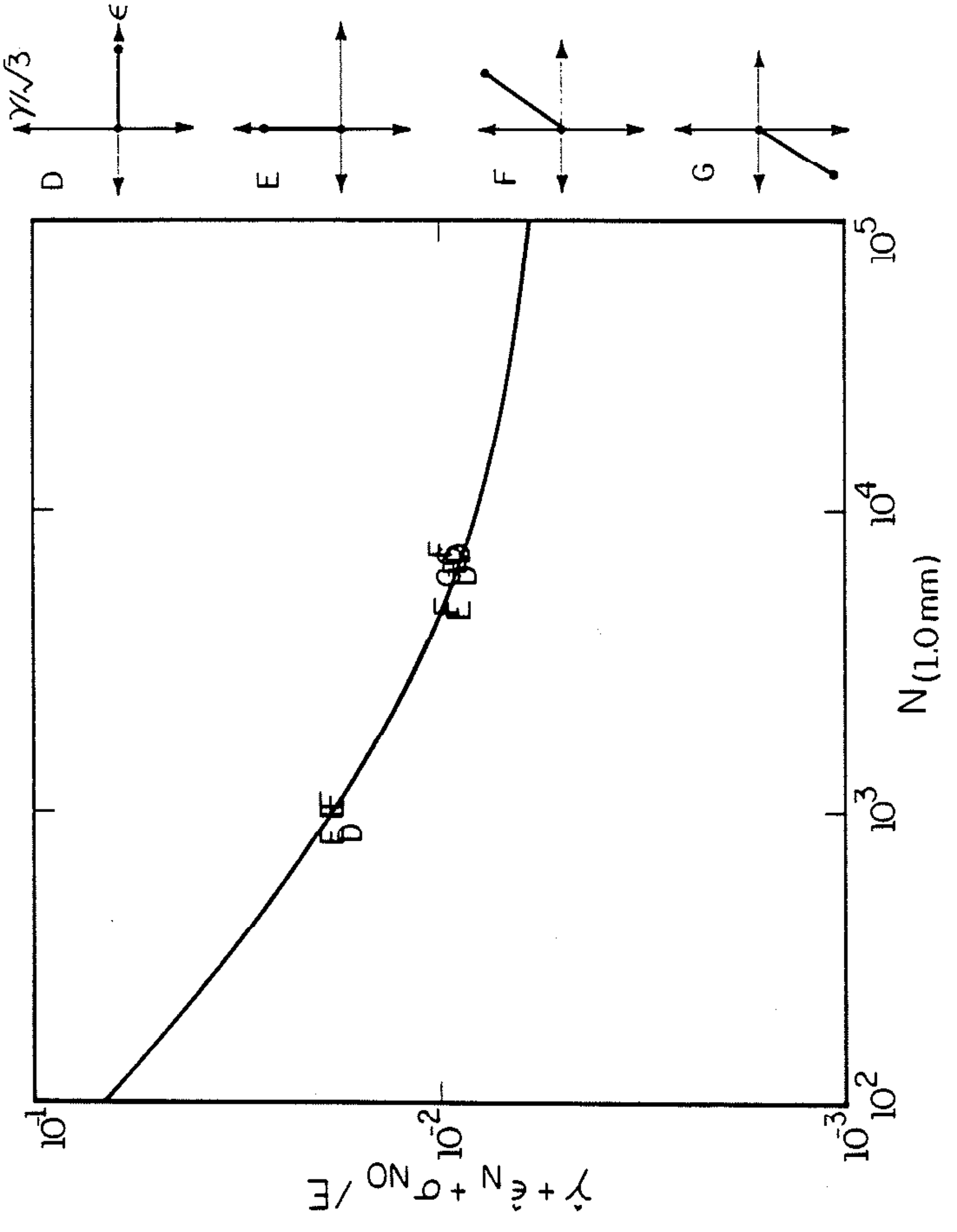

Figure 30 Data Correlation for Strain Paths D-G

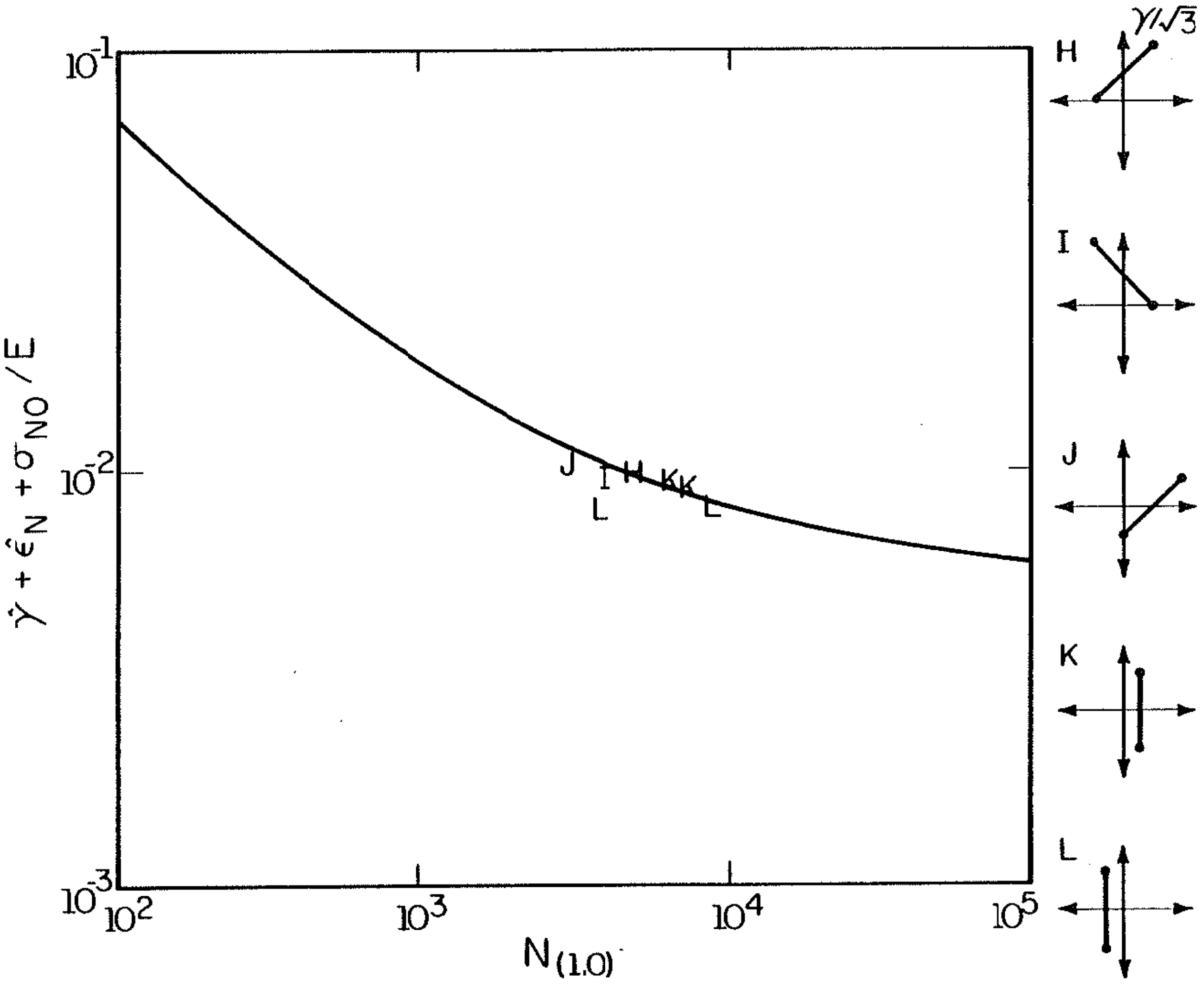

Figure 31 Data Correlation for Strain Paths H-L

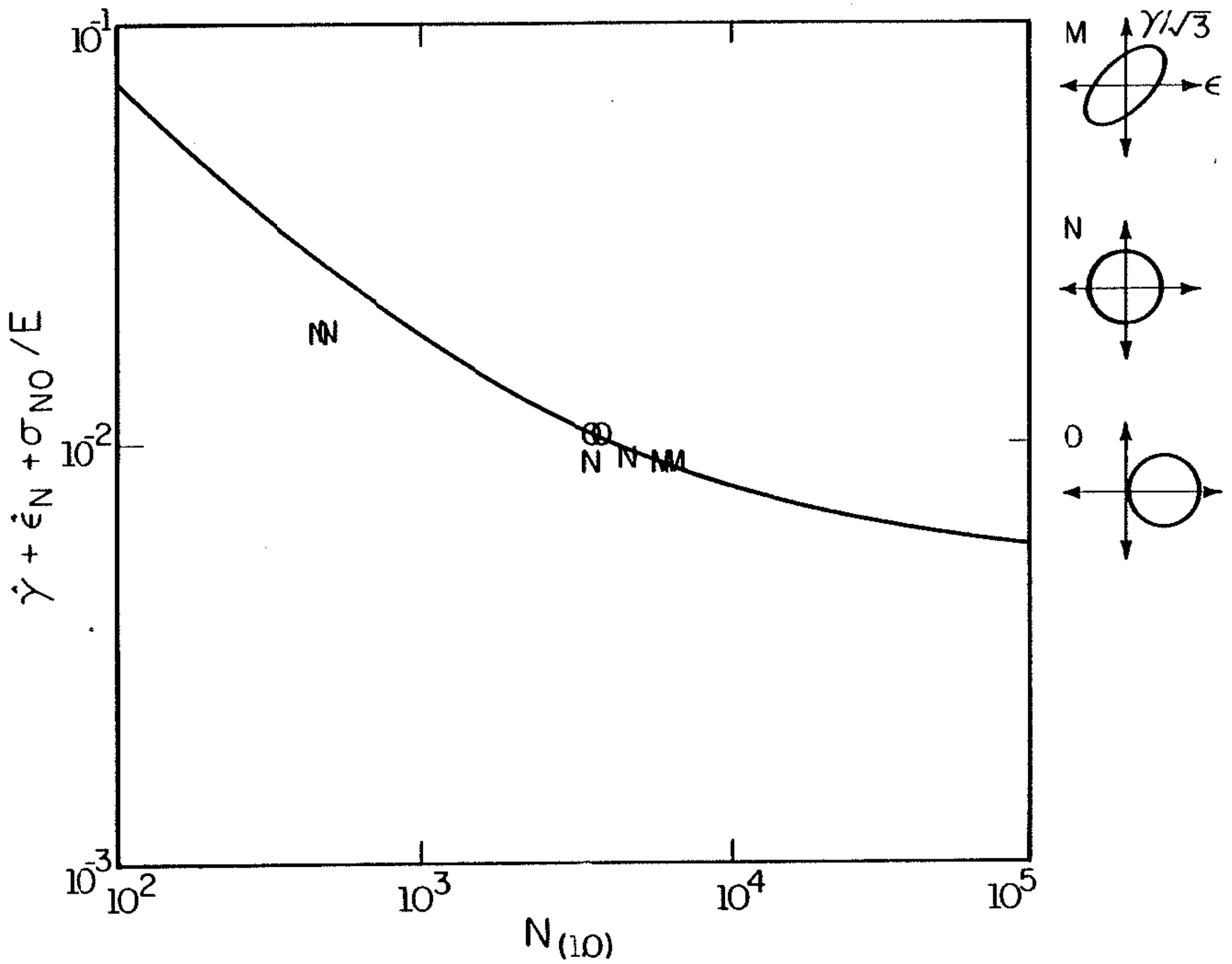

Figure 32 Data Correlation for Strain Paths M-O

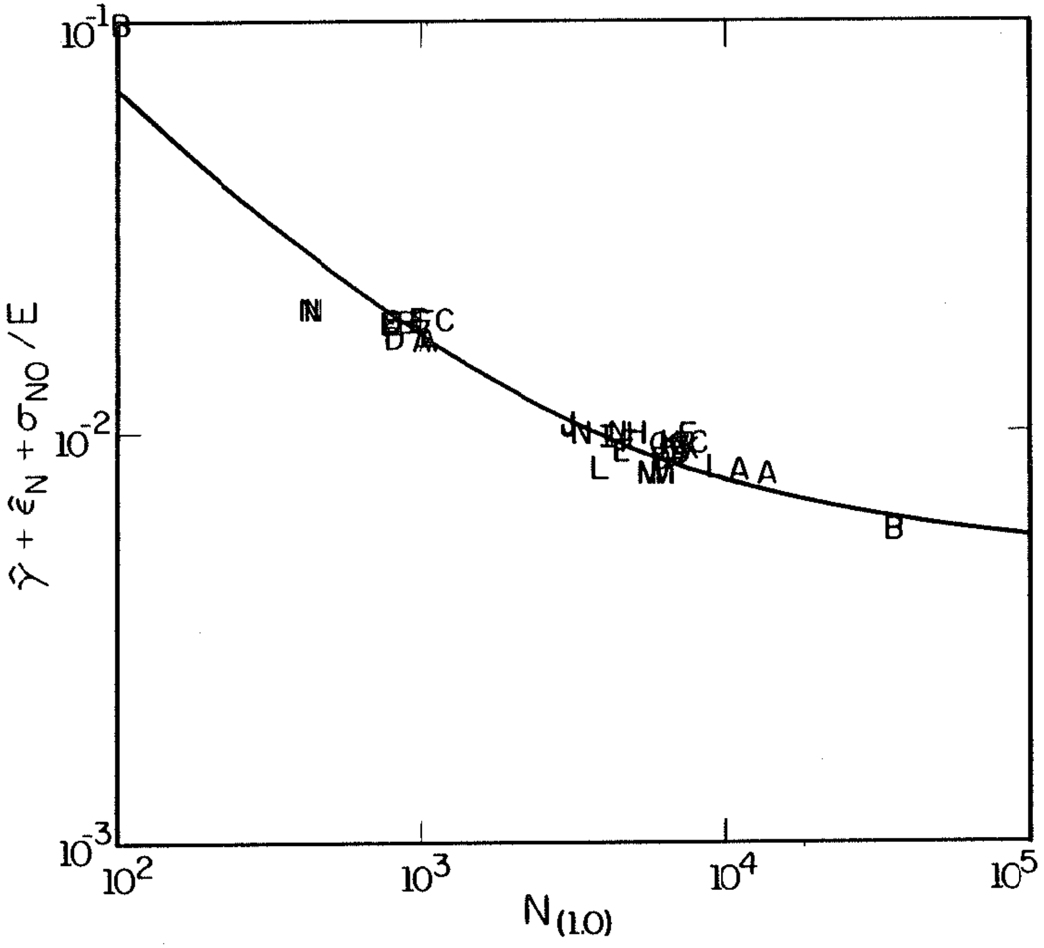

Figure 33 Data Correlation for all Strain Paths

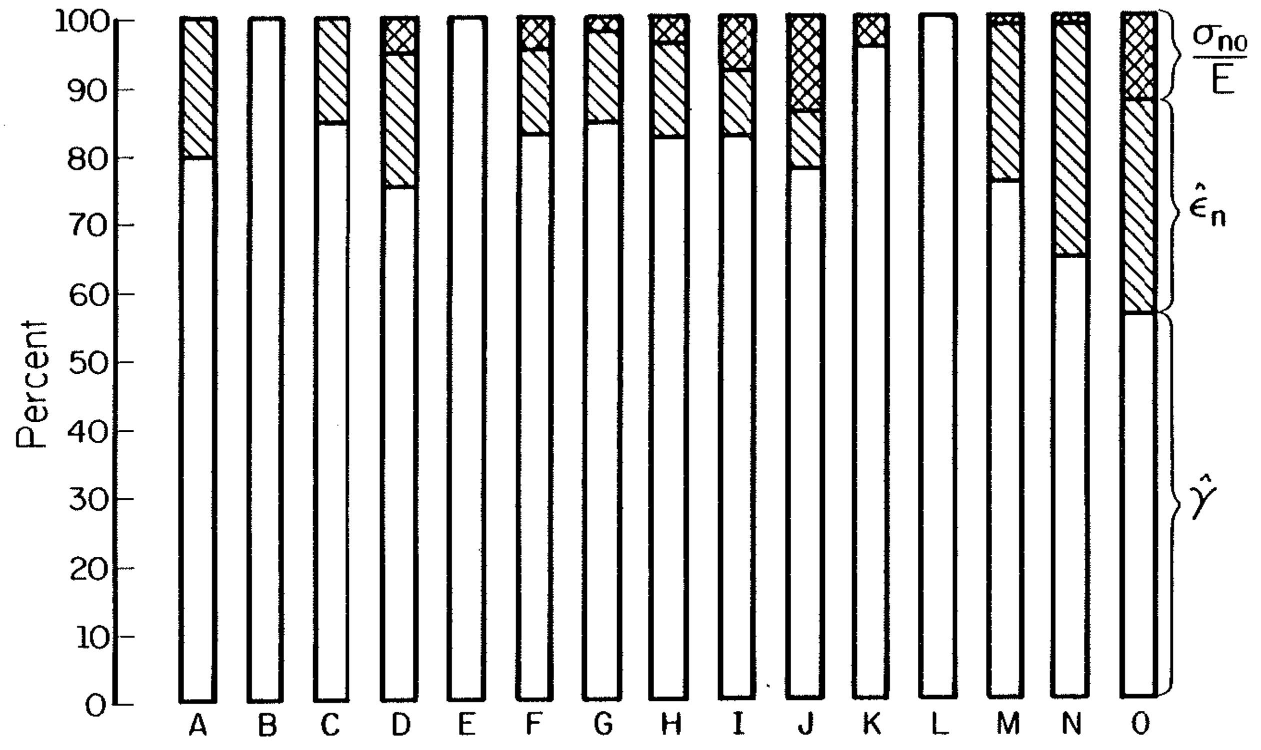

Figure 34 Percent Damage Comparison for all Strain Paths at $\bar{\varepsilon}$= 0.005

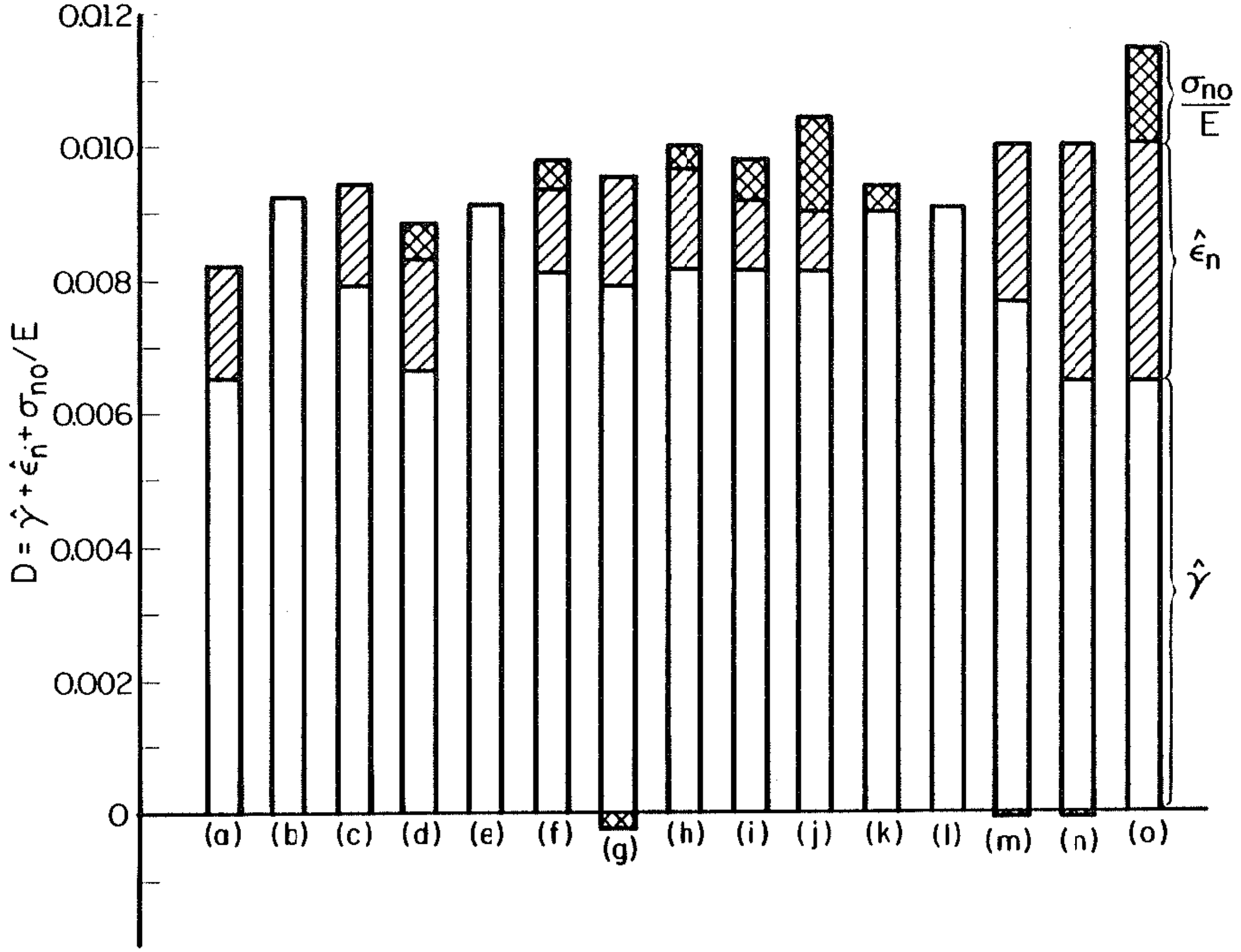

Figure 35 Damage Comparison for all Strain Paths at $\overline{\varepsilon} = 0.005$

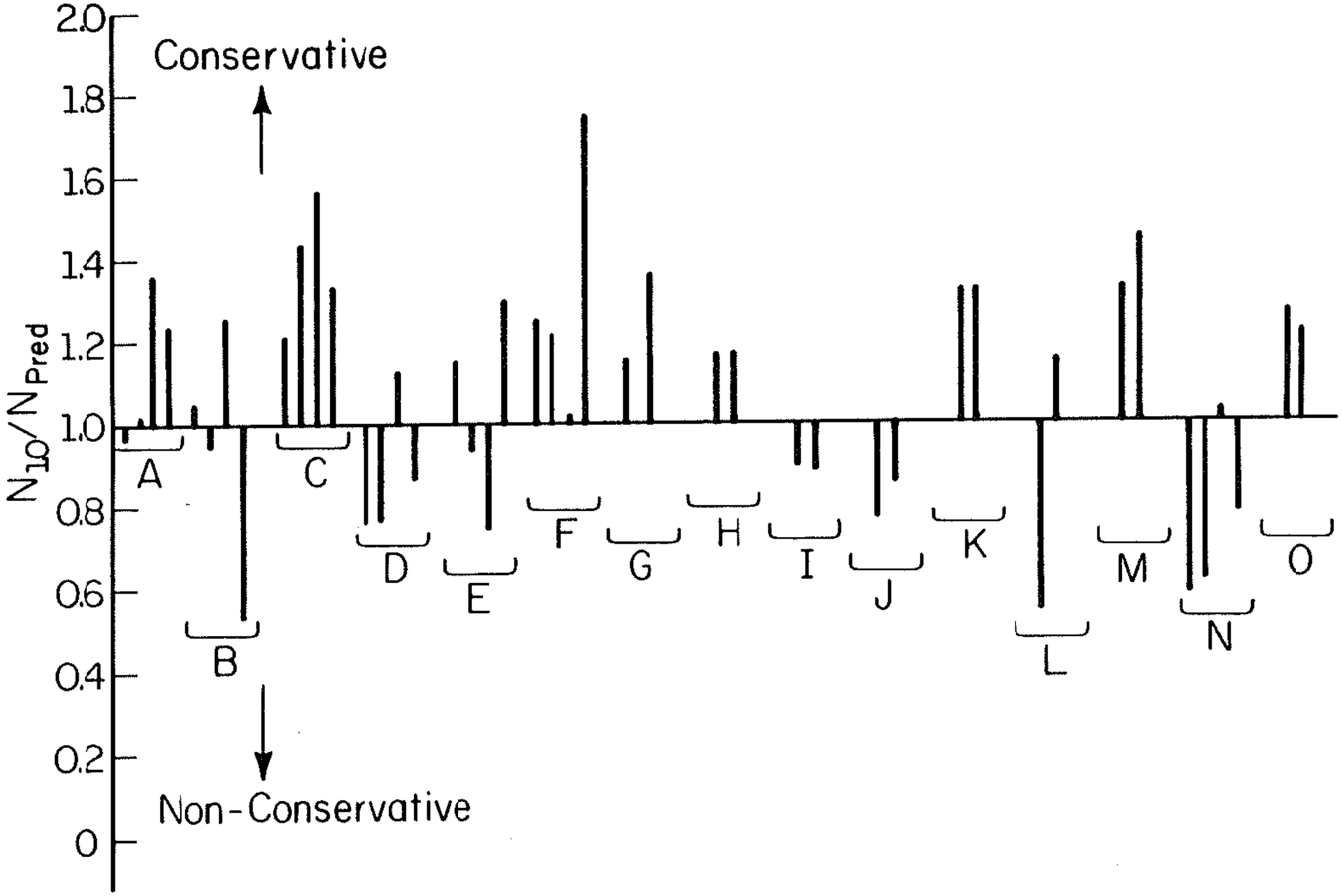

Figure 36 Comparison of Actual and Predicted Fatigue Lives

APPENDIX A

LIST OF FIGURES

APPENDIX A: COMPARISON OF TWO CRITICAL SHEAR PLANE THEORIES

Two critical shear planes for fatigue crack growth, $\hat{\gamma}$ and γ^*, will be examined graphically. Brown and Miller [18] expounded the following representation for a critical shear plane:

$$\hat{\gamma} = (\varepsilon_1 - \varepsilon_3)/2. \qquad (1)$$

Lohr and Ellison [19] proposed an alternate formulation:

$$\gamma^* = (\varepsilon_1 - \varepsilon_2)/2. \qquad (2)$$

Theoretical background for the selections will not be discussed. Two tests, simple tension and torsion, will be employed to contrast the two theories.

Mohr's three-dimensional representation for strain (Fig. A.1) is shown for both tests. The maximum shear strain, γ_{max}, is always at an angle of 90° to the principle strain axis on Mohr's circle. This corresponds to a 45° rotation from the principle strain axes of the specimen. (Note: the principle strain axes and the axis of the specimen coincide only for simple tension). The principle strains, ε_1 and ε_3, define the $\hat{\gamma}$ plane. Thus, $\hat{\gamma}$ plane is a 45° rotation on the specimen from ε_1 and ε_3 axes (Fig. A.2a). The γ^* plane is similarly defined at 45° from the ε_1 and ε_2 axes (Fig. A.2b). Identification of either the $\hat{\gamma}$ or γ^* plane with regard to specimen orientation for any particular strain state is a two-step procedure:

(1) Definition of the principle strain axes relative to both the axis and surface of the specimen.

(2) Location of the $\hat{\gamma}$ or γ^* plane relative to the principle strain axes.

Two perpendicular shear planes exist for either theory. For clarity only one $\hat{\gamma}$ and one γ^* plane will be referred to in the ensuing discussion.

In simple tension, the strains perpendicular to the applied strain, ε, are all equal to $-\nu\varepsilon$. Orientation of the principle strain axes has only one constraint, that ε_1 be parallel to the specimen axes (Fig. A.2c). An infinite number of equivalent orientations of ε_2 and ε_3 may be achieved by rotation about the ε_1 axis. Peterson [22] demonstrated that this could be interpreted as planes tangent to a 45° cone (Fig. A.3). The planes, $\hat{\gamma}$ and γ^*, are indistinguishable in simple tension. Therefore, the two theories cannot be contrasted with this test.

In torsion, the ε_2 direction is perpendicular to the specimen surface. Other principle strains, ε_1 and ε_3 are oriented at 45° from the specimen axis (Fig. A.2d) in the surface plane. The torsional strain state fixes the location of the principle strain axes to one position. Unique orientations of the $\hat{\gamma}$ and γ^* planes for torsion (Fig. A.4) allow comparison of the two theories.

Experimental crack observations will allow the appropriate choice of damage parameter to be made for a material that displays a shear crack growth direction.

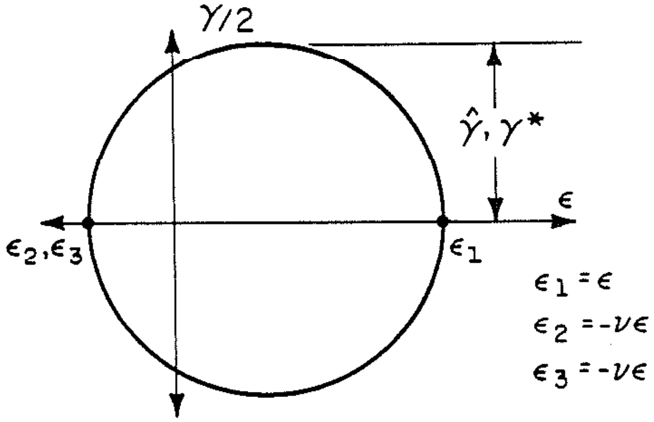

(a) Tension

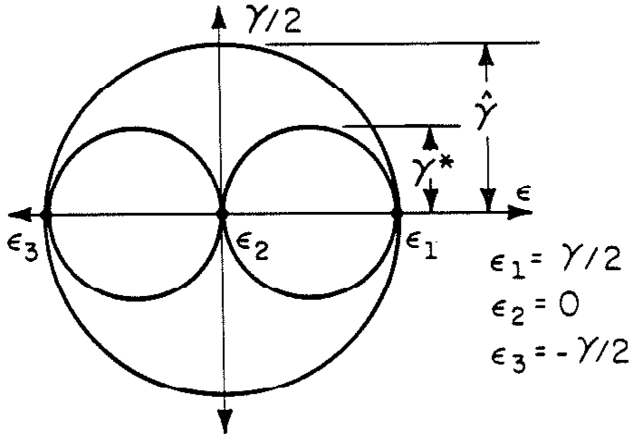

(b) Torsion

Figure A.1 Mohr's Strain Circle for Tension and Torsion

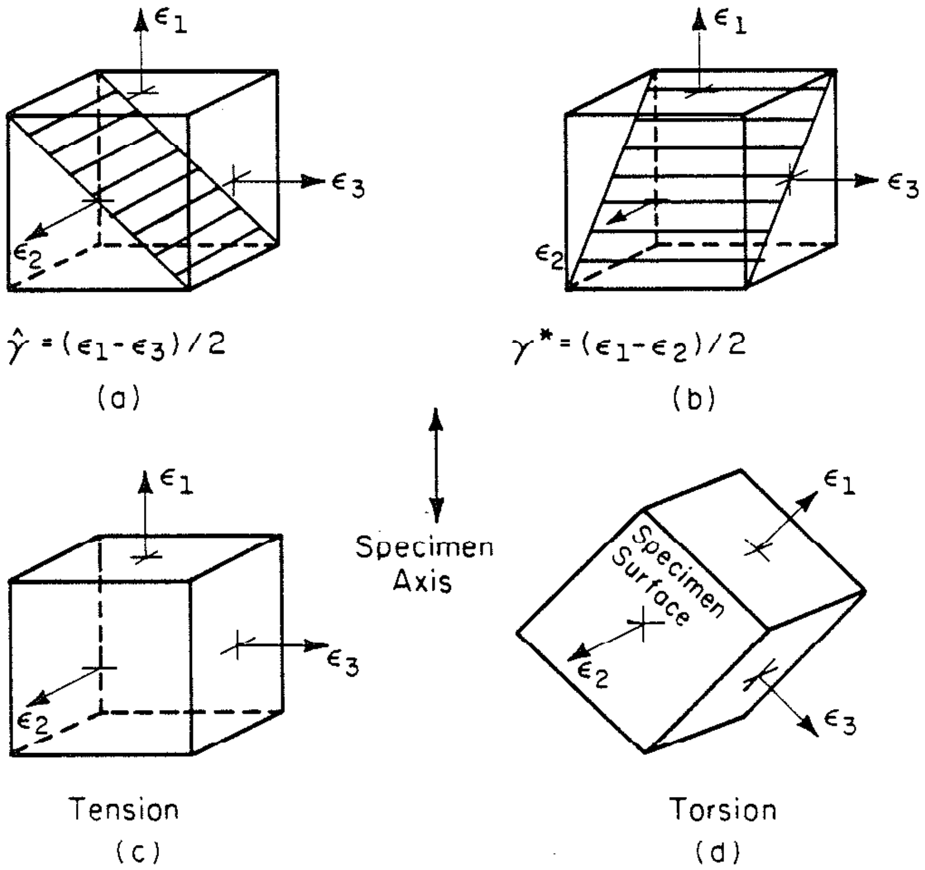

$\hat{\gamma} = (\epsilon_1 - \epsilon_3)/2$
(a)

$\gamma^* = (\epsilon_1 - \epsilon_2)/2$
(b)

Tension
(c)

Torsion
(d)

Figure A.2 Principle Axis Orientation for $\hat{\gamma}$, γ^* Tension and Torsion

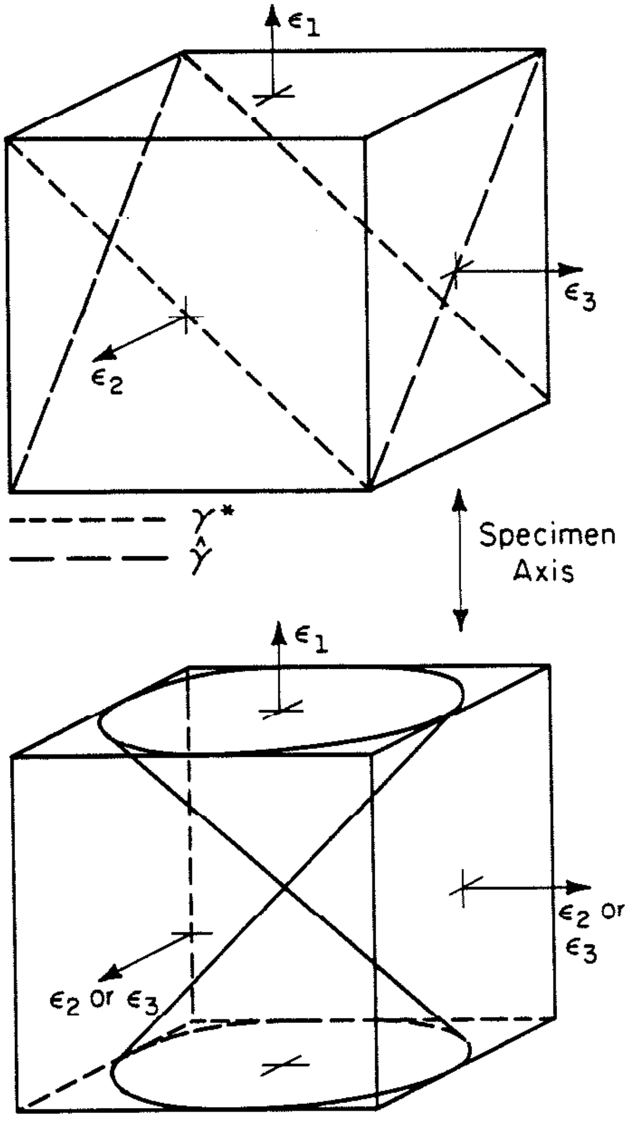

Figure A.3 Graphical Comparison of $\hat{\gamma}$ and γ^* for a Tension Test

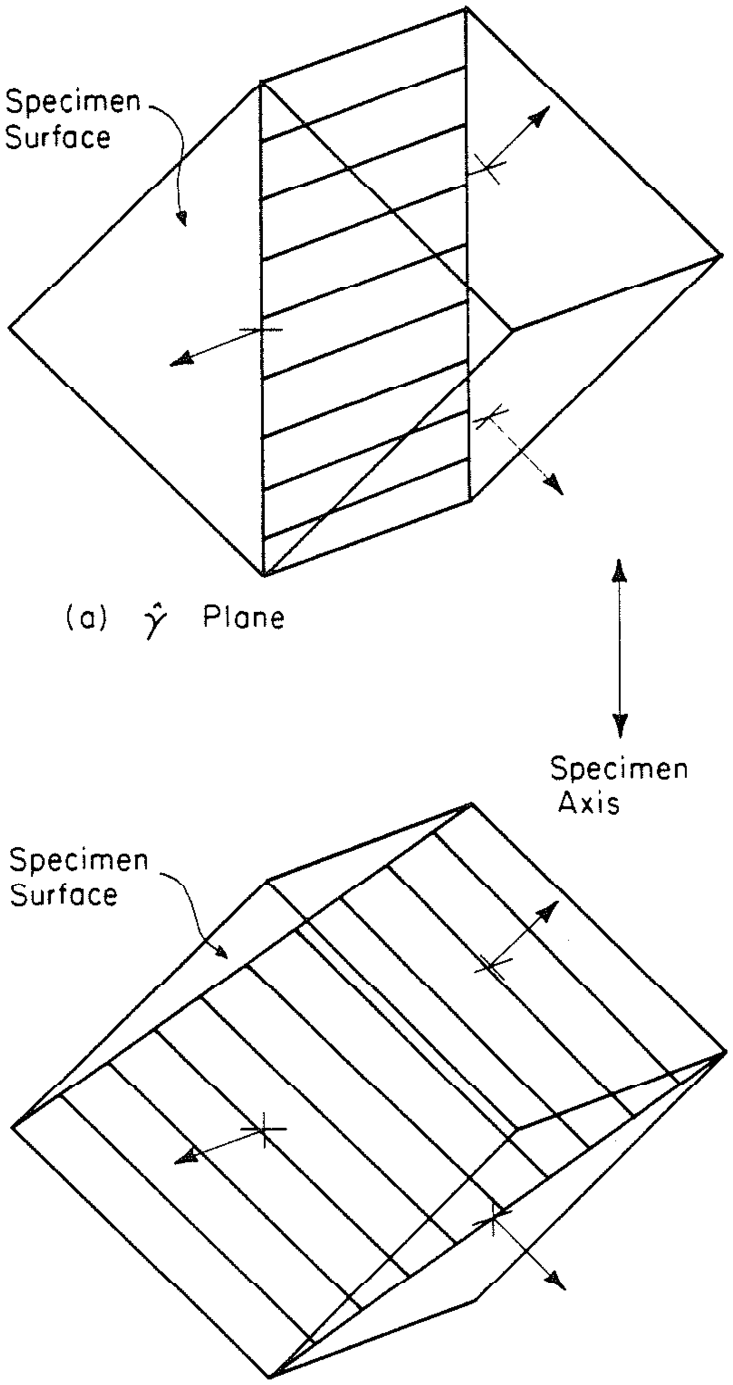

(a) $\hat{\gamma}$ Plane

(b) γ^* Plane

Figure A.4 Graphical Comparison of $\hat{\gamma}$ and γ^* for a Torsion Test

APPENDIX B

LIST OF FIGURES

APPENDIX B: PLANE ROTATION DOCUMENTATION

B.I Introduction

Tensor rotation was employed in calculations to resolve the stresses and strains on a given plane of the thin-walled cylinder. Plane stress is assumed throughout the ensuing discussion. Consider the coordinate system shown in Fig. B.1.

With the assumption of plane stress, the stress and strain tensors take the following form:

$$\tau_{ij} = \begin{matrix} 0 & -\tau & 0 \\ -\tau & \sigma & 0 \\ 0 & 0 & 0 \end{matrix} \quad ; \quad \varepsilon_{ij} = \begin{matrix} -\nu\varepsilon & -\frac{\gamma}{2} & 0 \\ -\frac{\gamma}{2} & \varepsilon & 0 \\ 0 & 0 & -\nu\varepsilon \end{matrix} \; .$$

The negative signs for τ_{12}, τ_{21}, ε_{12}, and ε_{21} are a result of the test system being of left-hand orientation, and our choice of coordinate system being right hand.

The normal to the surface may be defined as follows:

$$\hat{n} = A\hat{i} + B\hat{j} + C\hat{k} = n_i + n_j + n_k$$

where

$$A = \{\cos\psi \sin\phi + \cos\theta \cos\phi \sin\psi\}$$

$$B = \{-\sin\psi \sin\phi + \cos\theta \cos\phi \cos\psi\}$$

$$C = -\sin\theta \cos\phi .$$

The angles, ϕ, θ and ψ, are the three Euler angles. The order of rotation is: (1) ϕ about the $\hat{k}$ axis; (2) θ about the $\hat{i}$ axis; and (3) ψ about the $\hat{k}$ direction. The $\hat{j}$ direction is the reference direction for $\phi = 0$, $\theta = 0$, and $\psi = 0$.

B.II Stresses and Strains Normal to a Plane

$$\sigma_N = n_i \, \tau_{ij} \, n_j$$

$$= -2\tau \, AB + \sigma \, B^2.$$

Similarly:

$$\varepsilon_N = n_i \, \varepsilon_{ij} \, n_j$$

$$= \gamma \, AB + \varepsilon \, B^2 - \nu\varepsilon(A^2 + C^2).$$

B.III Shear Stresses and Strains

(a) In general:

$$\tau_i = \tau_{ij} \, n_j - \sigma_N \, n_i$$

$$= -(\tau \, B + \sigma_N \, A) \, \hat{i} + (\sigma \, B - \tau \, A - \sigma_N \, B) \, \hat{j} - \sigma_N \, C \, \hat{k}.$$

Similarly:

$$\begin{aligned}\gamma_i &= 2(\varepsilon_{ij}\, n_j - \varepsilon_N\, n_i)\\ &= 2\{-(\nu\varepsilon A + \gamma\, B/2 + \varepsilon_N\, A)\, \hat{i}\\ &\quad +(-\gamma\, A/2 + \varepsilon B - \varepsilon_N\, B)\, \hat{j}\\ &\quad -C\, (\nu\varepsilon + \varepsilon_N)\, \hat{k}\}.\end{aligned}$$

(b) Shear Directions

The tangent to the surface on a plane defined by $\hat{n}$ is:

$$\hat{t}_1 = \sin(\phi - 90^\circ)\, \hat{i} + \cos(\phi + 90^\circ)\, \hat{j},$$

and through the surface is in the direction:

$$\begin{aligned}\hat{t}_2 &= C\cos(\phi + 90^\circ)\, \hat{i} - C\sin(90^\circ + \phi)\, \hat{j}\\ &\quad + \{B\sin(\phi + 90^\circ) - A\cos(\phi + 90^\circ)\}\, \hat{k}\\ &= \hat{t}_1 \times \hat{n}.\end{aligned}$$

(c) Hence the shear stresses and strains tangent to the surface are:

$$\begin{aligned}\tau_1 &= \tau_i \cdot \hat{t}_1\\ &= -(\tau B + \sigma_N\, A)\sin(\phi + 90^\circ)\end{aligned}$$

$$+(\sigma B - \tau A - \sigma_N B) \cos(\phi + 90^{\circ})$$

$$\gamma_1 = \gamma_i \cdot \hat{\tau}_1$$

$$= 2\{-(\nu\varepsilon A + \gamma B/2 + \varepsilon_N A) \sin(\phi + 90^{\circ})$$

$$+ (-\gamma A/2 + \varepsilon B - \varepsilon_N B) \cos(\phi + 90^{\circ}),$$

(d) and the shear stresses and strains through the surface are:

$$\tau_2 = \tau_i \cdot \hat{\tau}_2$$

$$= -C(\tau B + \sigma_N A) \cos(\phi + 90^{\circ})$$

$$-C(\sigma B - \tau A - \sigma_N B) \sin(\phi + 90^{\circ})$$

$$-\sigma_N C(B \sin(\phi + 90^{\circ}) - A \cos(\phi + 90^{\circ}))$$

$$\gamma 2 = \gamma i \cdot \hat{\tau} 2$$

$$= 2\{-C(\nu\varepsilon A + \gamma B/2 + \varepsilon_N A) \cos (\phi + 90^{\circ})$$

$$+ C(-\gamma A/2 + \varepsilon B - \varepsilon_N B) \sin(\phi + 90^{\circ})$$

$$- C(\nu\varepsilon + \varepsilon_N) (B \sin(\phi + 90^{\circ}) - A \cos(\phi + 90^{\circ}).$$

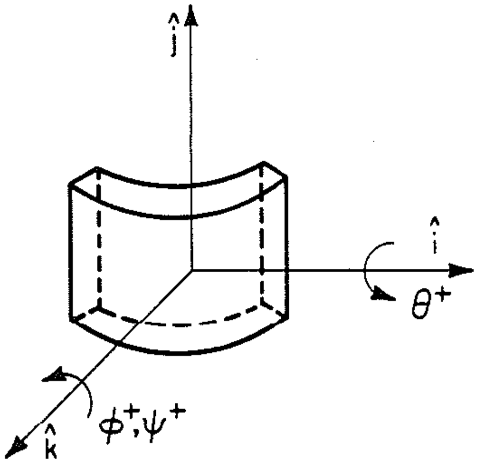

Figure B.1 Coordinate System

APPENDIX C: SURFACE CRACK DIRECTION OBSERVATIONS

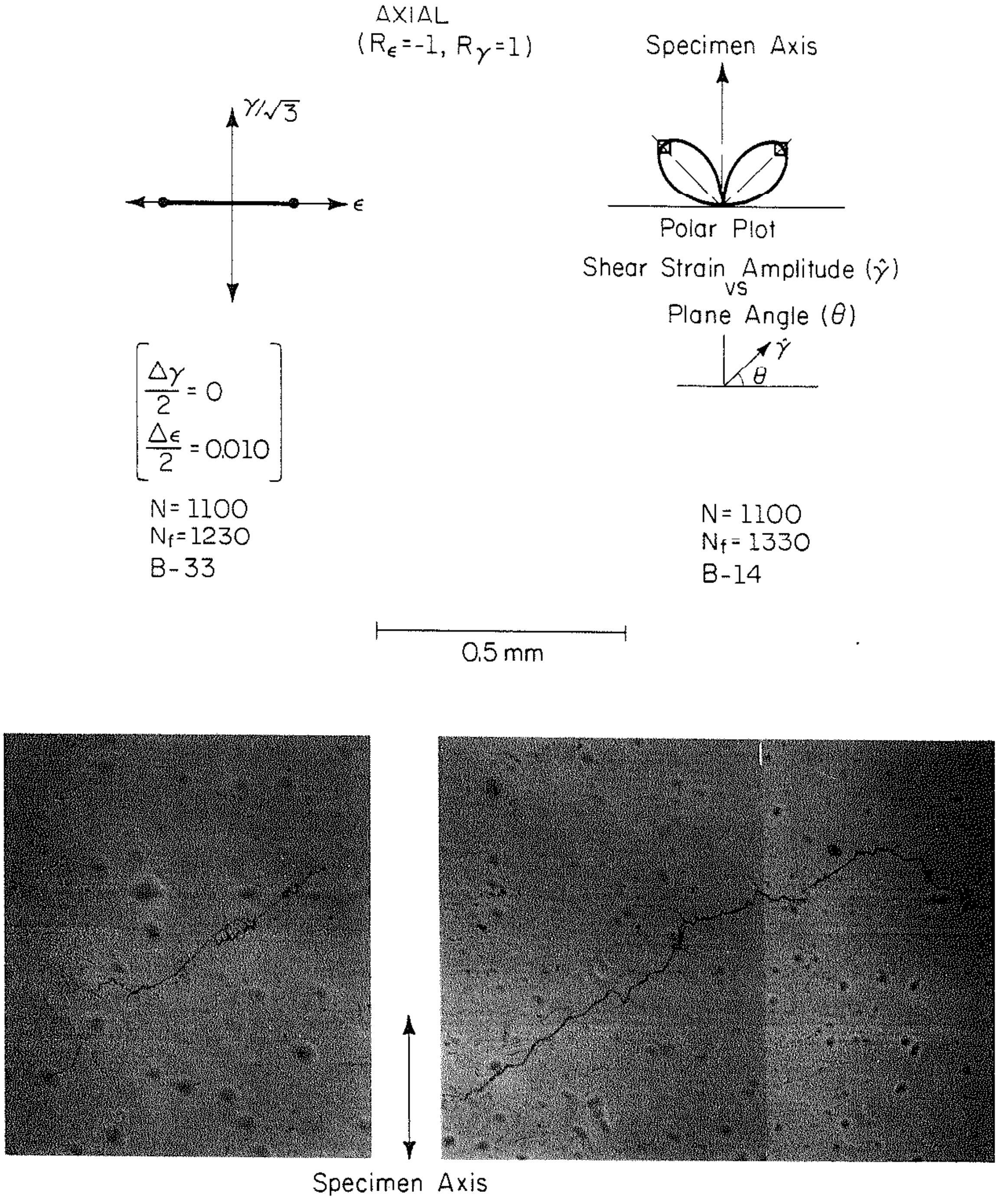

Figure C.1 Strain Path A, $\bar{\epsilon}$ = 0.010

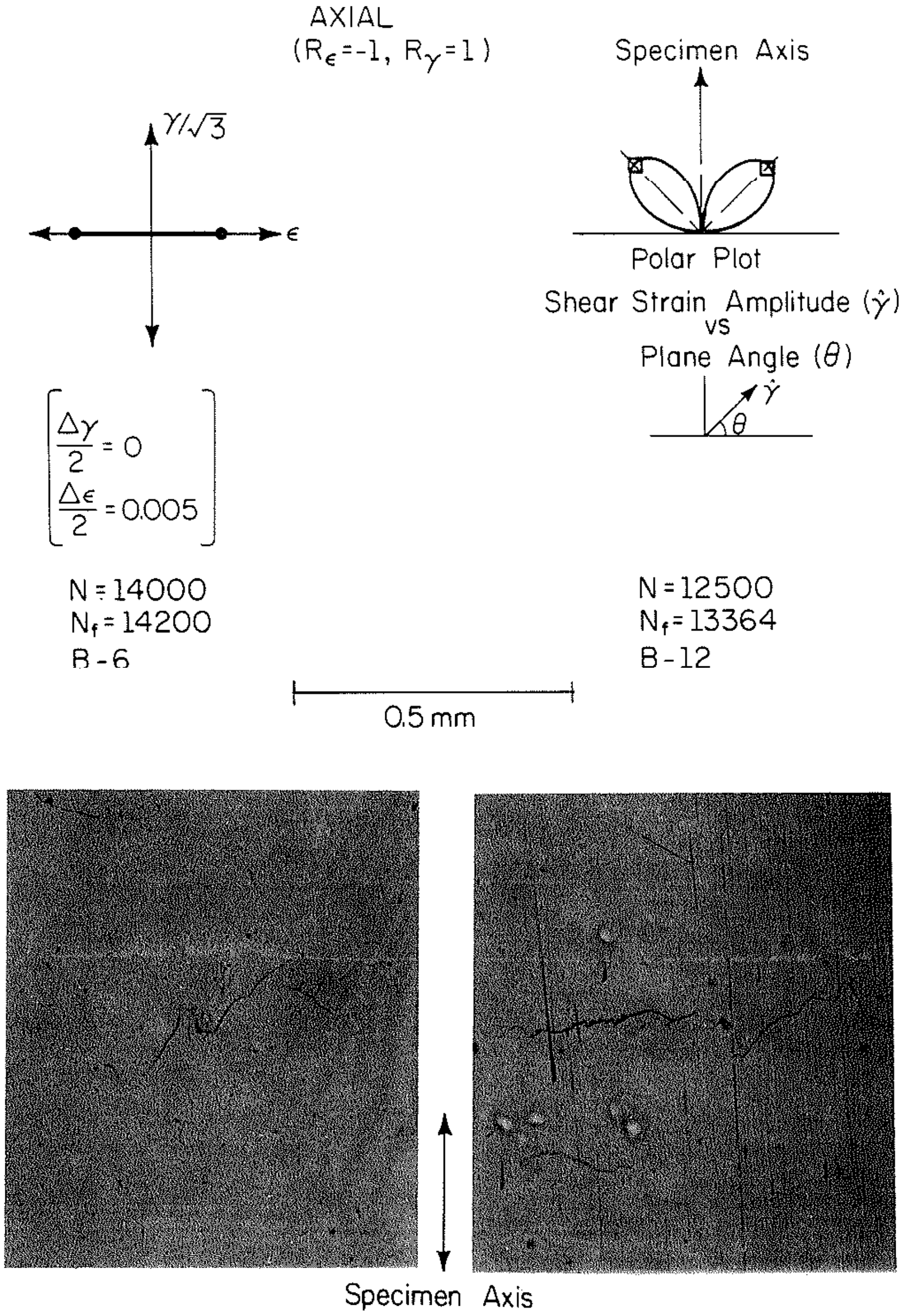

Figure C.2 Strain Path A, $\bar{\epsilon} = 0.005$

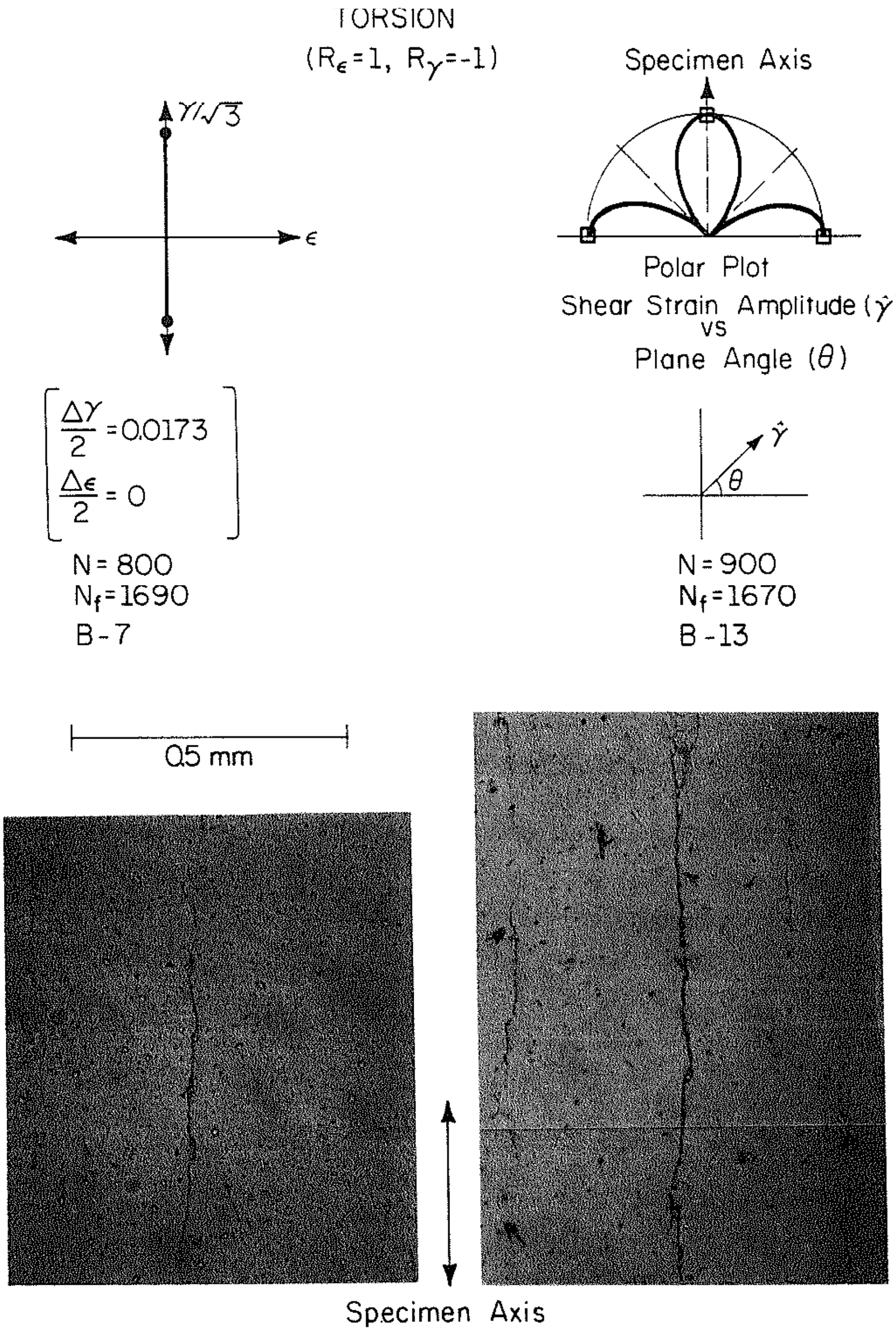

Figure C.3 Strain Path B, $\bar{\epsilon} = 0.010$

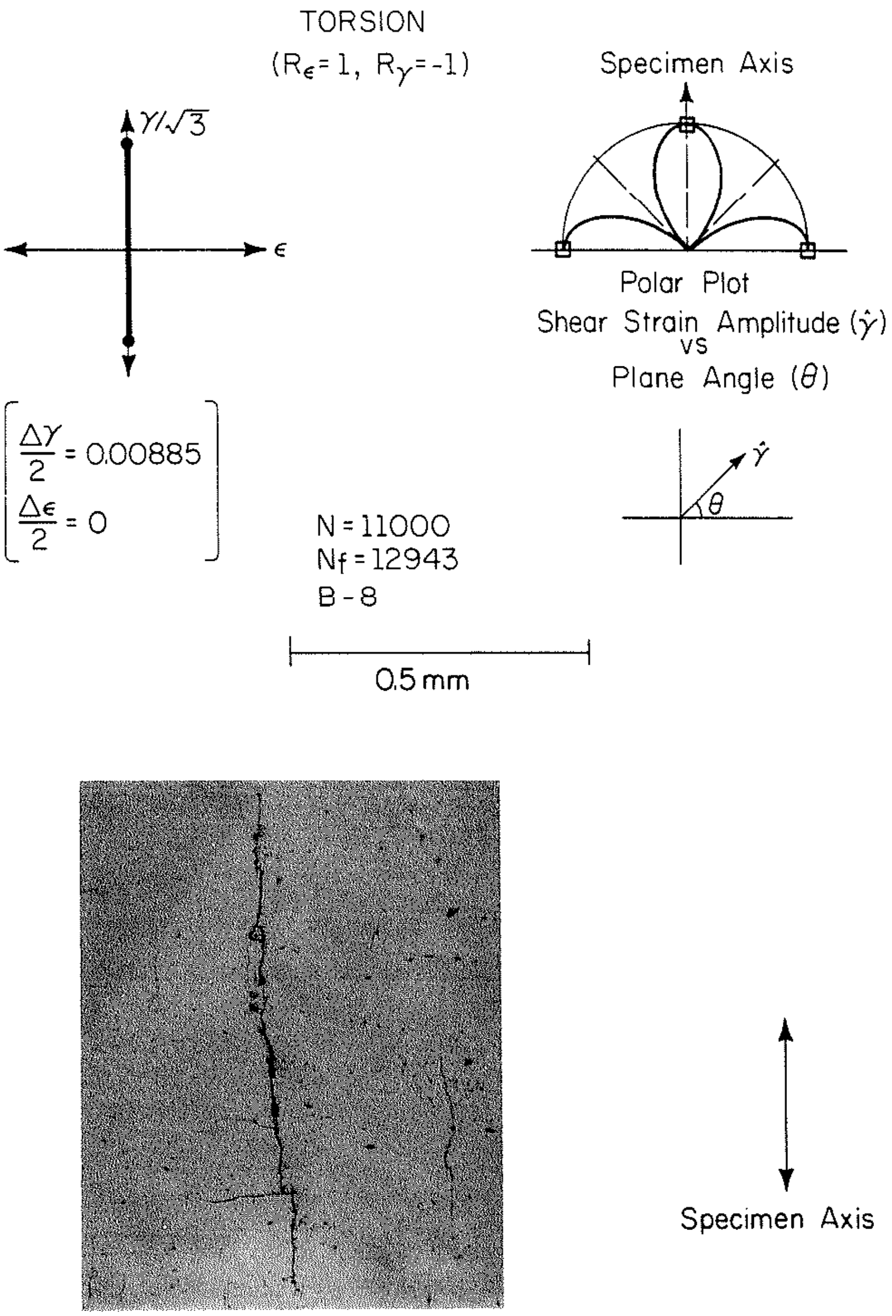

Figure C.4 Strain Path B, $\bar{\varepsilon}$ = 0.005

TORSION

$(R_\epsilon=1,\ R_\gamma=-1)$

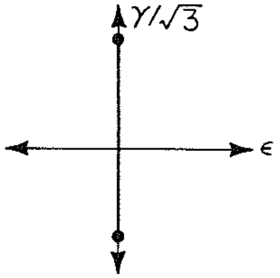

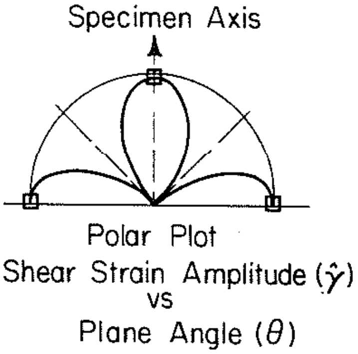

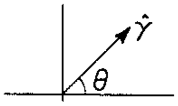

$$\left[\begin{array}{l}\frac{\Delta\gamma}{2}=0.0054\\ \frac{\Delta\epsilon}{2}=0\end{array}\right]$$

N = 40,000
N_f = 41,400
A-35

N = 30,000
N_f = 45,200
A-30

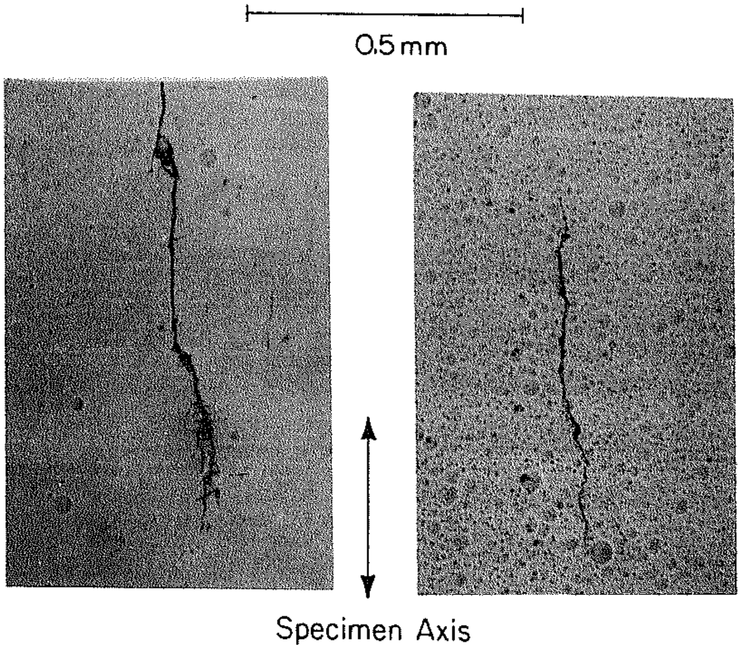

Figure C.5 Strain Path B, $\bar{\epsilon}$ = 0.003

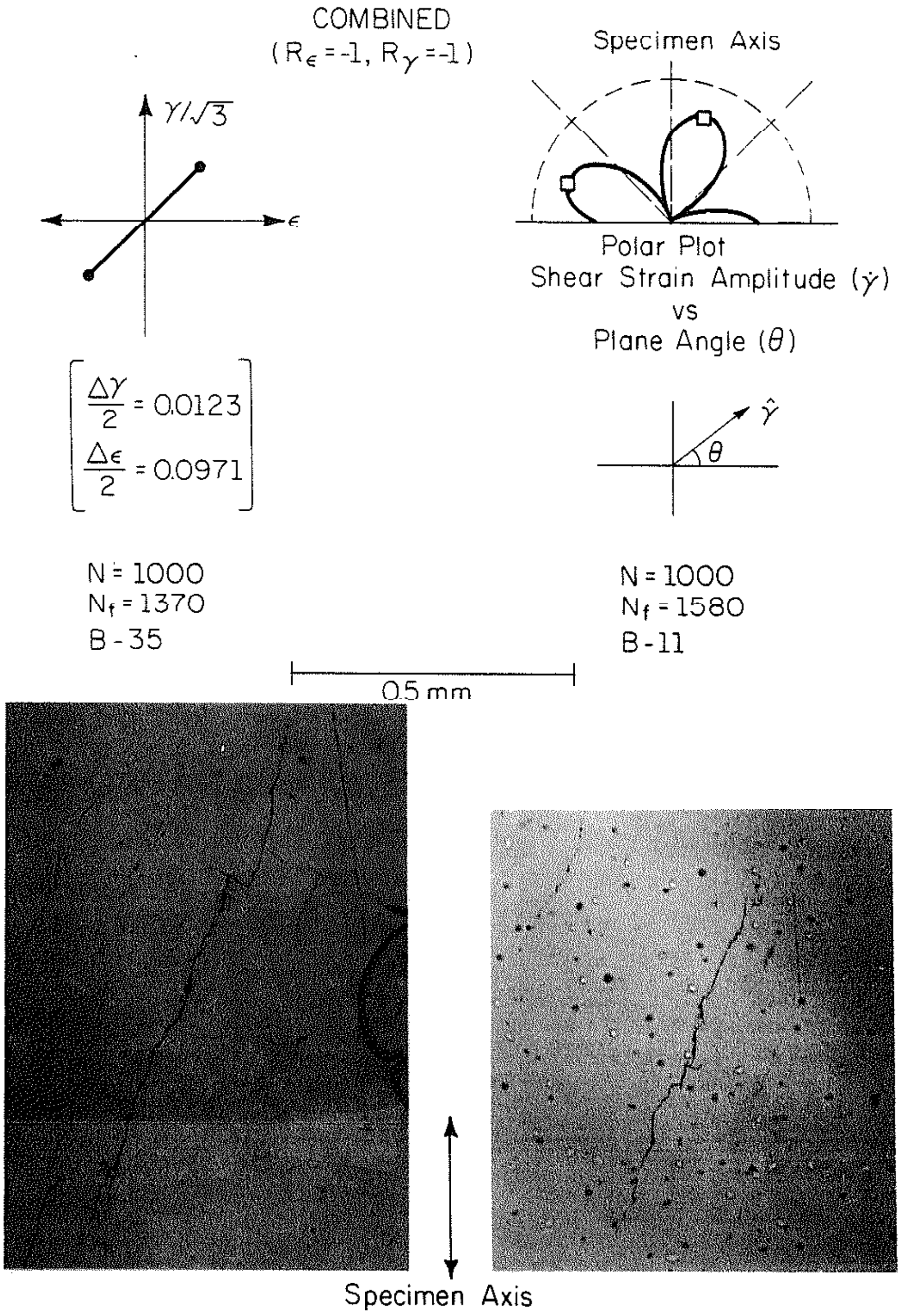

Figure C.6 Strain Path C, $\bar{\epsilon}$ = 0.010

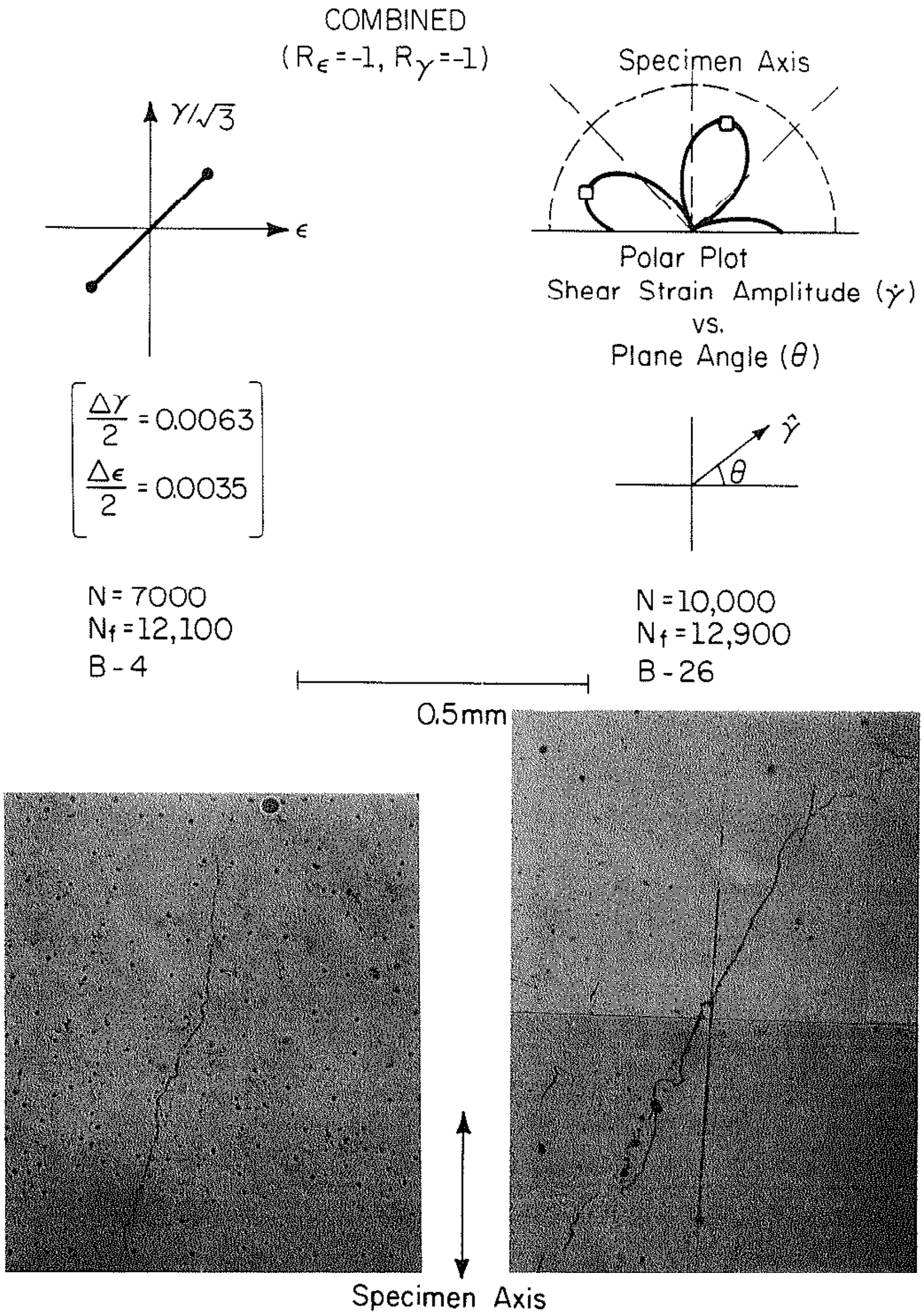

Figure C.7 Strain Path C, $\overline{\epsilon}$ = 0.005

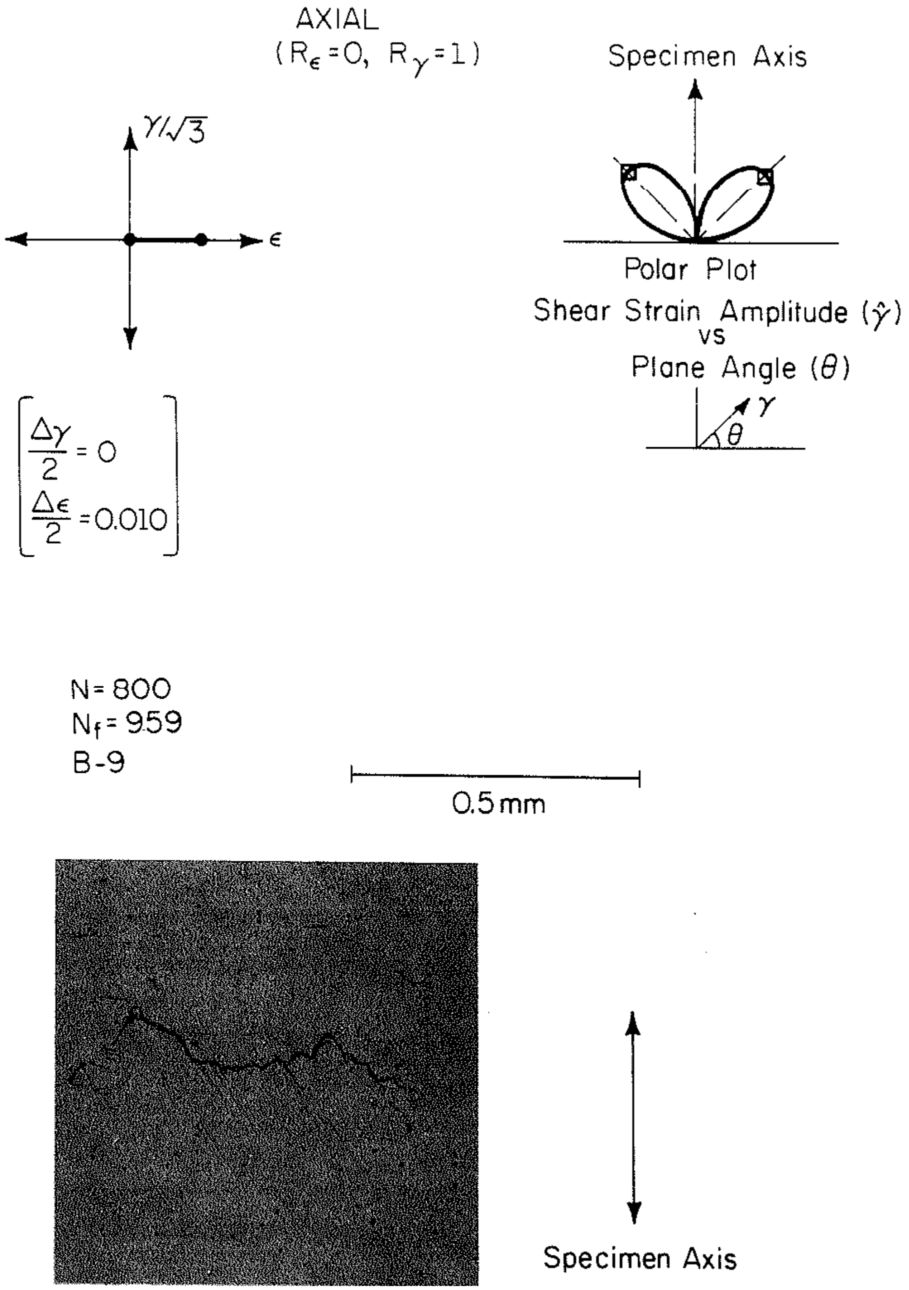

Figure C.8 Strain Path D, $\bar{\varepsilon}$ = 0.010

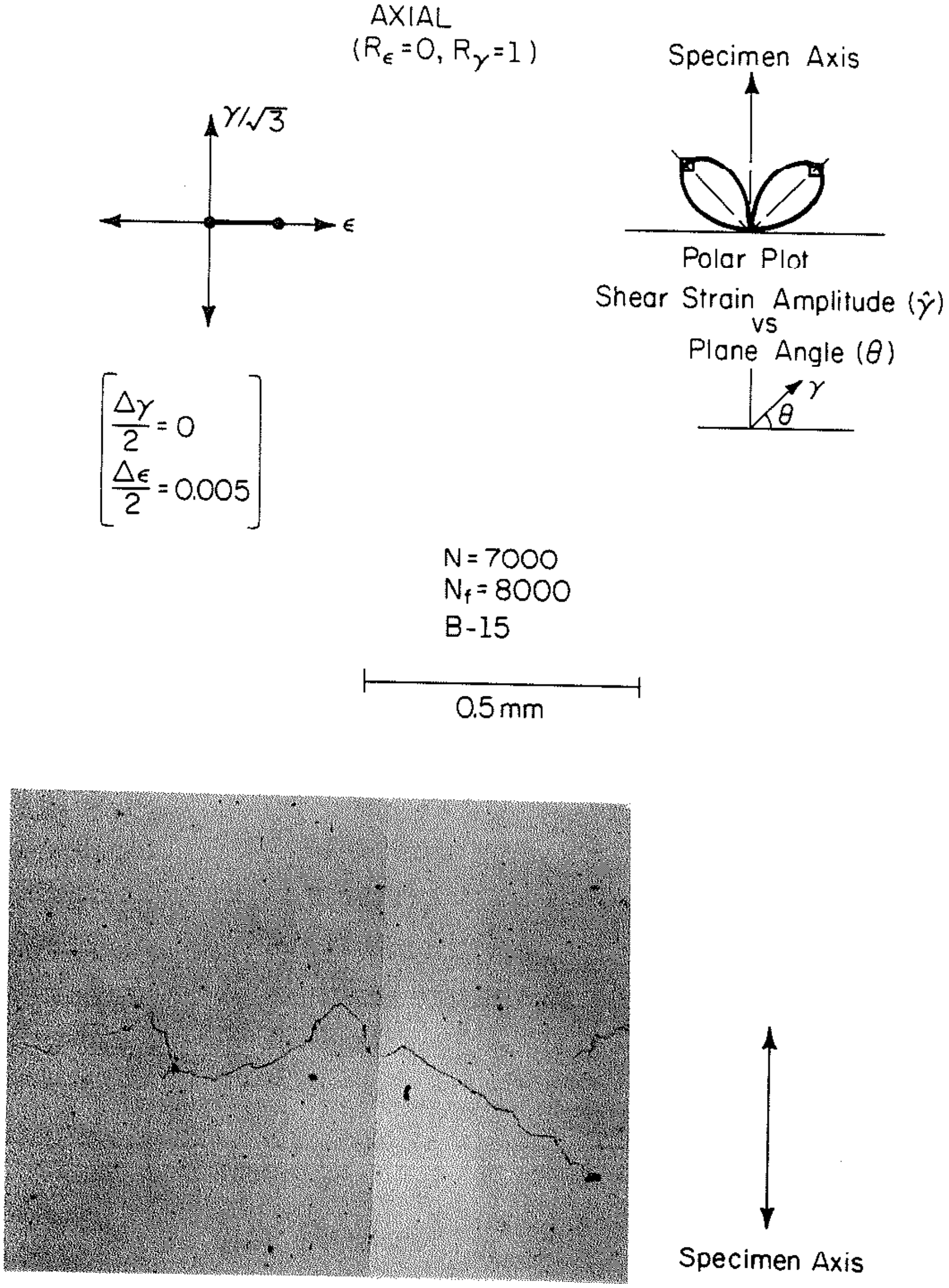

Figure C.9 Strain Path D, $\bar{\varepsilon}$ = 0.005

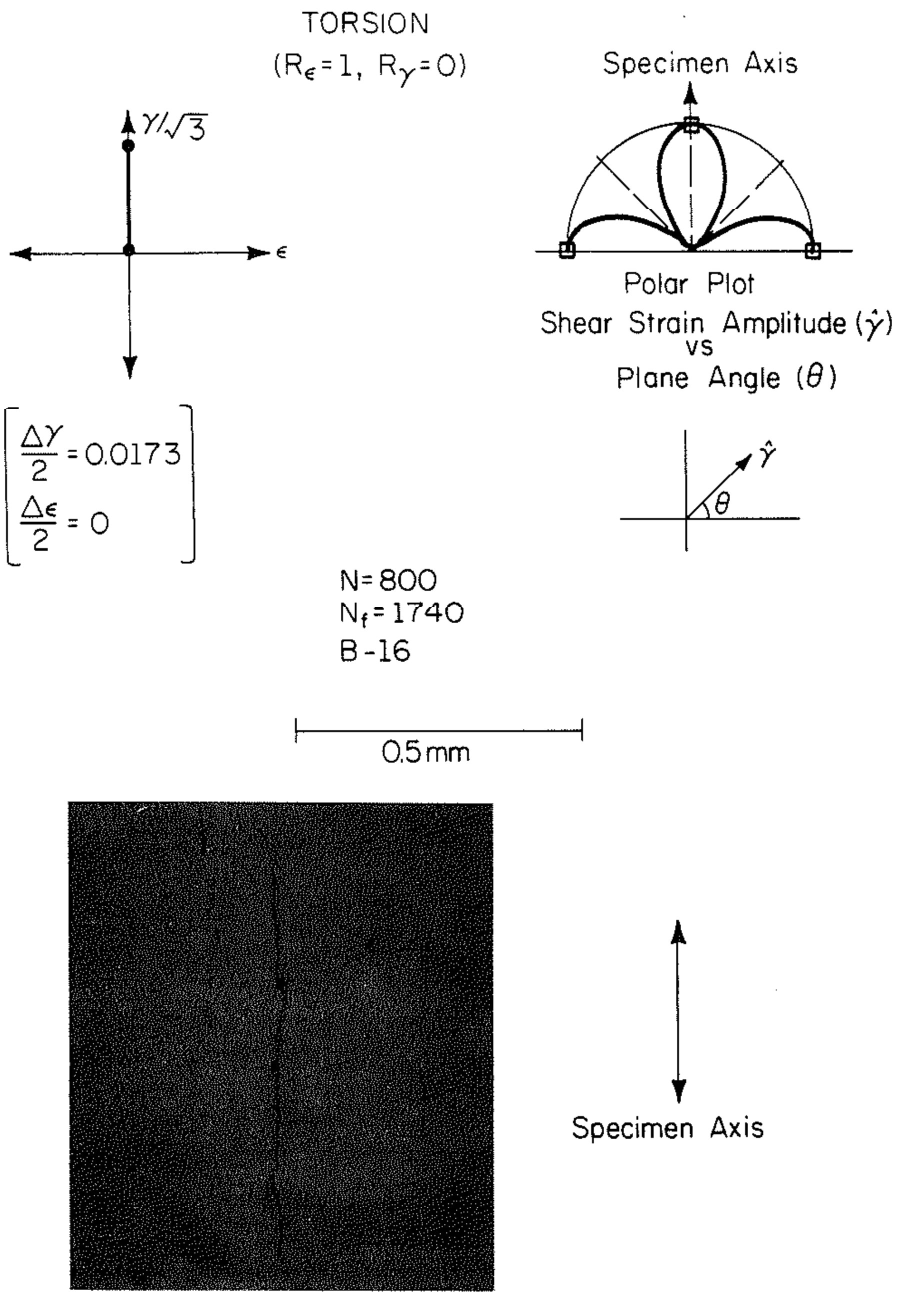

Figure C.10 Strain Path E, $\bar{\varepsilon}$ = 0.010

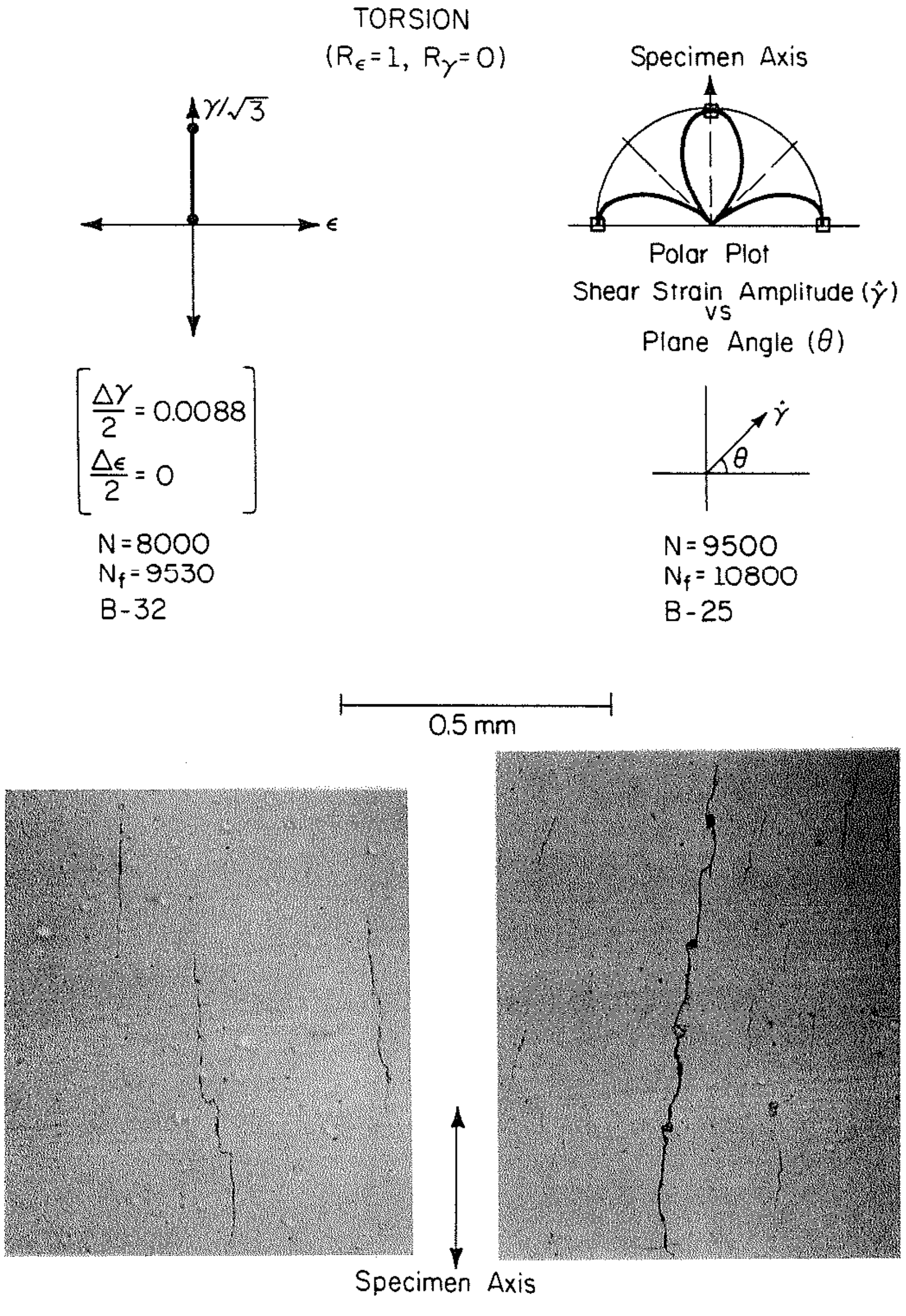

Figure C.11 Strain Path E, $\bar{\varepsilon}$ = 0.005

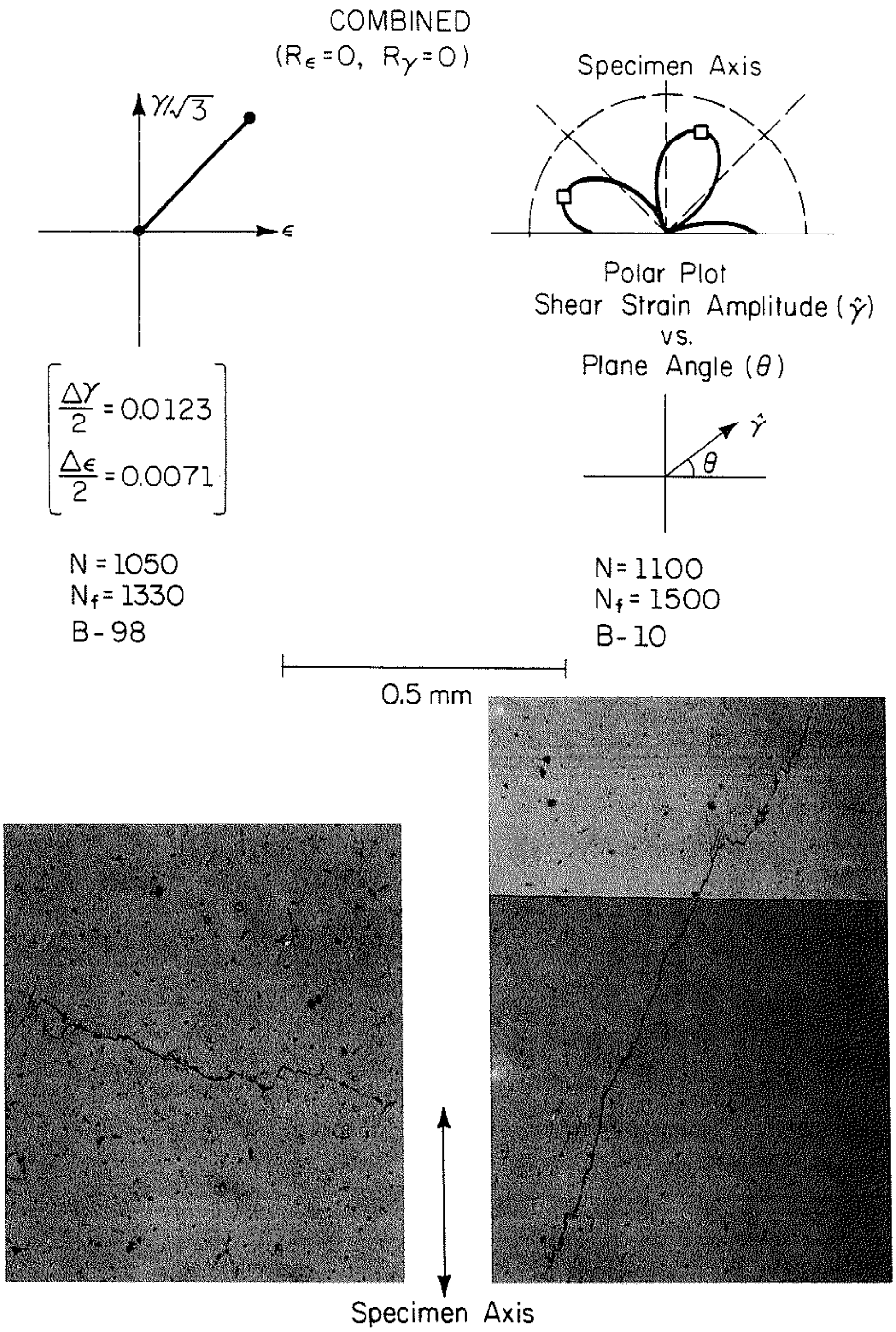

Figure C.12 Strain Path F, $\bar{\varepsilon}$ = 0.010

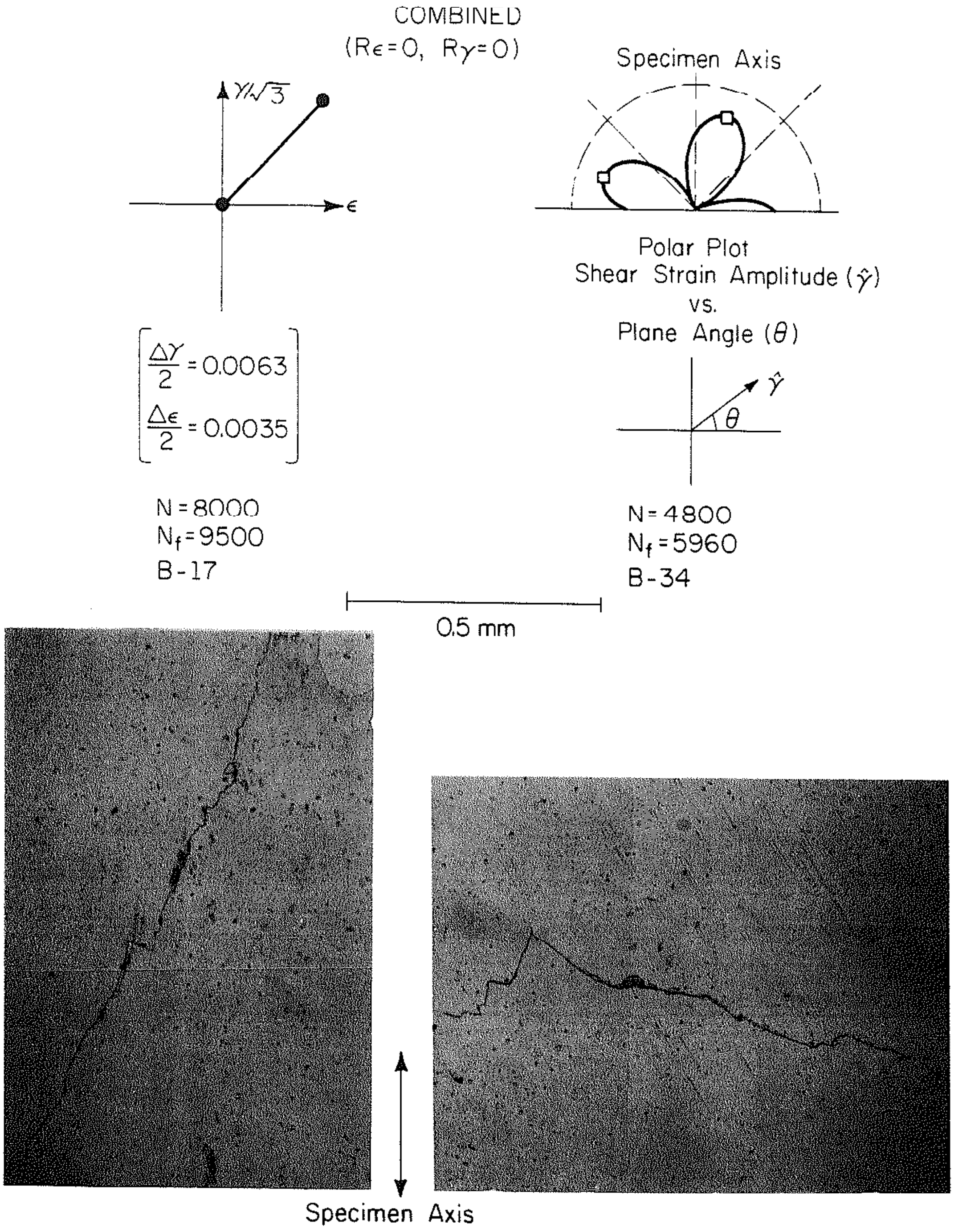

Figure C.13 Strain Path F, $\overline{\varepsilon}$ = 0.005

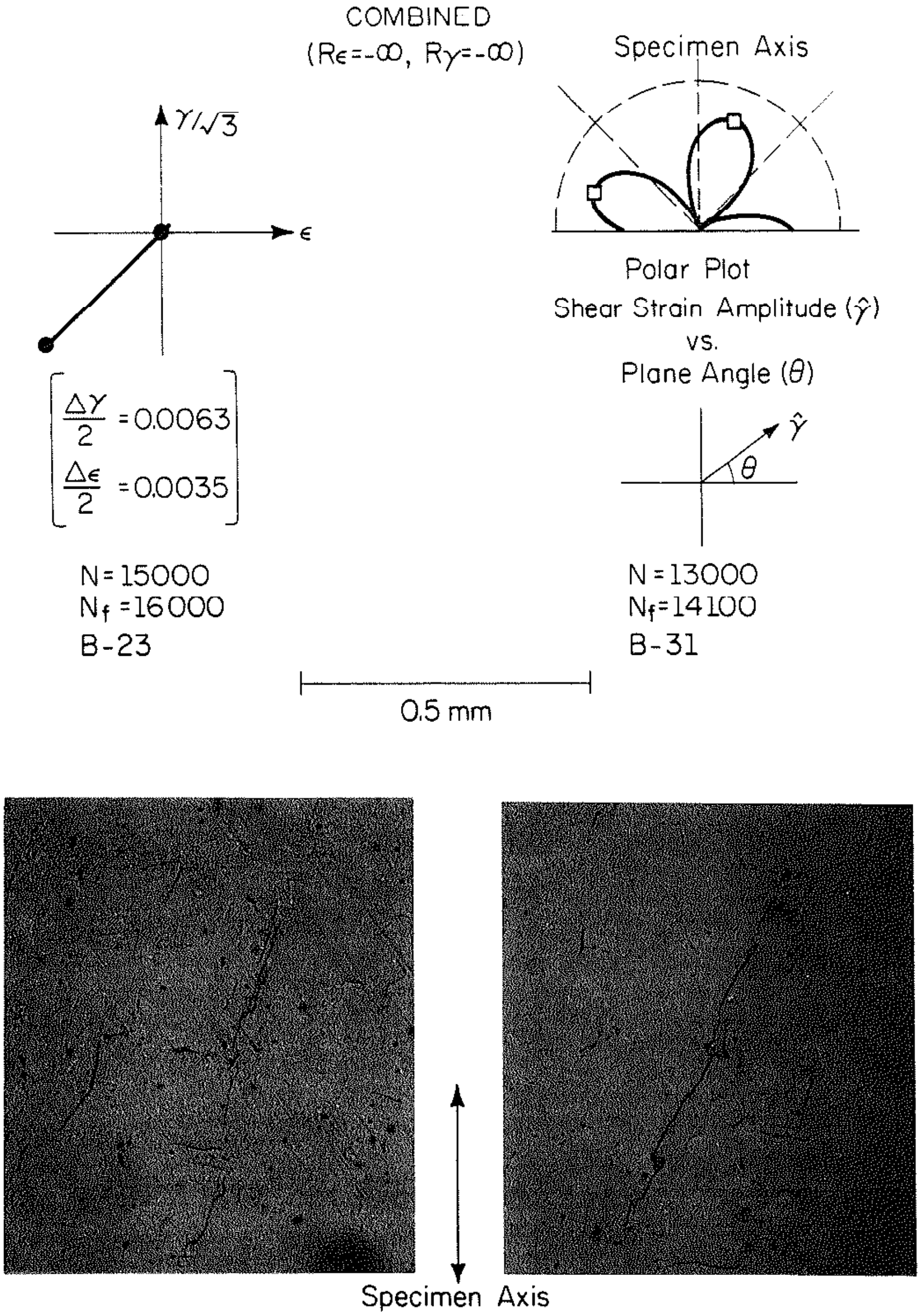

Figure C.14 Strain Path G, $\bar{\epsilon}$ = 0.005

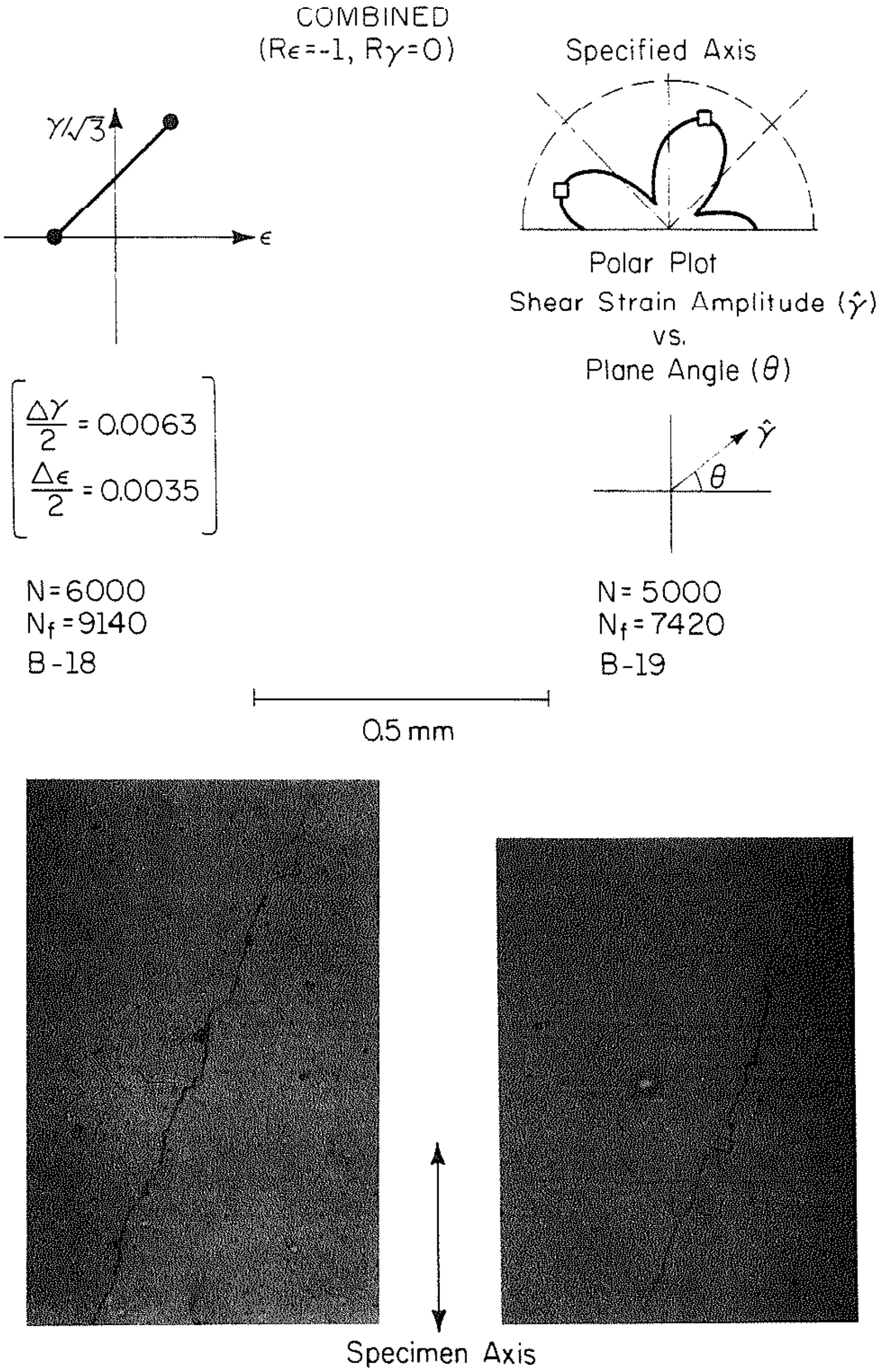

Figure C.15 Strain Path H, $\bar{\epsilon}$ = 0.005

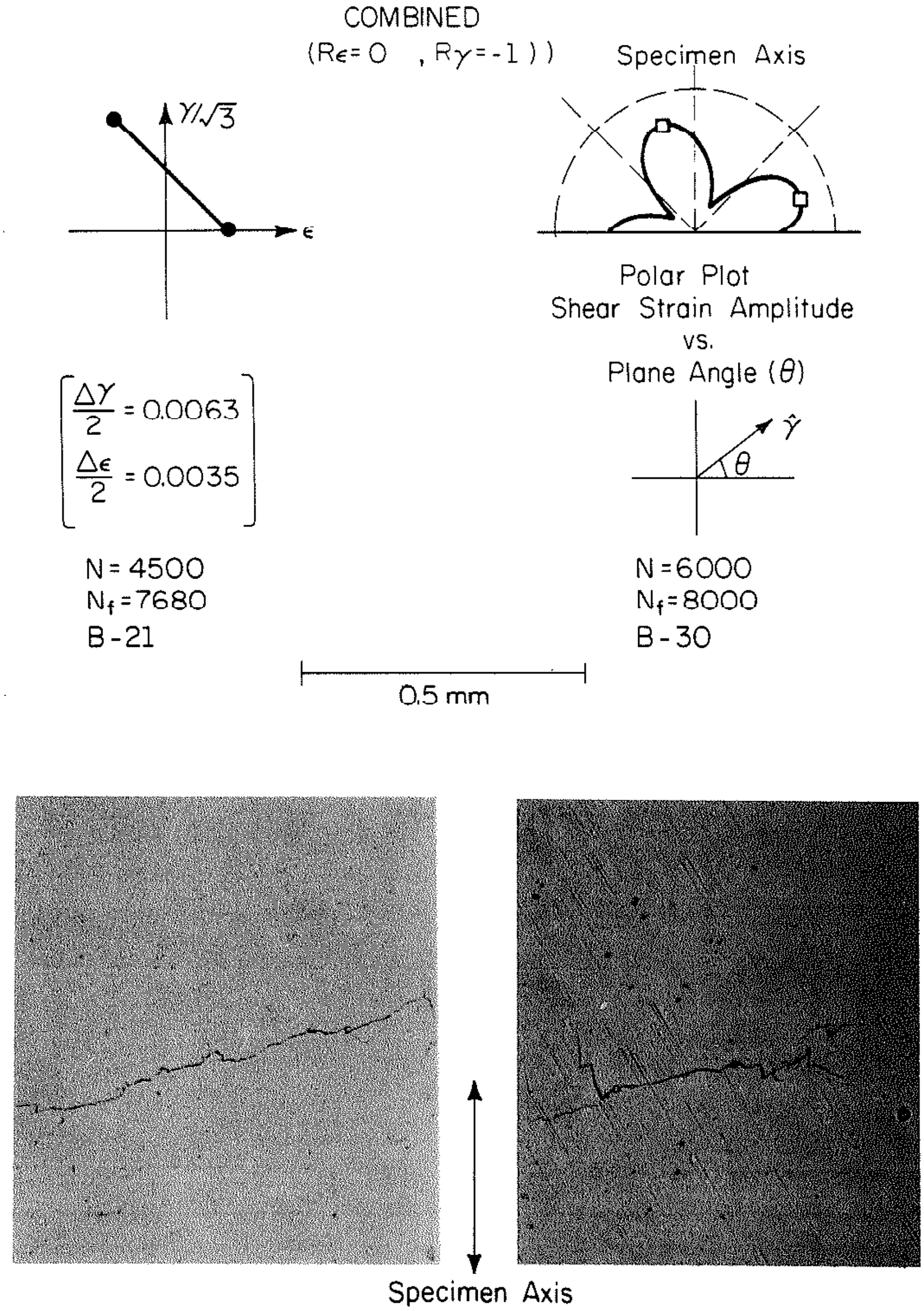

Figure C.16 Strain Path I, $\bar{\varepsilon}$ = 0.005

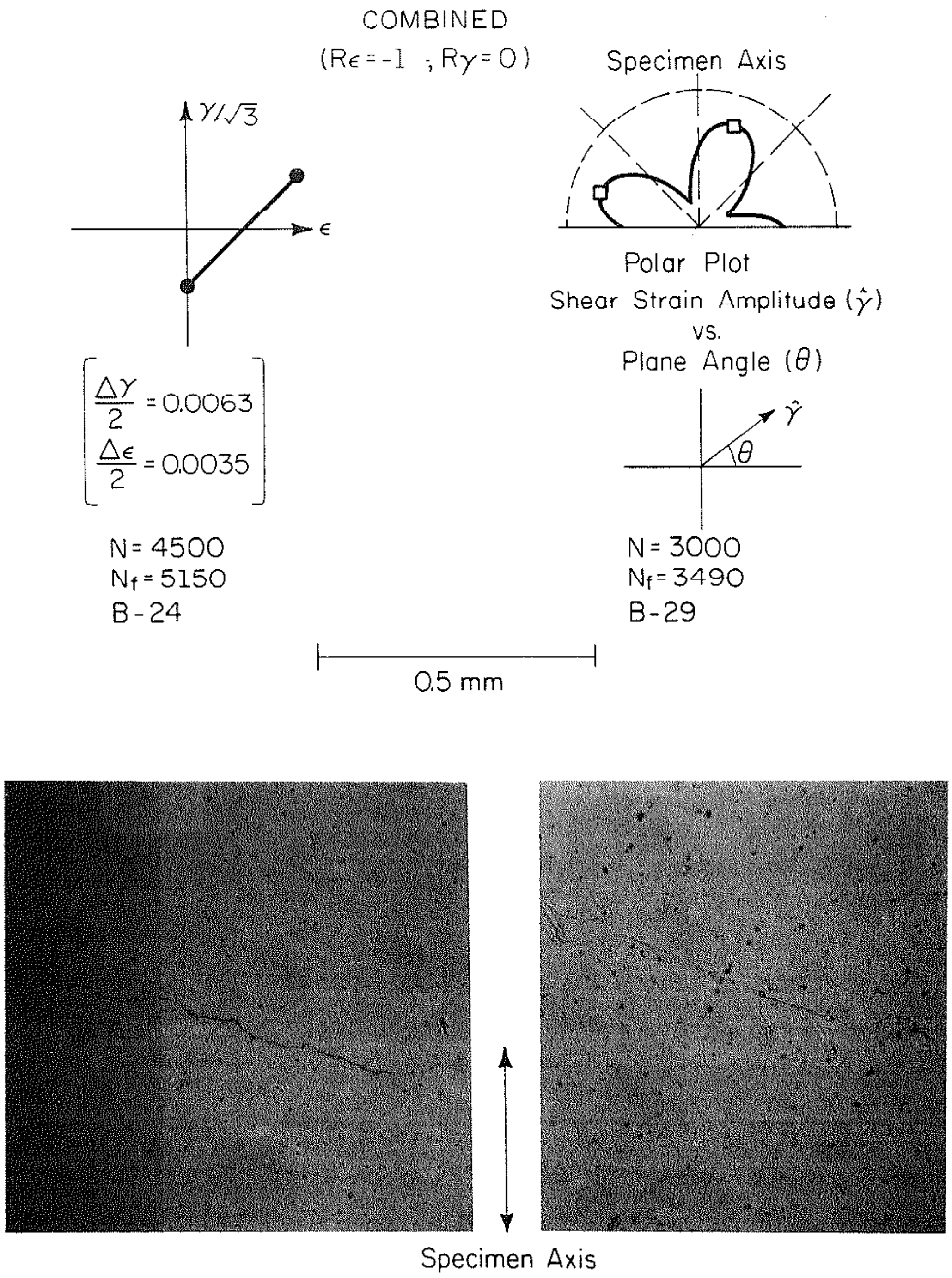

Figure C.17 Strain Path J, $\bar{\varepsilon}$ = 0.005

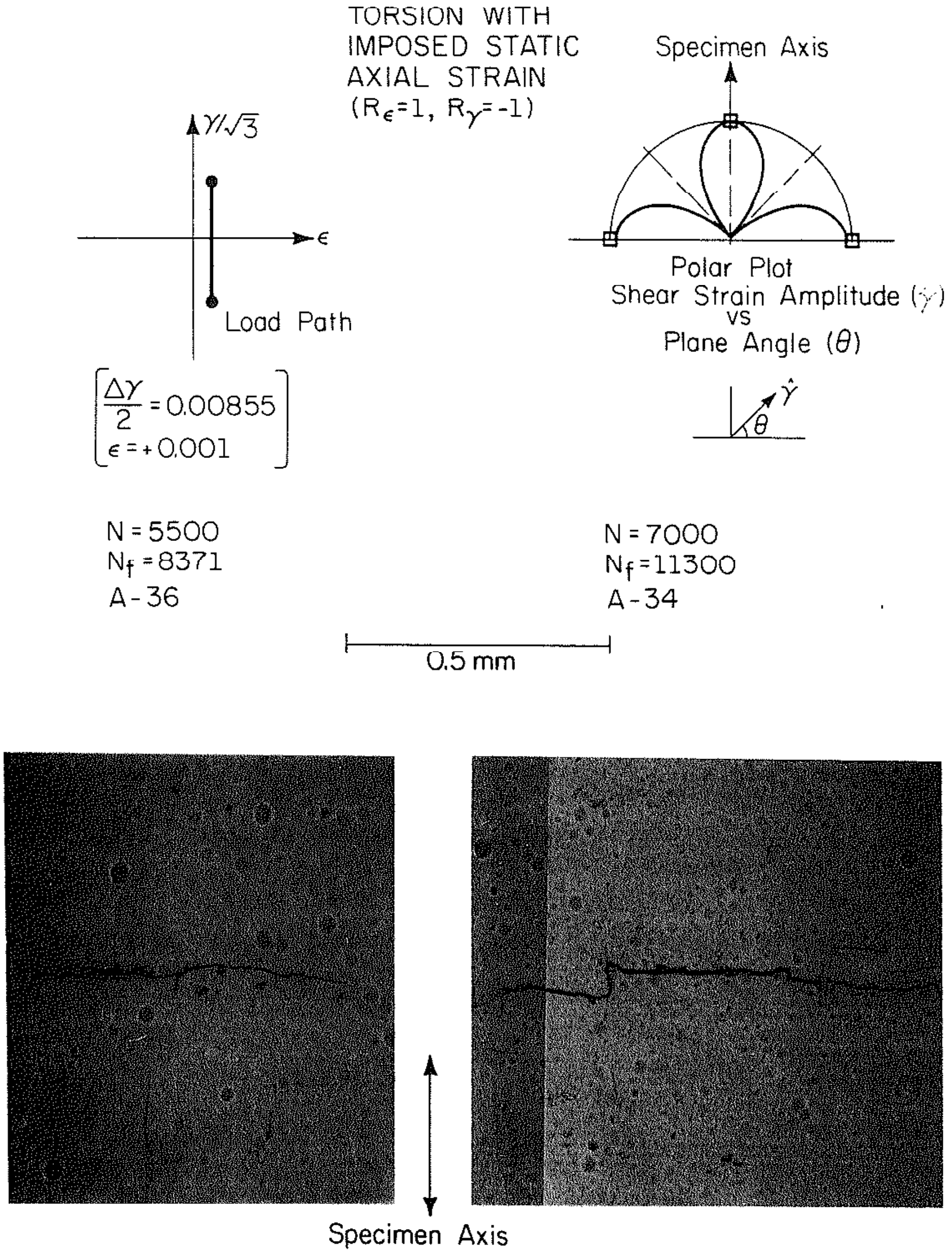

Figure C.18 Strain Path K, $\bar{\epsilon}$ = 0.005

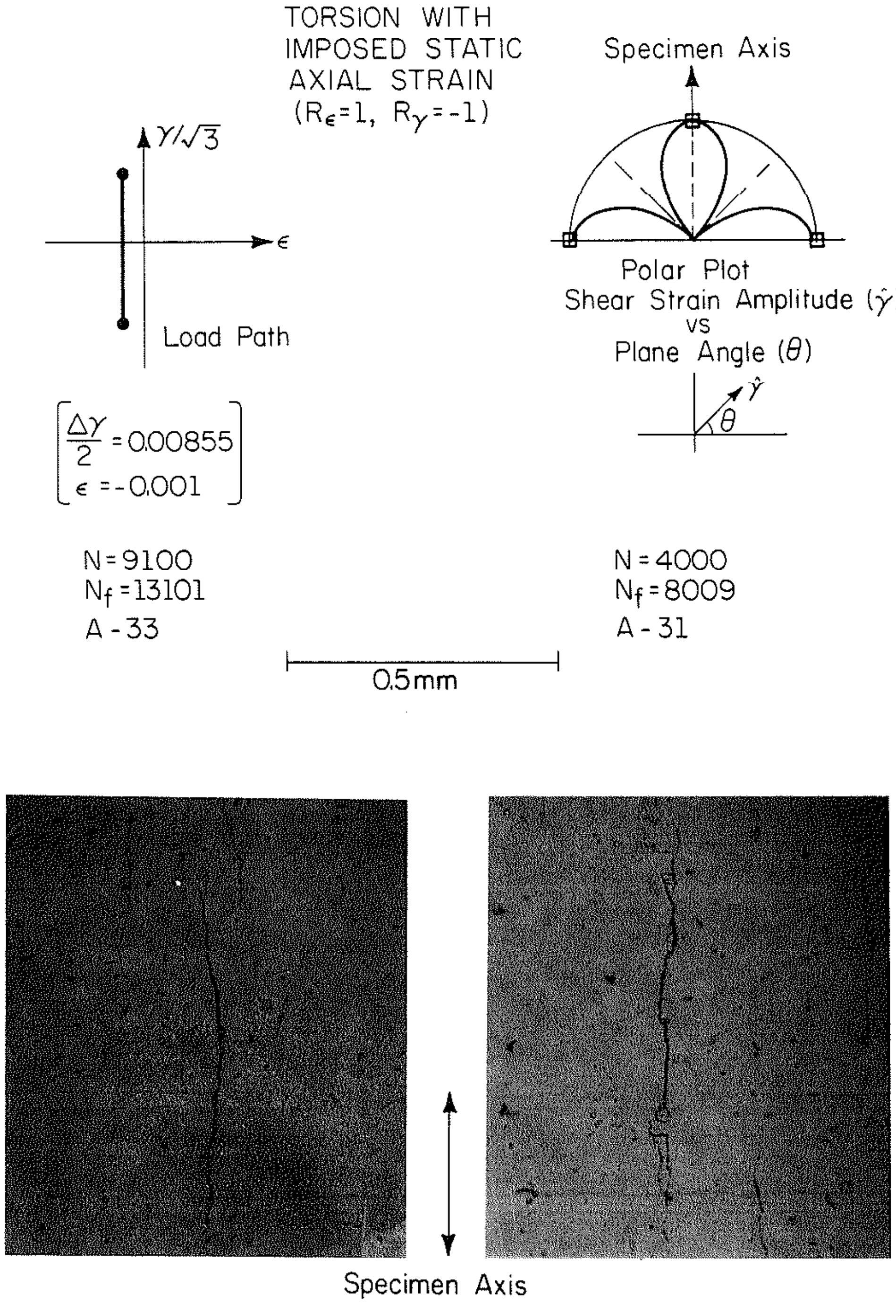

Figure C.19 Strain Path L, $\bar{\epsilon}$ = 0.005

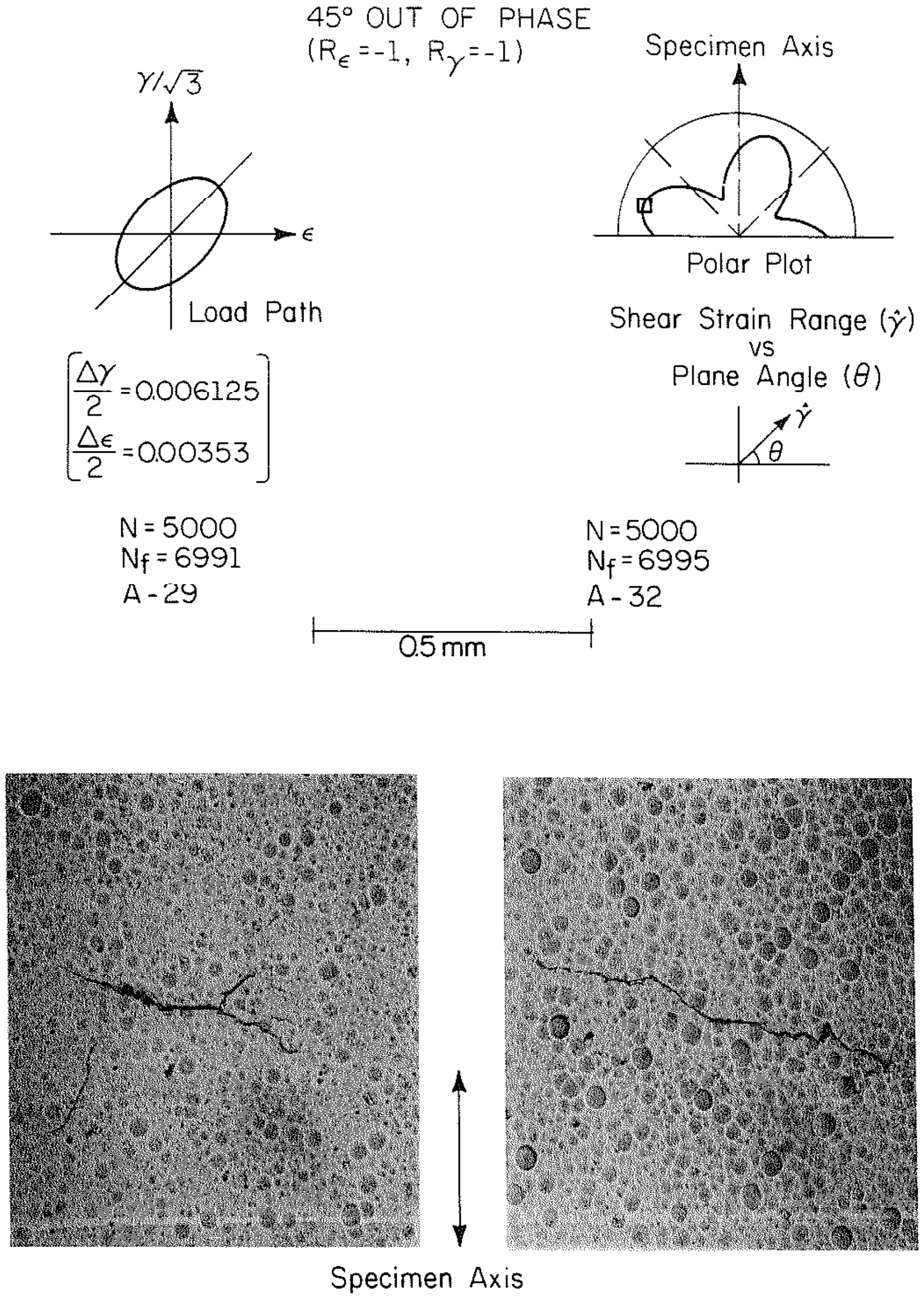

Figure C.20 Strain Path M, $\bar{\varepsilon}$ = 0.005

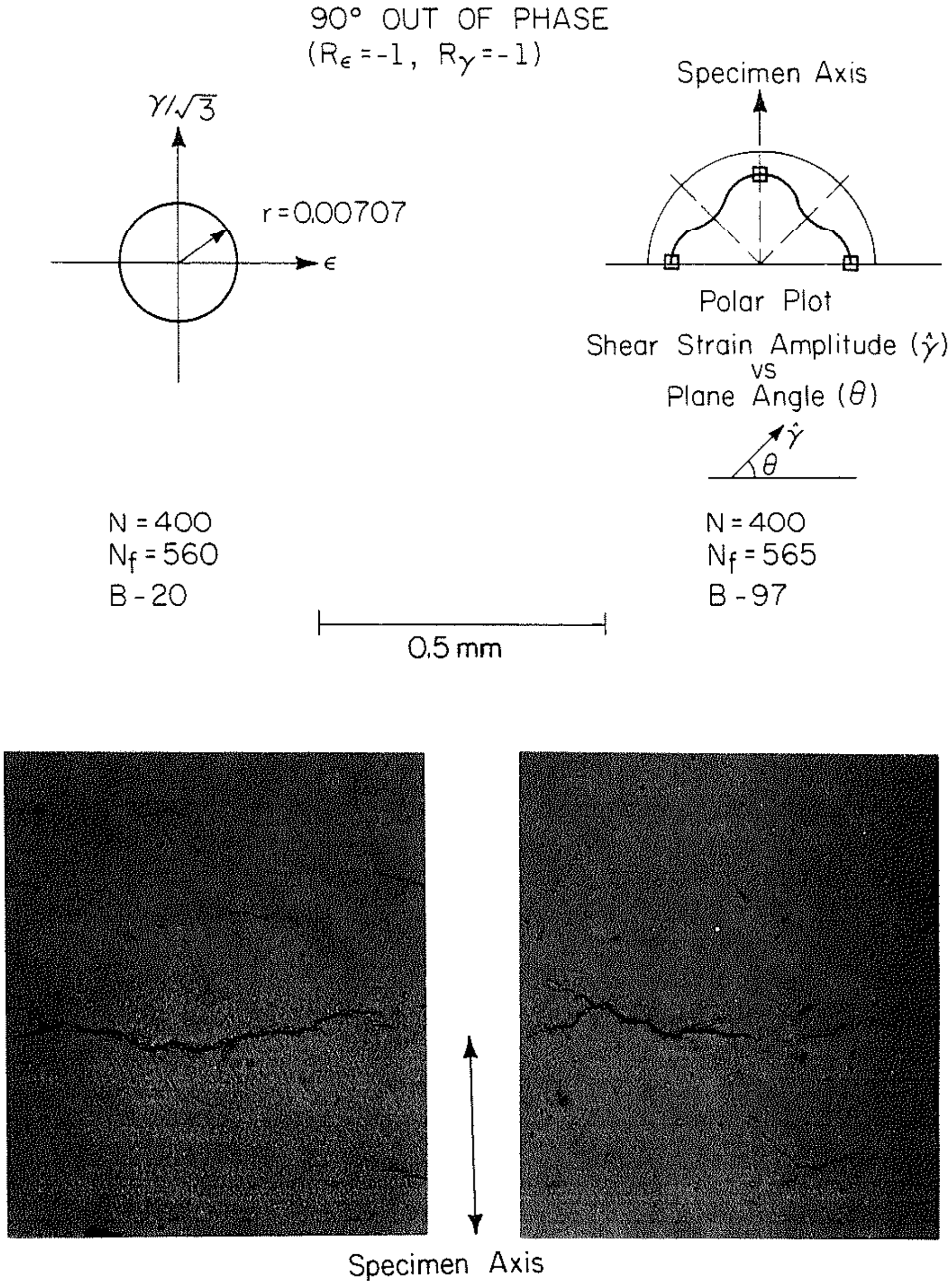

Figure C.21 Strain Path N, $\bar{\epsilon}$ = 0.010

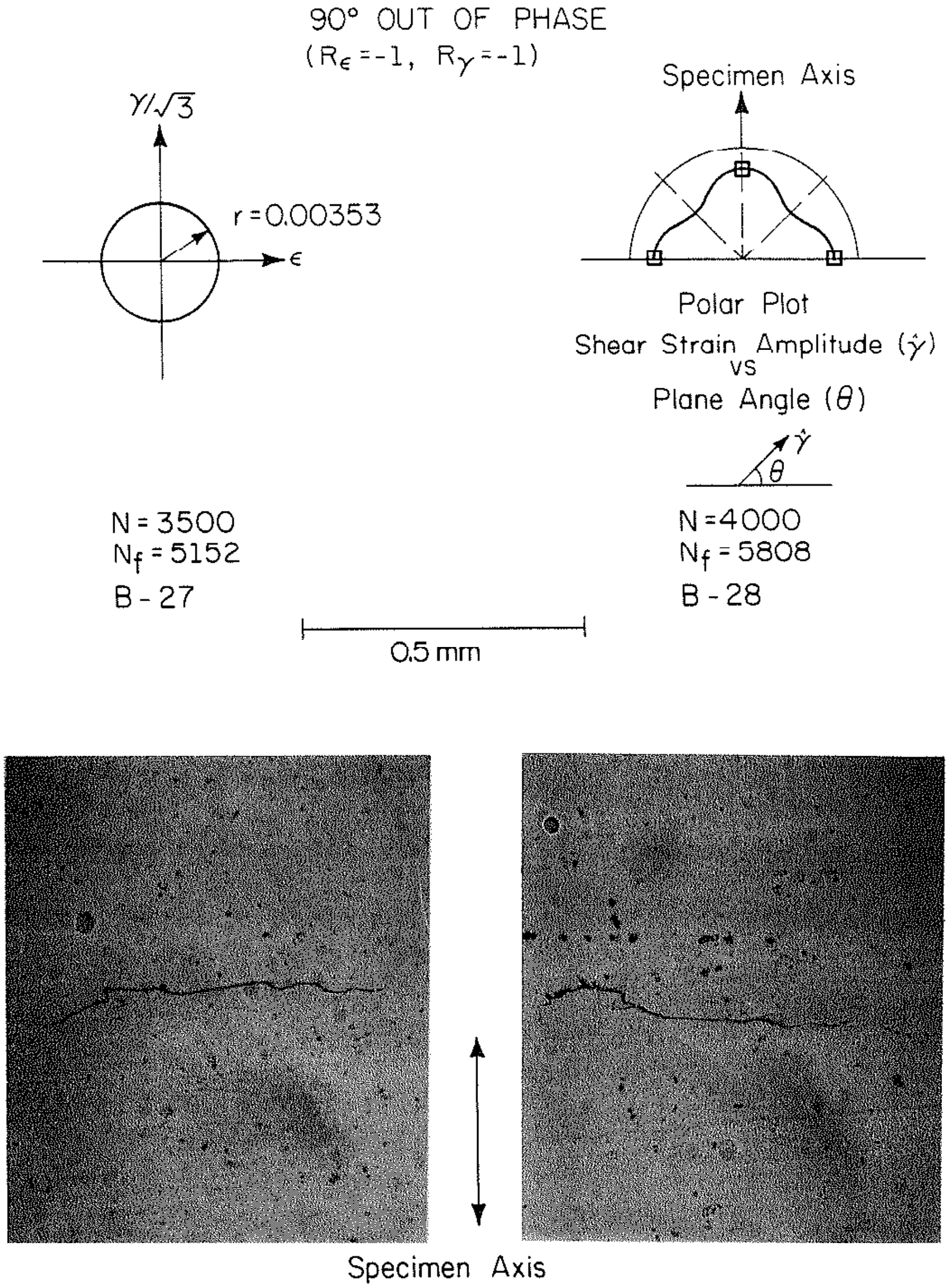

Figure C.22 Strain Path N, $\bar{\varepsilon}$ = 0.005

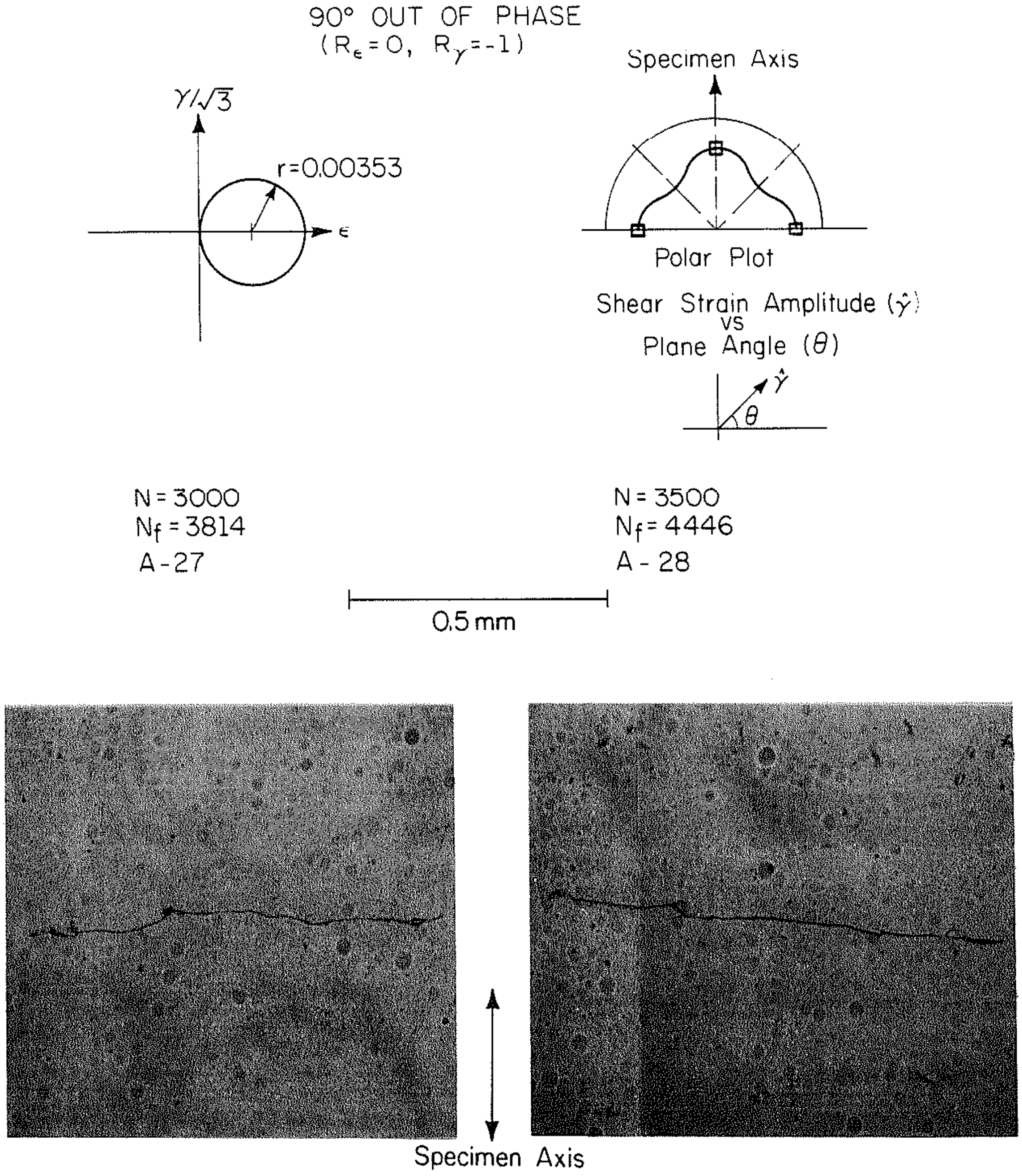

Figure C.23 Strain Path 0, $\overline{\varepsilon}$ = 0.005

APPENDIX D: CRACK GROWTH DATA

LIST OF TABLES

Table D.1 Strain Path A

$R_\varepsilon = -1 \qquad R_\gamma = 1$

$\frac{\Delta\varepsilon}{2} = 0.0100$		$\frac{\Delta\gamma}{2} = 0$		$\frac{\Delta\varepsilon}{2} = 0.0050$		$\frac{\Delta\gamma}{2} = 0$	
B-33		B-14		B-6		B-12	
N (cycles)	a (mm)	N (cycles)	a (mm)	N (cycles)	a (mm)	N (cycles)	a (mm)
100	0.09	100	0.03	2,000	0.01	1,000	0.02
200	0.21	200	0.07	6,000	0.08	2,000	0.06
300	0.32	300	0.13	7,000	0.09	3,000	0.10
400	0.37	400	0.19	8.000	0.10	4,000	0.12
500	0.37	500	0.28	9,000	0.19	5,000	0.13
600	0.46	600	0.39	10,000	0.21	6,000	0.28
700	0.57	700	0.44	11,000	0.43	7,000	0.31
800	0.74	800	0.46	12,000	0.45	8,000	0.64
900	0.80	900	0.52	13,000	0.46	9,000	0.69
1,000	0.80	1,000	1.20	14,000	0.59	11,000	1.00
1,100	1.33	1,100	1.30			12,000	1.12
1,200	1.71	1,200	1.62			12,500	1.55
		1,300	2.48				

Table D.2 Strain Path B

$R_\varepsilon = 1 \qquad R_\gamma = -1$

$\frac{\Delta\varepsilon}{2} = 0$ $\frac{\Delta\gamma}{2} = 0.0176$				$\frac{\Delta\varepsilon}{2} = 0$ $\frac{\Delta\gamma}{2} = 0.0087$				$\frac{\Delta\varepsilon}{2} = 0$ $\frac{\Delta\gamma}{2} = 0.0054$			
B-7		B-13		B-3		B-8		A-35		A-30	
N (cycles)	a (mm)	N (cycles)	a (mm)	N (cycles)	a (mm)	N (cycles)	a (mm)	N (cycles)	a (mm)	N (cycles)	a (mm)
200	0.13	100	0.08			1,000	0.04			400	0.03
300	0.16	200	0.11			2,000	0.07	Not Available		5,000	0.20
400	0.62	300	0.12	Not Available		3,000	0.13			10,000	0.29
500	0.71	400	0.15			4,000	0.21	(Crack growth		15,000	0.30
600	0.88	500	0.38			5,000	0.23	is out of		20,000	0.34
700	0.90	600	0.68			6,000	0.28	gage section)		25,000	0.38
800	1.21	700	0.88			7,000	0.30			30,000	0.59
900	1.36	800	0.98			8,000	0.36			35,000	0.85
1,000	1.49	900	1.05			9,000	0.73			40,000	2.0
1,100	2.10	1,000	1.42			10,000	0.90				
		1,100	2.05			11,000	1.19				

Table D.3 Strain Path C

$R_\varepsilon = -1$ $R_\gamma = -1$

$\frac{\Delta\varepsilon}{2} = 0.0071$		$\frac{\Delta\gamma}{2} = 0.0123$		$\frac{\Delta\varepsilon}{2} = 0.0035$		$\frac{\Delta\gamma}{2} = 0.0061$	
B-35		B-11		B-26		B-4	
N (cycles)	a (mm)	N (cycles)	a (mm)	N (cycles)	a (mm)	N (cycles)	a (mm)
200	0.06	100	0.06	1,000	0.10	2,000	0.07
300	0.12	200	0.07	2,000	0.20	3,000	0.22
400	0.16	300	0.12	3,000	0.23	4,000	0.55
500	0.20	400	0.13	4,000	0.34	5,000	0.66
600	0.37	500	0.17	5,000	0.52	6,000	0.85
700	0.40	600	0.30	6,000	0.58	7,000	0.92
800	0.47	700	0.33	7,000	0.62	9,000	1.19
900	0.87	800	0.50	8,000	0.74	10,000	1.59
1,000	1.04	900	0.66	9,000	0.81	10,500	1.91
1,100	1.42	1,000	0.70	10,000	1.18		
1,200	1.87	1,100	1.00	11,000	1.99		
		1,200	1.85				

Table D.4 Strain Path D

$R_\epsilon = 0 \quad R_\gamma = 1$

$\frac{\Delta\epsilon}{2} = 0.0100$		$\frac{\Delta\gamma}{2} = 0$		$\frac{\Delta\epsilon}{2} = 0.0050$		$\frac{\Delta\gamma}{2} = 0$	
B-5		B-9		B-36		B-15	
N (cycles)	a (mm)	N (cycles)	a (mm)	N (cycles)	a (mm)	N (cycles)	a (mm)
120	0.07	100	0.04	200	0.03	500	0.04
160	0.09	200	0.12	400	0.05	1,000	0.04
200	0.09	300	0.16	800	0.06	1,500	0.06
240	0.18	400	0.21	1,200	0.06	2,000	0.09
280	0.20	500	0.32	2,000	0.07	2,500	0.11
320	0.20	600	0.38	2,400	0.18	3,000	0.11
360	0.20	700	0.45	3,200	0.20	3,500	0.13
480	0.27	800	0.55	3,600	0.28	4,000	0.23
560	0.43	900	1.22	4,000	0.33	4,500	0.25
650	0.62	950	1.71	6,000	0.52	5,000	0.29
750	0.98			7,000	0.71	5,500	0.61
850	1.43					6,000	0.70
						6,500	0.98
						7,000	1.52
						7,500	1.59

Table D.5 Strain Path E

$R_\varepsilon = 1 \qquad R_\gamma = 0$

$\frac{\Delta\varepsilon}{2} = 0$ $\frac{\Delta\gamma}{2} = 0.0173$				$\frac{\Delta\varepsilon}{2} = 0$ $\frac{\Delta\gamma}{2} = 0.0087$			
B-99		B-16		B-32		B-25	
N (cycles)	a (mm)	N (cycles)	a (mm)	N (cycles)	a (mm)	N (cycles)	a (mm)
50	0.10	100	0.09	1,000	0.06	2,000	0.20
100	0.11	200	0.11	1,500	0.07	3,000	0.25
200	0.13	300	0.18	2,000	0.16	4,000	0.27
250	0.13	400	0.24	3,000	0.24	5,000	0.46
350	0.15	500	0.43	4,000	0.36	6,000	0.46
500	0.24	600	0.51	5,000	0.52	7,000	0.47
600	0.26	700	0.61	6,000	0.67	8,000	1.11
700	0.46	800	0.71	7,000	0.73	9,000	1.67
800	0.49	900	1.50	8,500	1.51		
900	0.84	1,000	2.74	9,000	1.86		
1,000	1.05	1,100	3.06	9,500	2.00		
1,100	1.17	1,200	4.13				
1,200	1.26	1,400	5.66				
1,300	1.40						

Table D.5 Strain Path F

$R_{\varepsilon} = 0 \quad R_{\gamma} = 0$

$\frac{\Delta\varepsilon}{2} = 0.0071$		$\frac{\Delta\varepsilon}{2} = 0.0123$		$\frac{\Delta\varepsilon}{2} = 0.0035$		$\frac{\Delta\varepsilon}{2} = 0.0063$	
B-98		B-10		B-34		B-17	
N (cycles)	a (mm)	N (cycles)	a (mm)	N (cycles)	a (mm)	N (cycles)	a (mm)
125	0.05	100	0.14	1,600	0.05	4,000	0.09
225	0.10	200	0.22	2,200	0.12	4,500	0.16
300	0.22	400	0.38	2,400	0.16	5,000	0.20
375	0.25	500	0.46	3,200	0.43	5,500	0.31
450	0.27	600	0.49	4,000	0.70	6,000	0.62
525	0.40	800	0.67	4,800	1.10	6,500	0.86
600	0.44	900	0.77	5,600	2.20	7,000	0.94
675	0.50	1,000	1.0	5,941	7.90	7,500	1.54
750	0.57	1,100	1.18			8,000	1.56
825	0.71	1,200	1.45			8,500	1.95
875	0.88	1,300	2.00			9,000	3.20
1,050	0.92	1,400	2.30				
1,200	1.24						
1,260	2.21						

Table D.7 STRAIN PATH G

$R_\varepsilon = -\infty$ $R_\gamma = -\infty$

$\frac{\Delta\varepsilon}{2} = 0.0035$ $\frac{\Delta\varepsilon}{2} = 0.0063$

B-31		B-23	
N (cycles)	a (mm)	N (cycles)	a (mm)
2,000	----	1,000	0.03
3,000	0.12	2,000	0.03
4,000	0.16	3,000	0.12
5,000	0.23	4,000	0.24
6,000	0.30	6,000	0.57
8,000	0.47	8,000	1.11
10,000	0.70	10,000	1.21
12,000	1.09	12,000	1.32
13,000	1.42	13,000	1.73
14,000	6.56	15,000	3.63
		16,000	8.48

Table D.8 STRAIN PATH H

$R_\varepsilon = -1$ $R_\gamma = 0$

$\frac{\Delta\varepsilon}{2} = 0.0035$ $\frac{\Delta\gamma}{2} = 0.0063$

B-18		B-19	
N (cycles)	a (mm)	N (cycles)	a (mm)
1,000	0.03	2,000	0.07
2,000	0.19	2,500	0.16
4,000	0.27	3,000	0.31
6,000	1.01	3,500	0.55
8,000	0.18	4,000	0.86
		4,500	1.17
		5,000	1.25
		5,500	1.41
		6,000	2.03
		6,500	2.11
		7,000	4.22

Table D.9 PATH I

$R_\varepsilon = -1$ $R_\gamma = 0$

$\frac{\Delta\varepsilon}{2} = 0.0035$ $\frac{\Delta\gamma}{2} = 0.0063$

B-21		B-30	
N (cycles)	a (mm)	N (cycles)	a (mm)
2,000	0.11	1,000	----
2,500	0.23	2,000	0.04
3,000	0.31	3,000	0.07
3,500	0.47	4,000	0.14
4,000	0.94	5,000	0.44
4,500	0.95	6,000	0.77
5,000	1.05	7,000	0.96
5,500	1.41	8,000	7.25
6,000	2.05		
6,500	2.42		
7,000	3.28		
7,500	5.08		

Table D.10 STRAIN PATH J

$R_\varepsilon = 0$ $R_\gamma = -1$

$\frac{\Delta\varepsilon}{2} = 0.0035$ $\frac{\Delta\gamma}{2} = 0.0063$

B-24		B-29	
N (cycles)	a (mm)	N (cycles)	a (mm)
2,500	0.08	1,000	0.18
2,750	0.15	2,000	0.34
3,000	0.23	3,000	0.80
3,250	0.31	4,000	6.02
3,500	0.39		
3,750	0.43		
4,000	0.51		
4,500	0.86		
5,000	2.19		

Table D.11 STRAIN PATH K

$R_\varepsilon = 1$ $R_\gamma = -1$

$\frac{\Delta\varepsilon}{2} = 0$ $\frac{\Delta\gamma}{2} = 0.0086$

A-36		A-34	
N (cycles)	a (mm)	N (cycles)	a (mm)
500	0.06	700	0.15
1,000	0.12	1,400	0.19
1,500	0.16	2,100	0.26
2,000	0.37	3,500	0.34
2,500	0.39	4,200	0.34
3,000	0.42	4,900	0.34
3,500	0.43	5,600	0.55
4,000	0.48	6,300	0.56
5,000	0.55	7,000	0.60
6,000	0.78	7,700	1.20
7,000	1.54	8,400	2.62
8,000	2.54	9,100	2.85

Table D.12 STRAIN PATH L

$R_\varepsilon = 1$ $R_\gamma = -1$

$\frac{\Delta\varepsilon}{2} = 0$ $\frac{\Delta\gamma}{2} = 0.0086$

A-31		A-33	
N (cycles)	a (mm)	N (cycles)	a (mm)
500	0.04	700	0.12
1,000	0.10	1,400	0.16
1,500	0.26	2,100	0.18
2,000	0.28	2,800	0.20
2,500	0.30	3,500	0.25
3,000	0.47	4,900	0.31
3,500	0.78	6,300	0.39
4,000	1.06	7,000	0.43
5,000	1.80	7,700	0.51
6,000	4.69	8,400	0.60
7,000	7.81	9,100	1.08
		11,000	2.38

Table D.13 STRAIN PATH M

$R_\varepsilon = -1$ $R_\gamma = -1$

$\frac{\Delta\varepsilon}{2} = 0.0035$ $\frac{\Delta\varepsilon}{2} = 0.0062$

A-32		A-29	
N (cycles)	a (mm)	N (cycles)	a (mm)
500	0.09	500	0.06
1,000	0.12	1,000	0.06
1,500	0.12	1,500	0.06
2,000	0.13	2,000	0.09
2,500	0.13	2,500	0.10
3,000	0.23	3,000	0.11
3,500	0.31	3,500	0.16
4,000	0.38	4,000	0.22
4,500	0.51	5,000	0.42
5,000	0.63	5,500	0.56
5,500	0.95	6,000	0.89
6,000	1.45	6,500	1.62

Table D.14 STRAIN PATH N

$R_\varepsilon = -1 \quad R_\gamma = -1$

$\frac{\Delta\varepsilon}{2} = 0.0071$		$\frac{\Delta\varepsilon}{2} = 0.0123$		$\frac{\Delta\varepsilon}{2} = 0.0035$		$\frac{\Delta\varepsilon}{2} = 0.0062$	
B-20		B-97		B-28		B-27	
N (cycles)	a (mm)	N (cycles)	a (mm)	N (cycles)	a (mm)	N (cycles)	a (mm)
150	0.05	100	0.05	1,000	0.14	2,000	0.08
200	0.16	150	0.12	2,000	0.19	2,500	0.22
270	0.34	200	0.15	3,000	0.31	3,000	0.44
300	0.36	270	0.22	4,000	0.76	3,500	0.62
350	0.58	300	0.25	5,000	1.40	4,000	0.92
400	0.69	350	0.33			4,500	1.69
450	1.00	400	0.77			5,000	4.61
500	1.69	450	1.15				
550	4.77	500	1.45				
		550	2.38				

Table D.15 STRAIN PATH 0

$R_\varepsilon = 0 \qquad R_\gamma = -1$

$\frac{\Delta\varepsilon}{2} = 0.0035 \qquad \frac{\Delta\gamma}{2} = 0.0062$

A-28		A-27	
N (cycles)	a (mm)	N (cycles)	a (mm)
500	0.14	1,000	0.13
1,000	0.14	1,500	0.20
2,000	0.28	2,000	0.30
2,500	0.37	2,500	0.42
3,000	0.56	3,000	0.82
3,500	0.92	3,500	2.34
4,020	1.82		

APPENDIX E: CRACK GROWTH COMPARISONS

LIST OF FIGURES

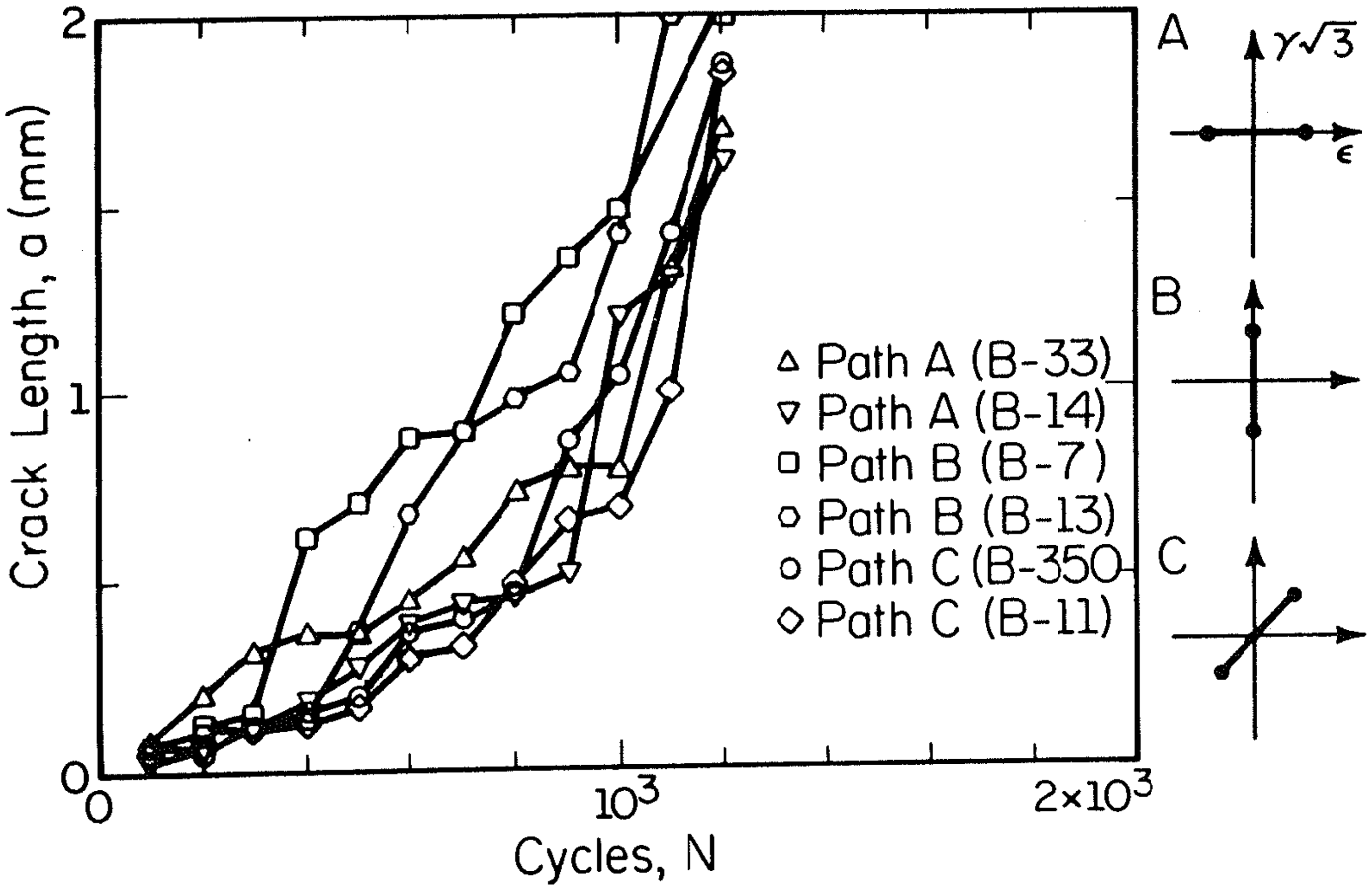

Figure E.1 Strain Paths A, B, and C, $\bar{\varepsilon} = 0.01$

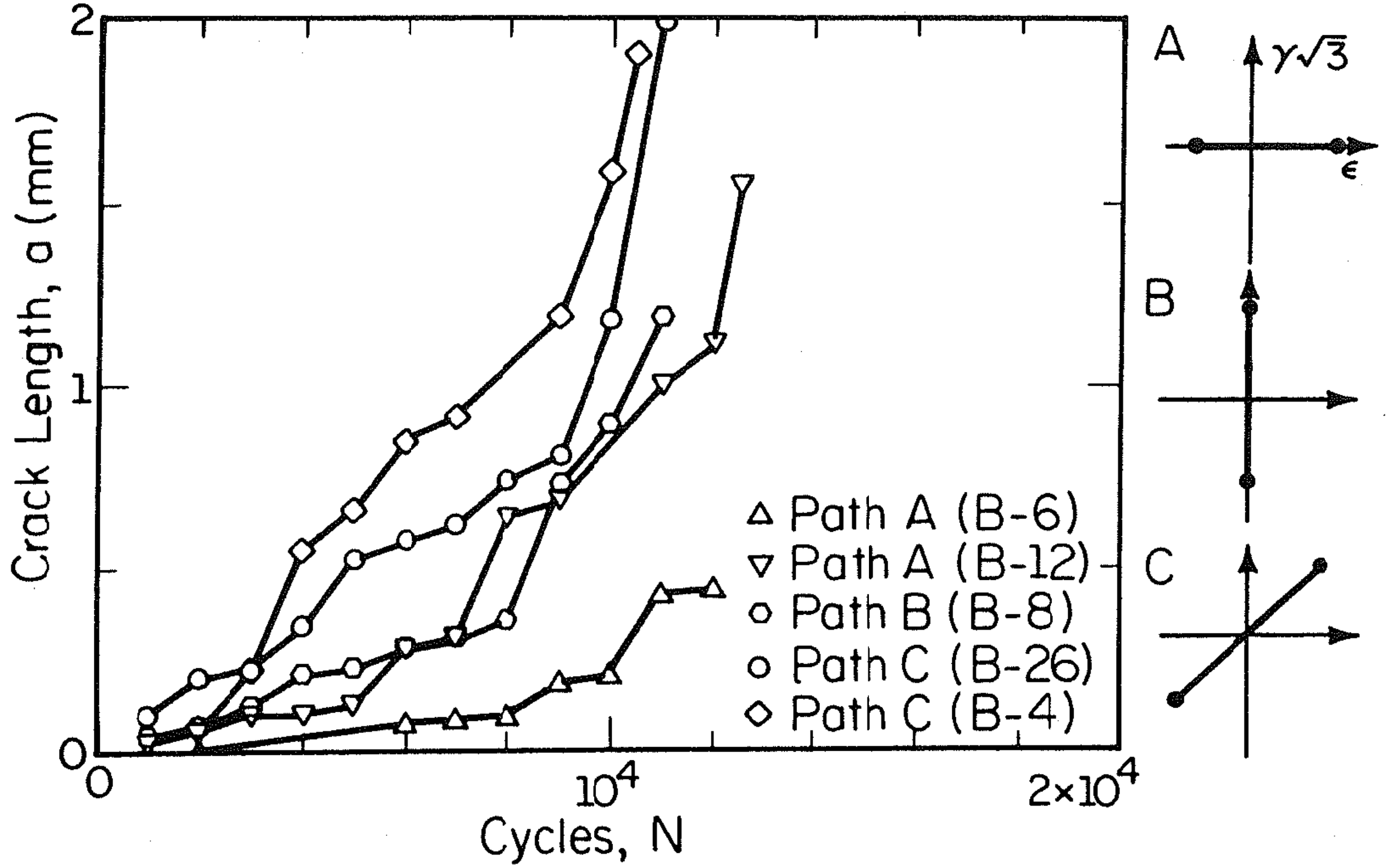

Figure E.2 Strain Paths A, B, and C, $\bar{\epsilon} = 0.005$

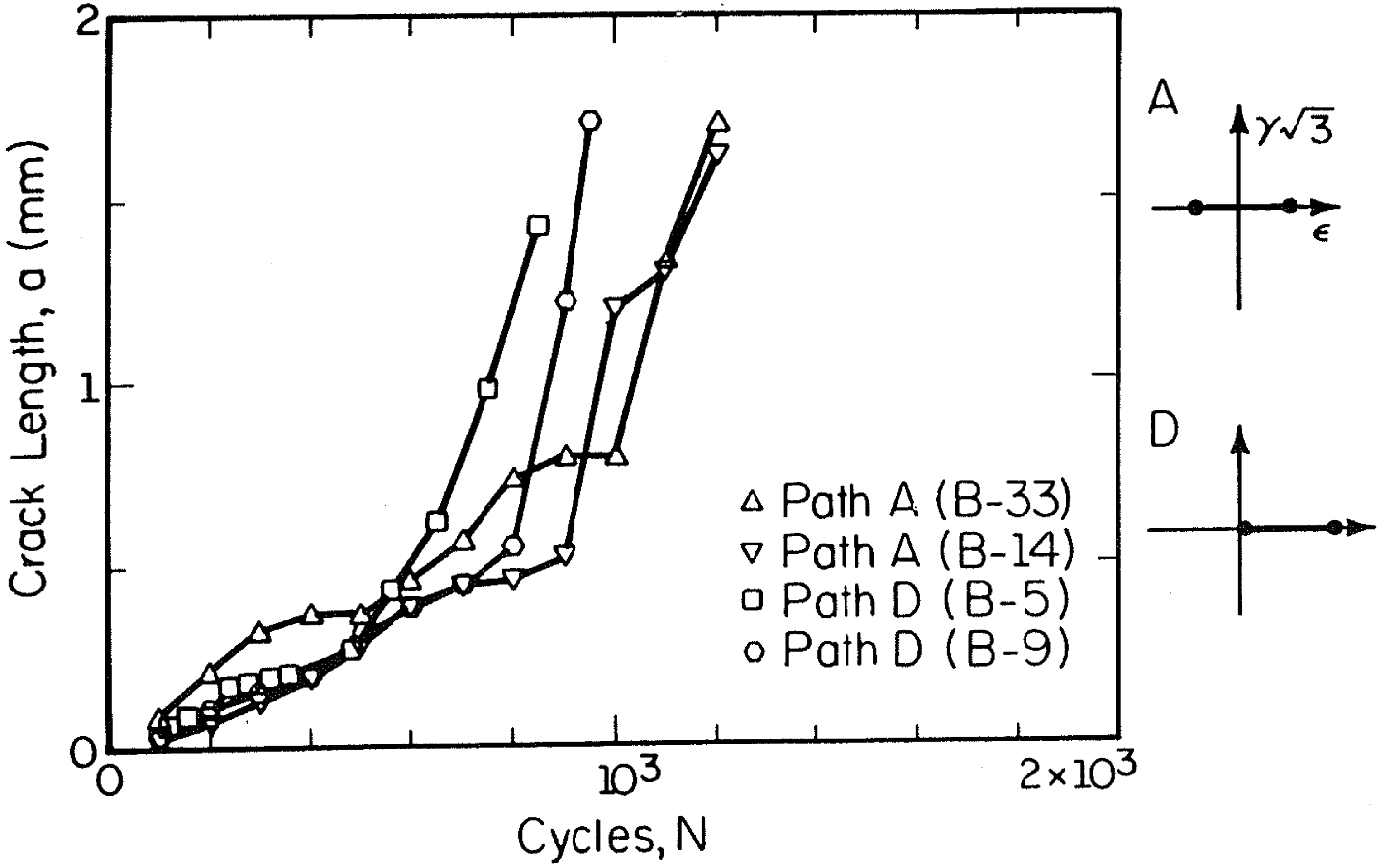

Figure E.3 Strain Paths A and D, $\bar{\epsilon} = 0.010$

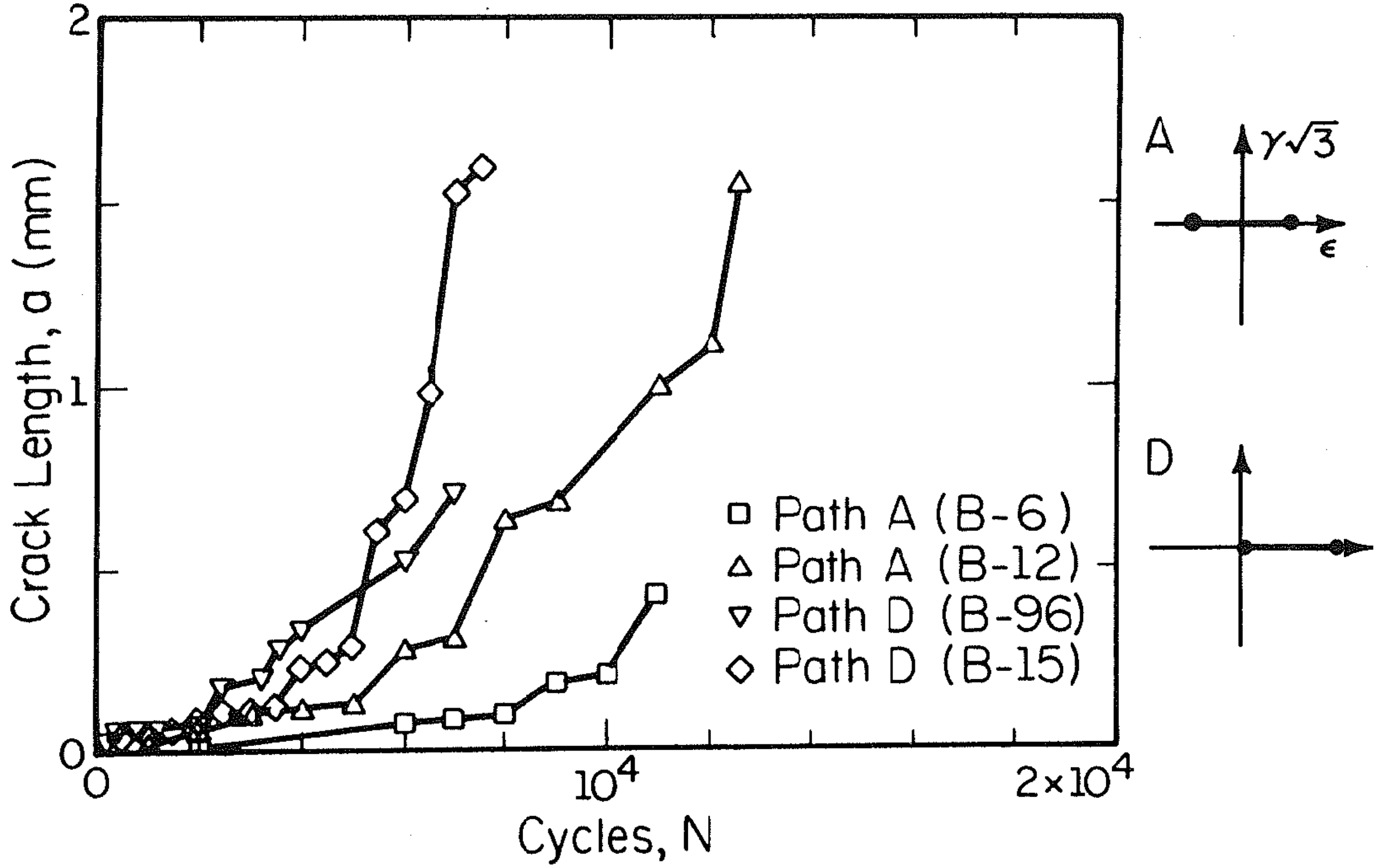

Figure E.4 Strain Paths A and D, $\overline{\varepsilon} = 0.005$

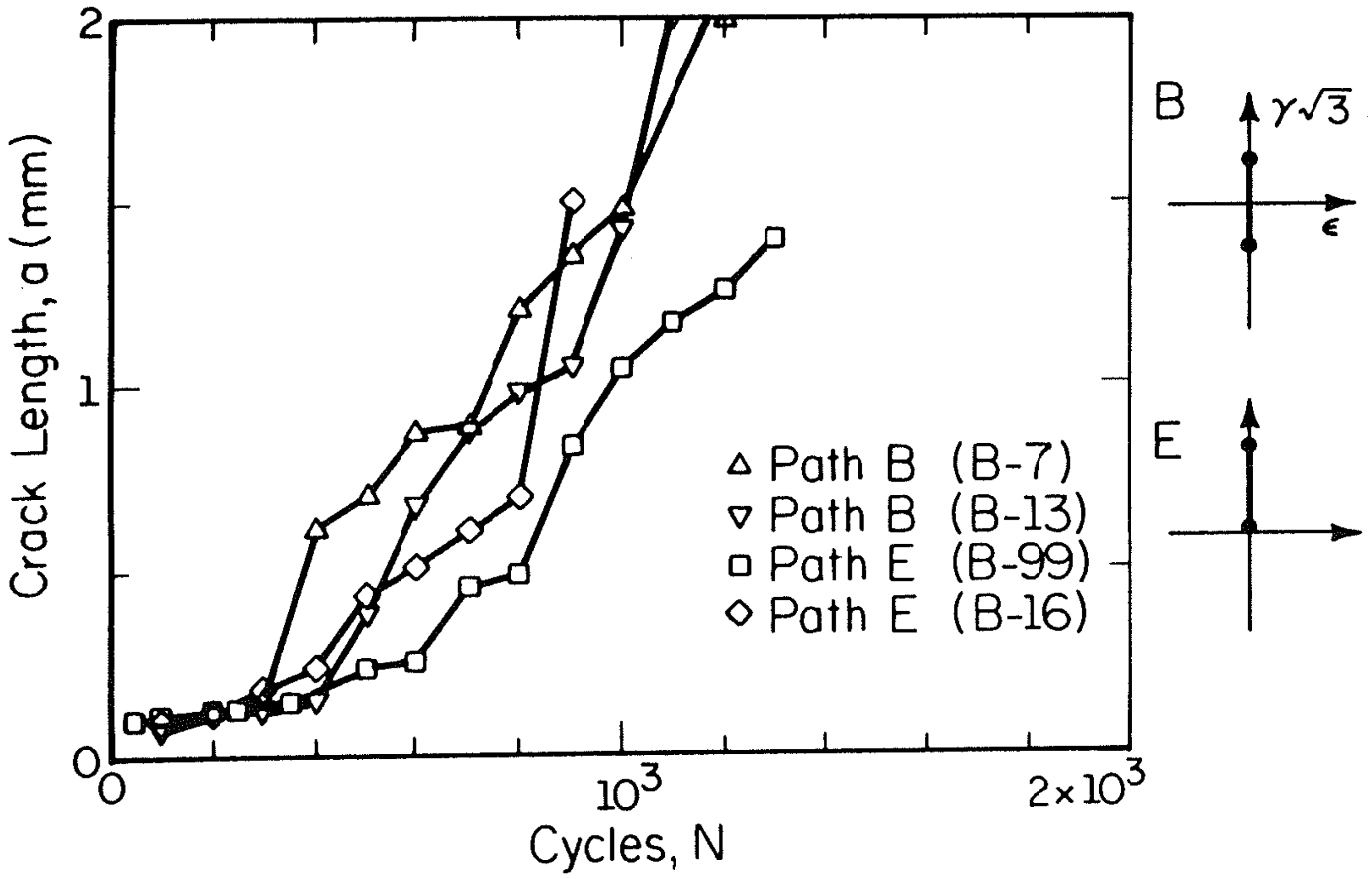

Figure E.5 Strain Paths B and E, $\bar{\epsilon} = 0.010$

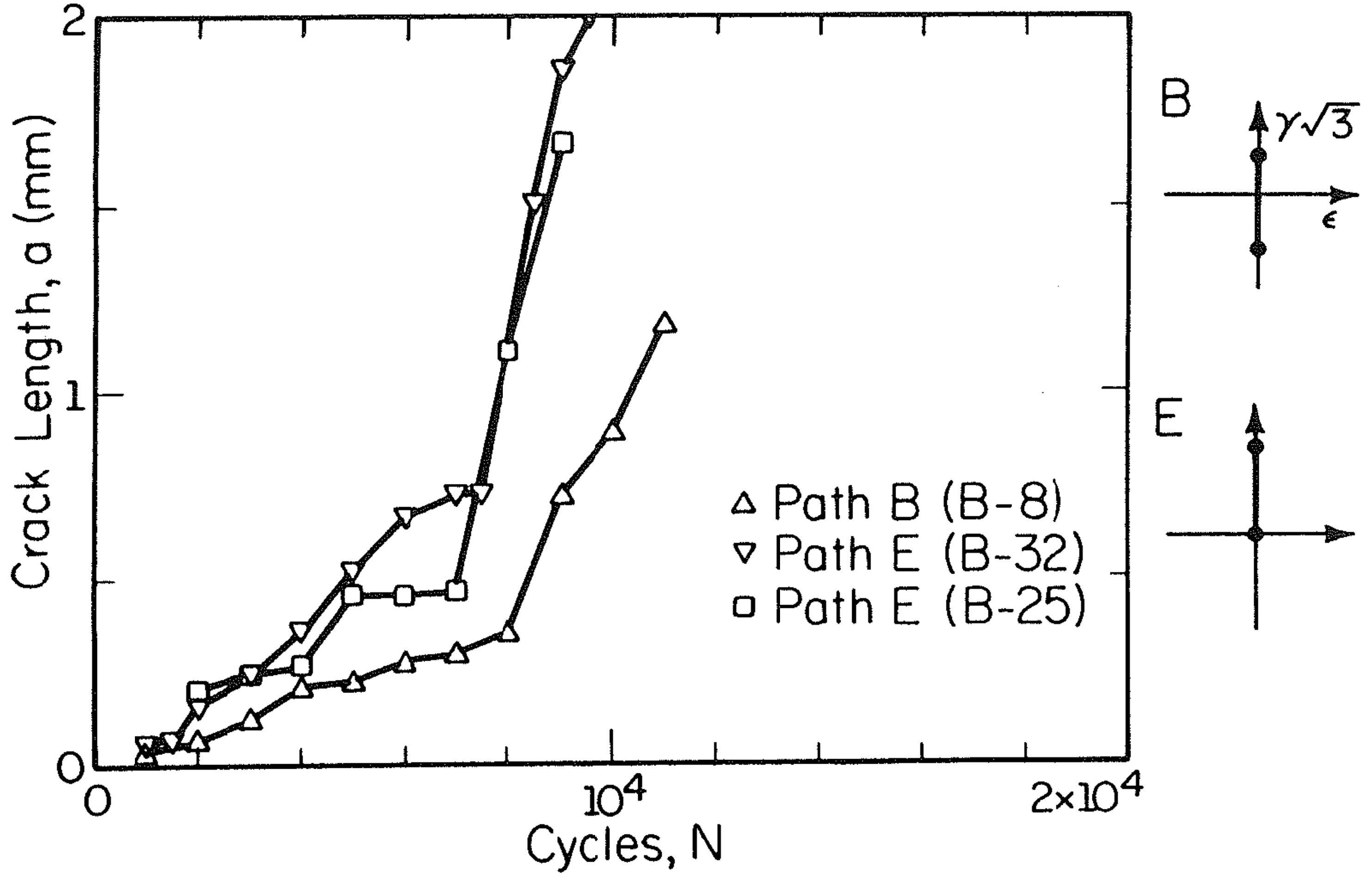

Figure E.6 Strain Paths B and E, $\bar{\varepsilon} = 0.005$

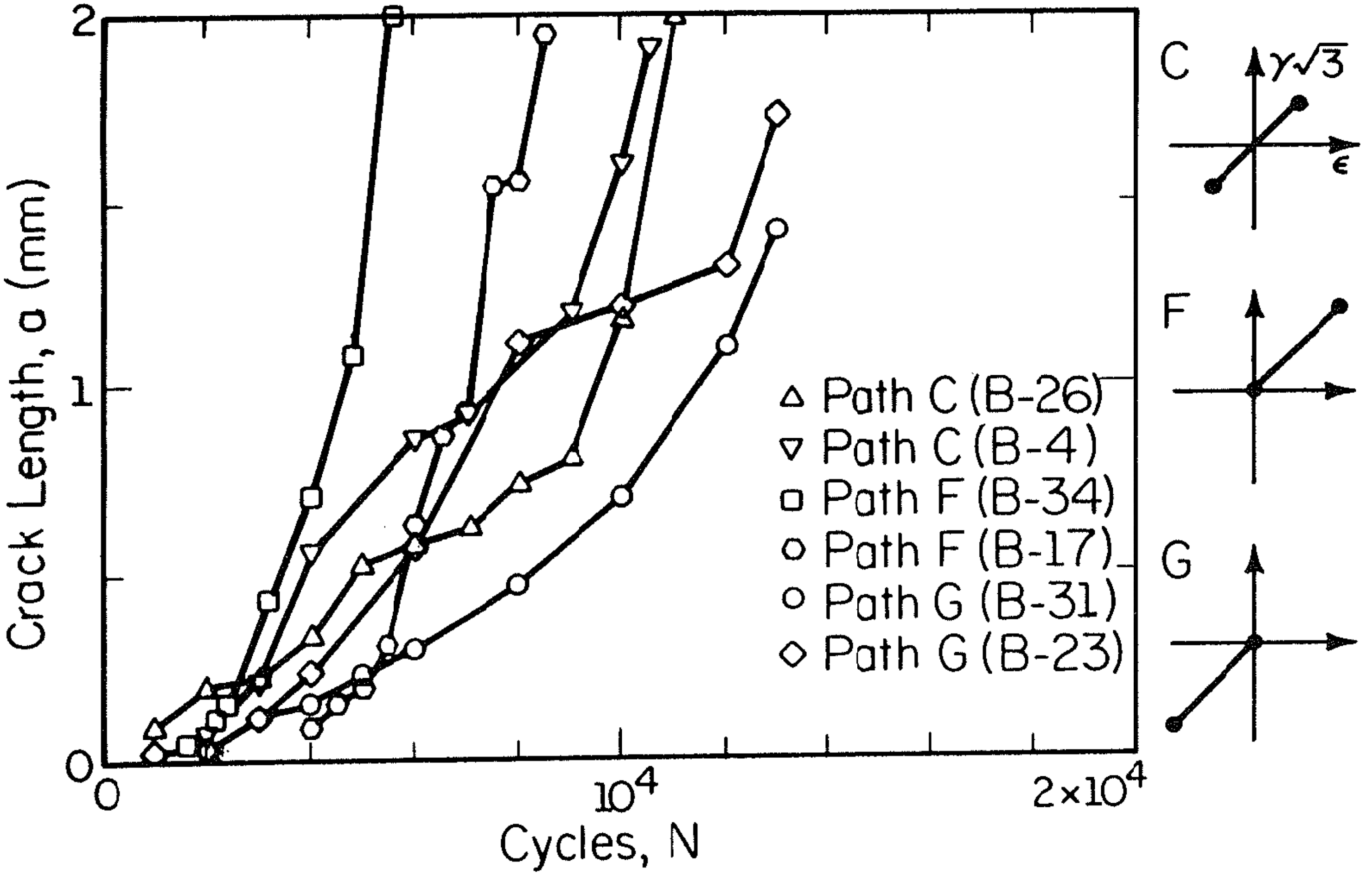

Figure E.7 Strain Paths C, F, and G, $\bar{\varepsilon} = 0.005$

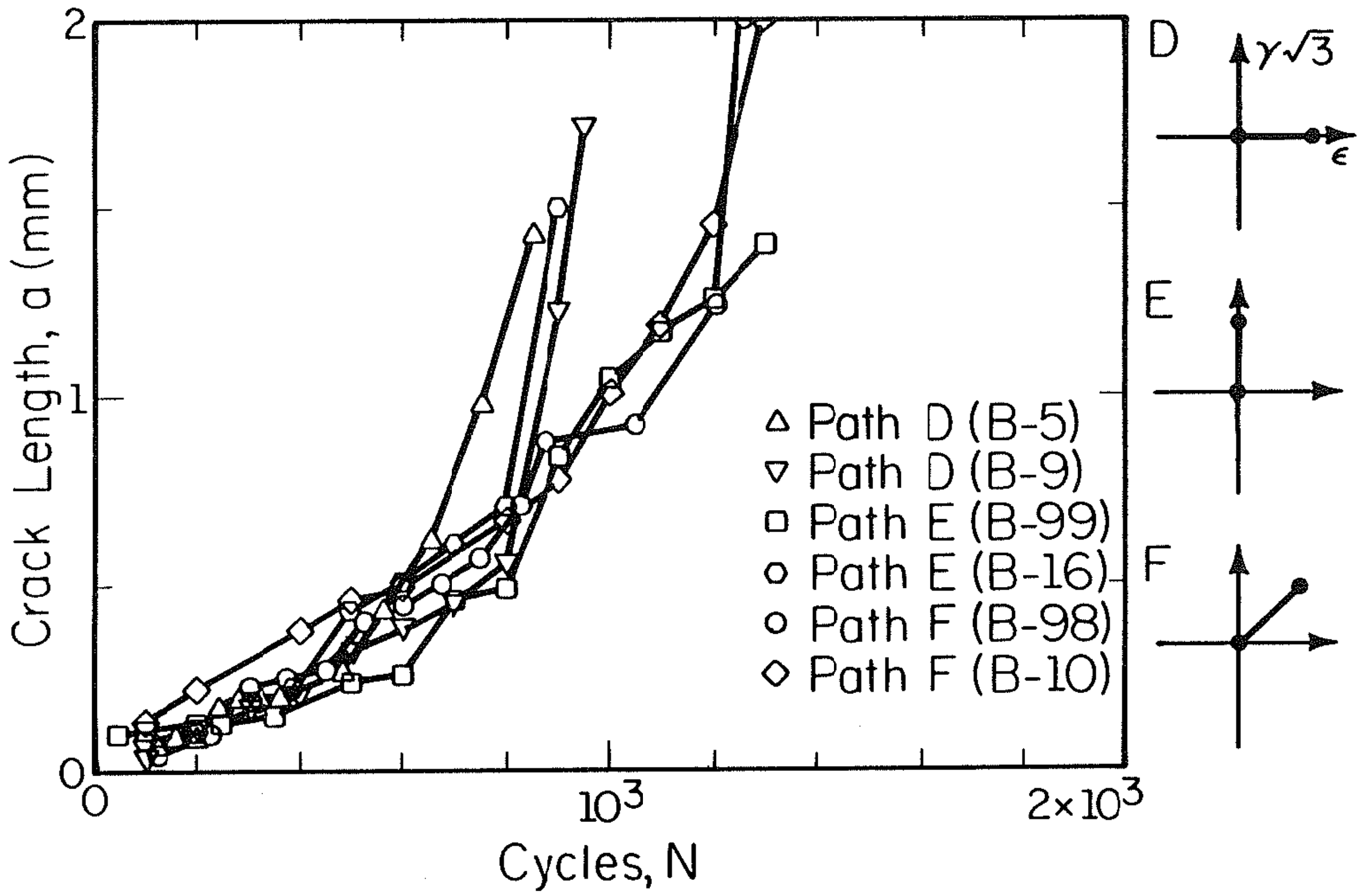

Figure E.8 Strain Paths D, E, and F, $\bar{\epsilon}$ = 0.010

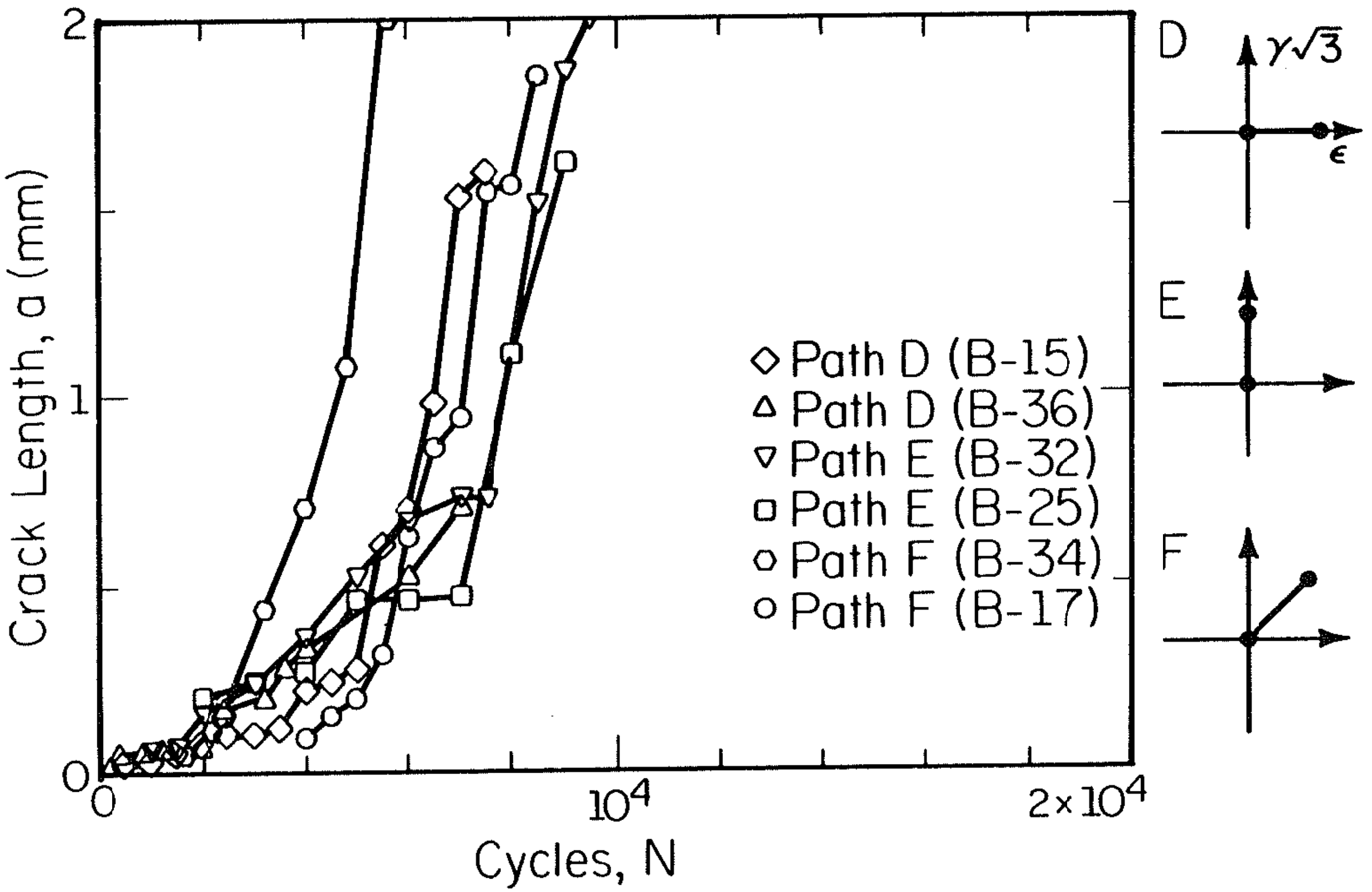

Figure E.9 Strain Paths D, E, and F, $\bar{\epsilon} = 0.005$

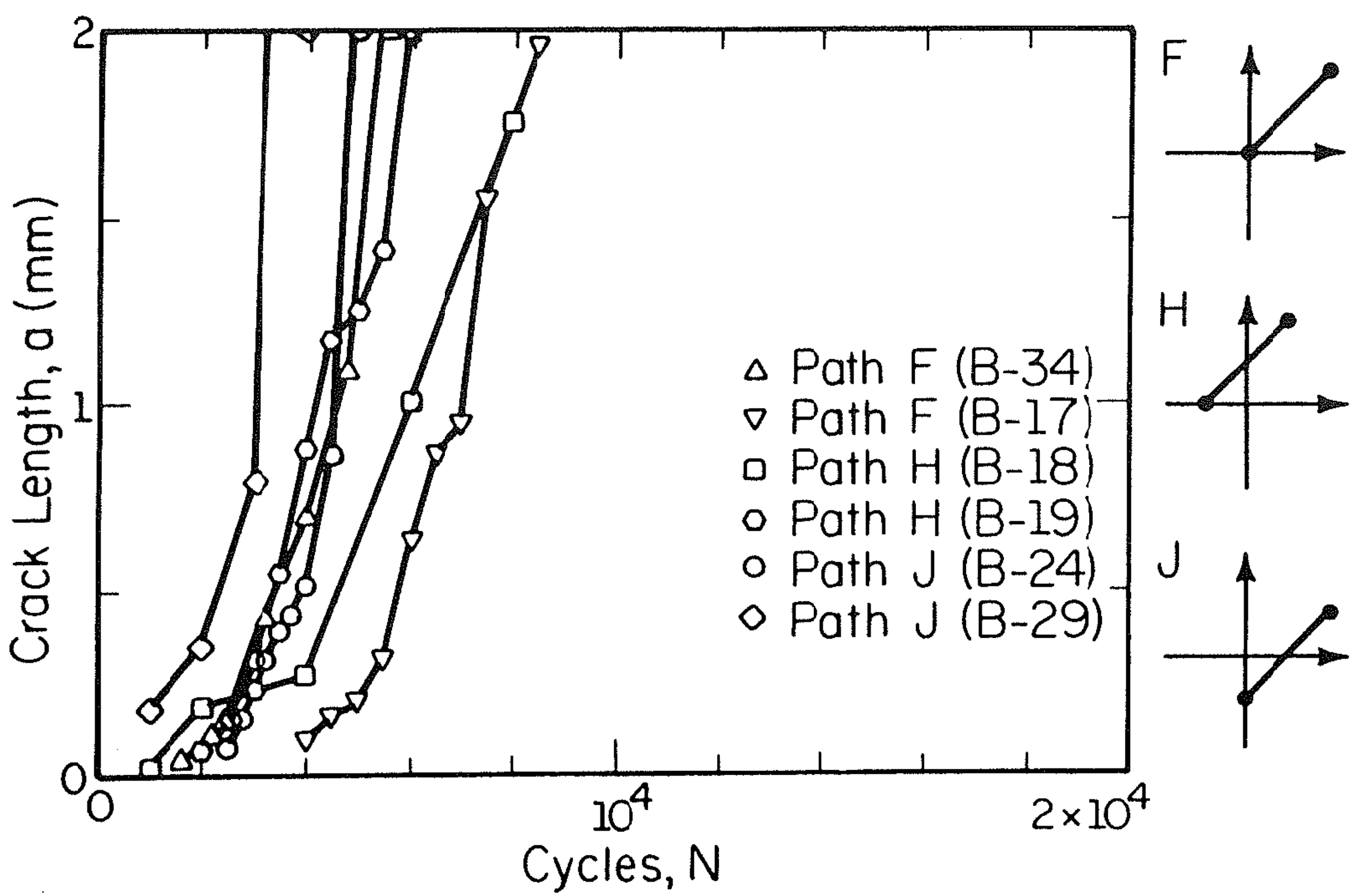

Figure E.10 Strain Paths F, H, and J, $\overline{\varepsilon} = 0.005$

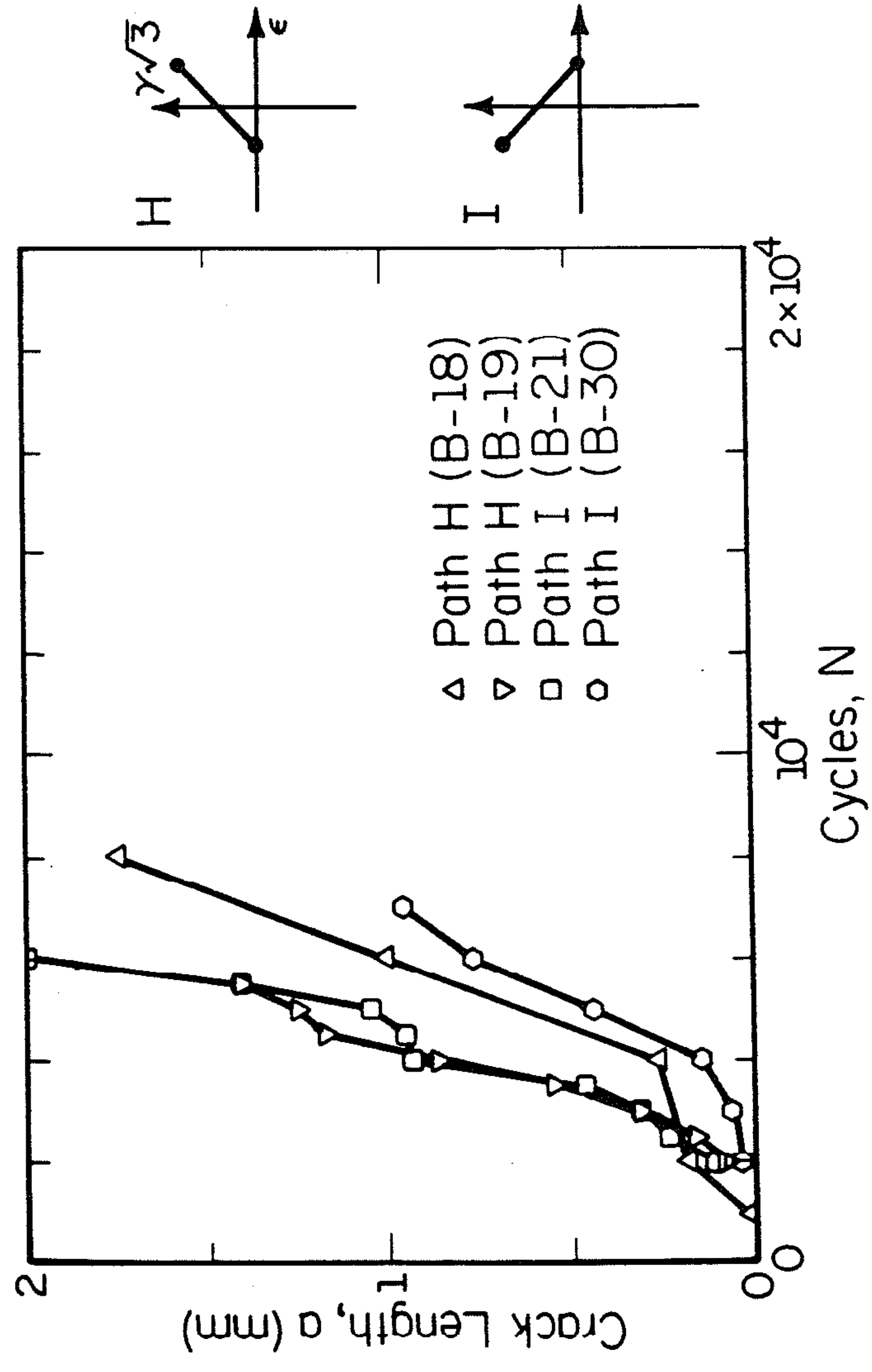

Figure E.11 Strain Paths H and I, $\bar{\varepsilon} = 0.005$

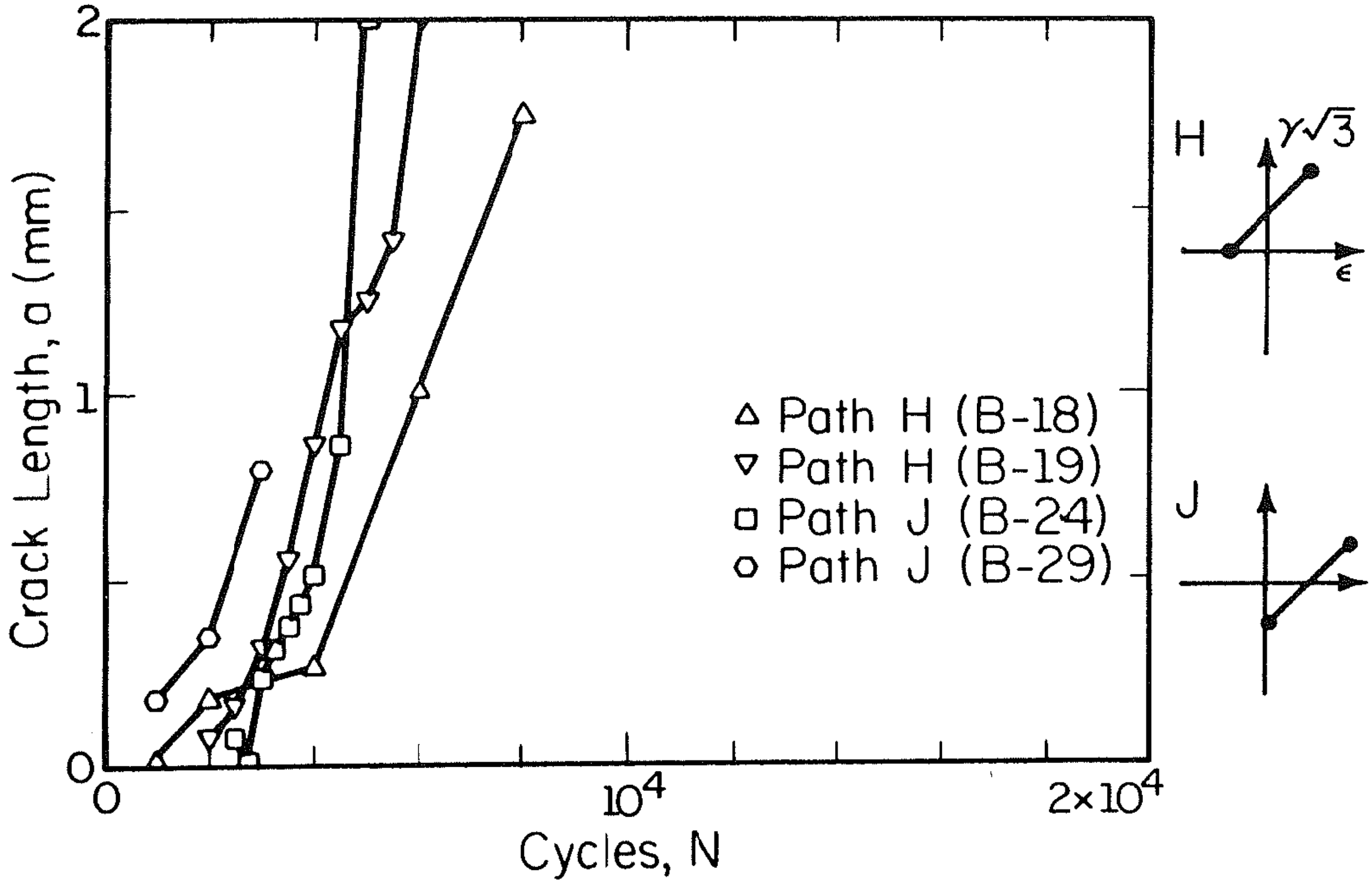

Figure E.12 Strain Paths H and J, $\bar{\epsilon} = 0.005$

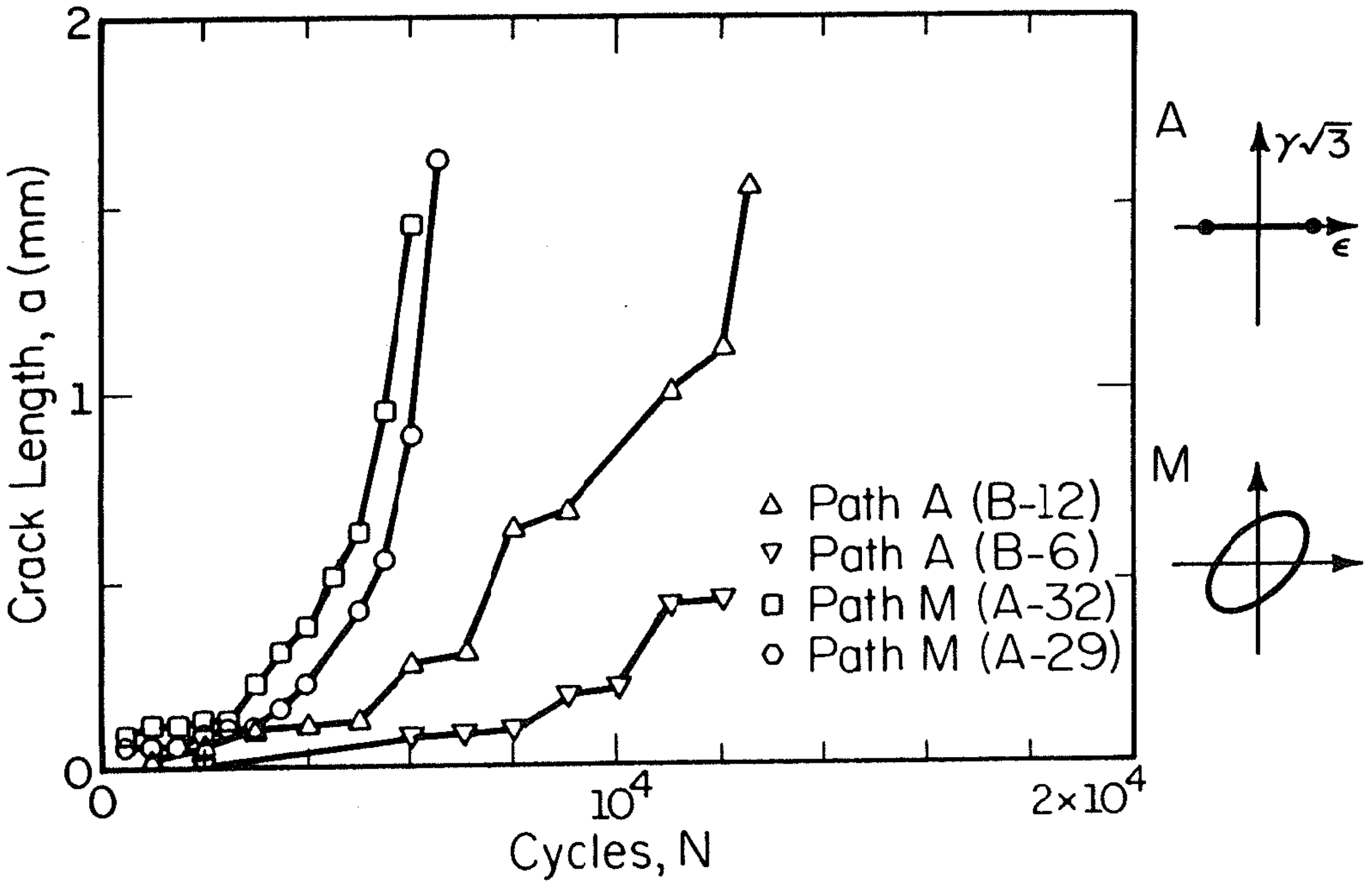

Figure E.13 Strain Paths A and M, $\bar{\epsilon}$ = 0.005

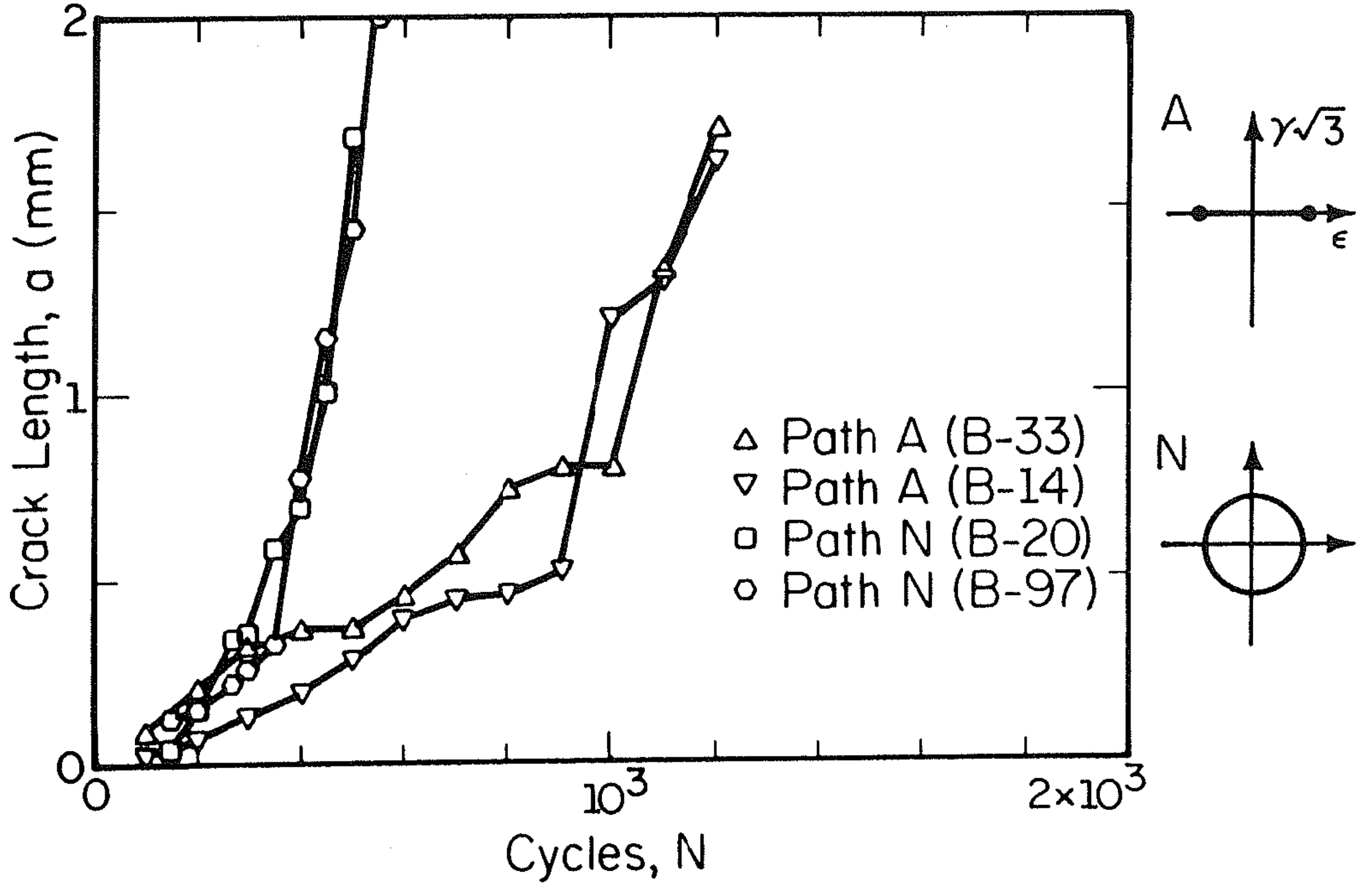

Figure E.14 Strain Paths A and N, $\bar{\varepsilon} = 0.010$

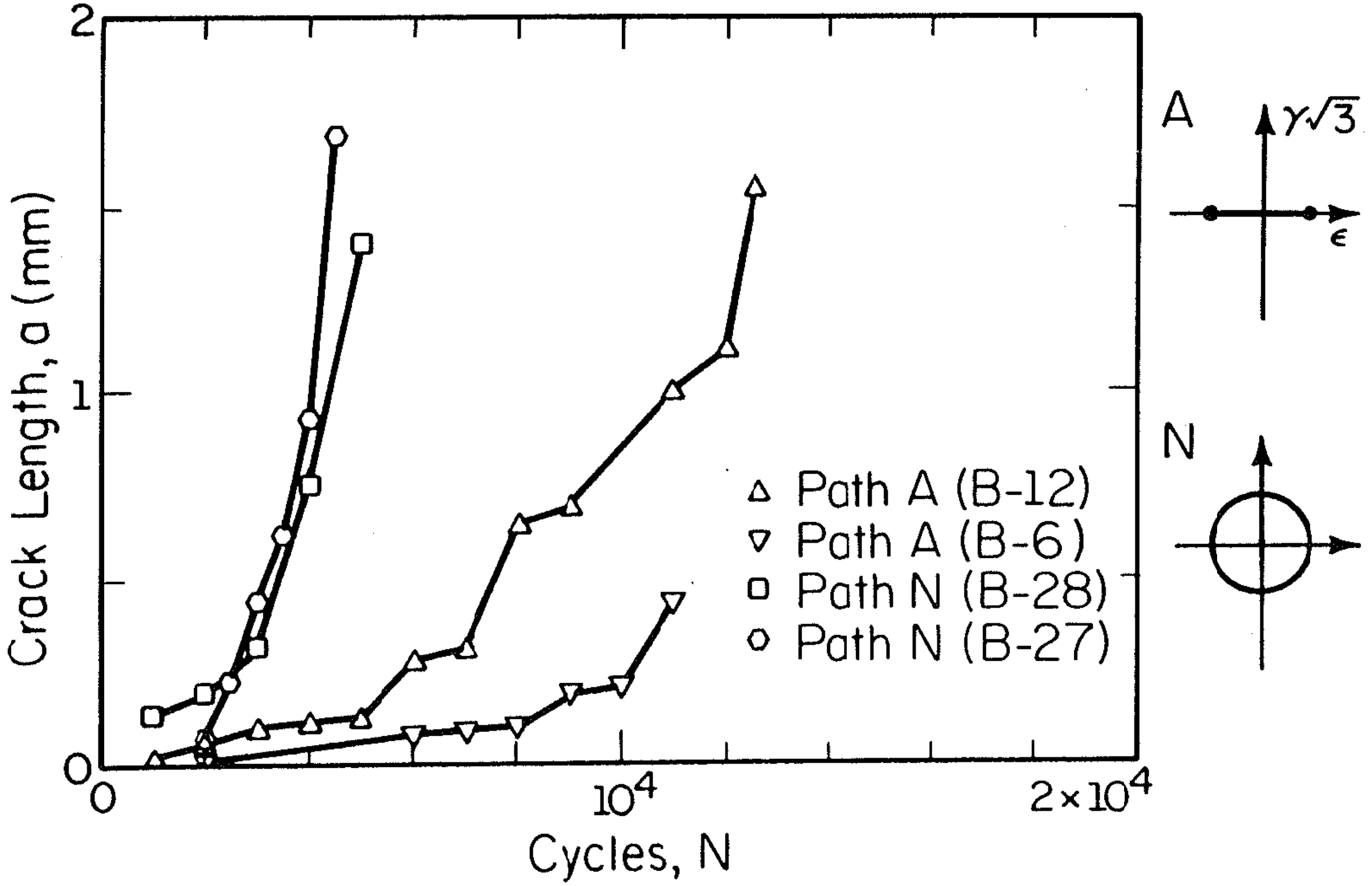

Figure E.15 Strain Paths A and N, $\bar{\varepsilon} = 0.005$

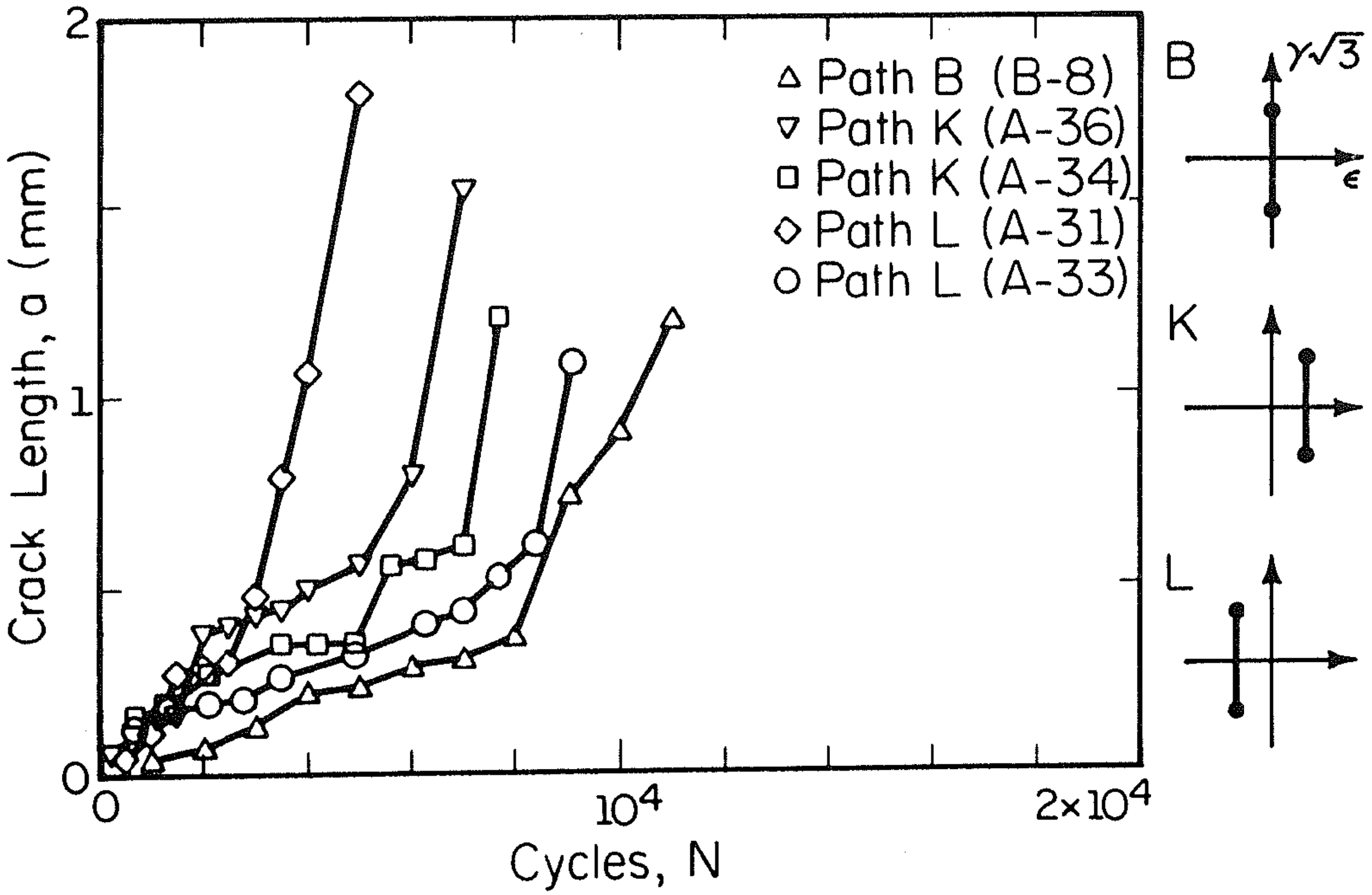

Figure E.16 Strain Paths B, K, and L, $\bar{\varepsilon} = 0.005$

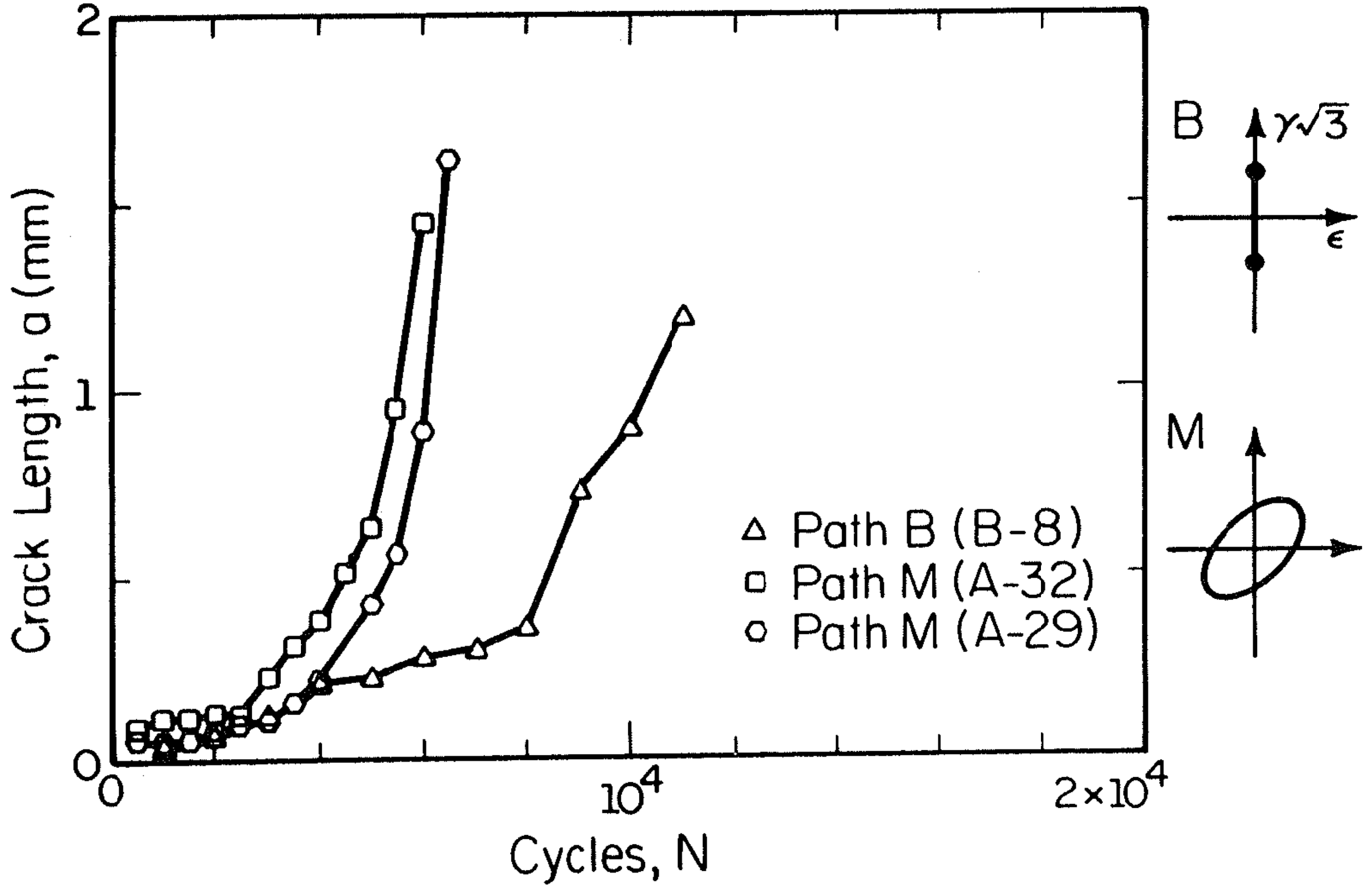

Figure E.17 Strain Paths B and M, $\bar{\epsilon} = 0.005$

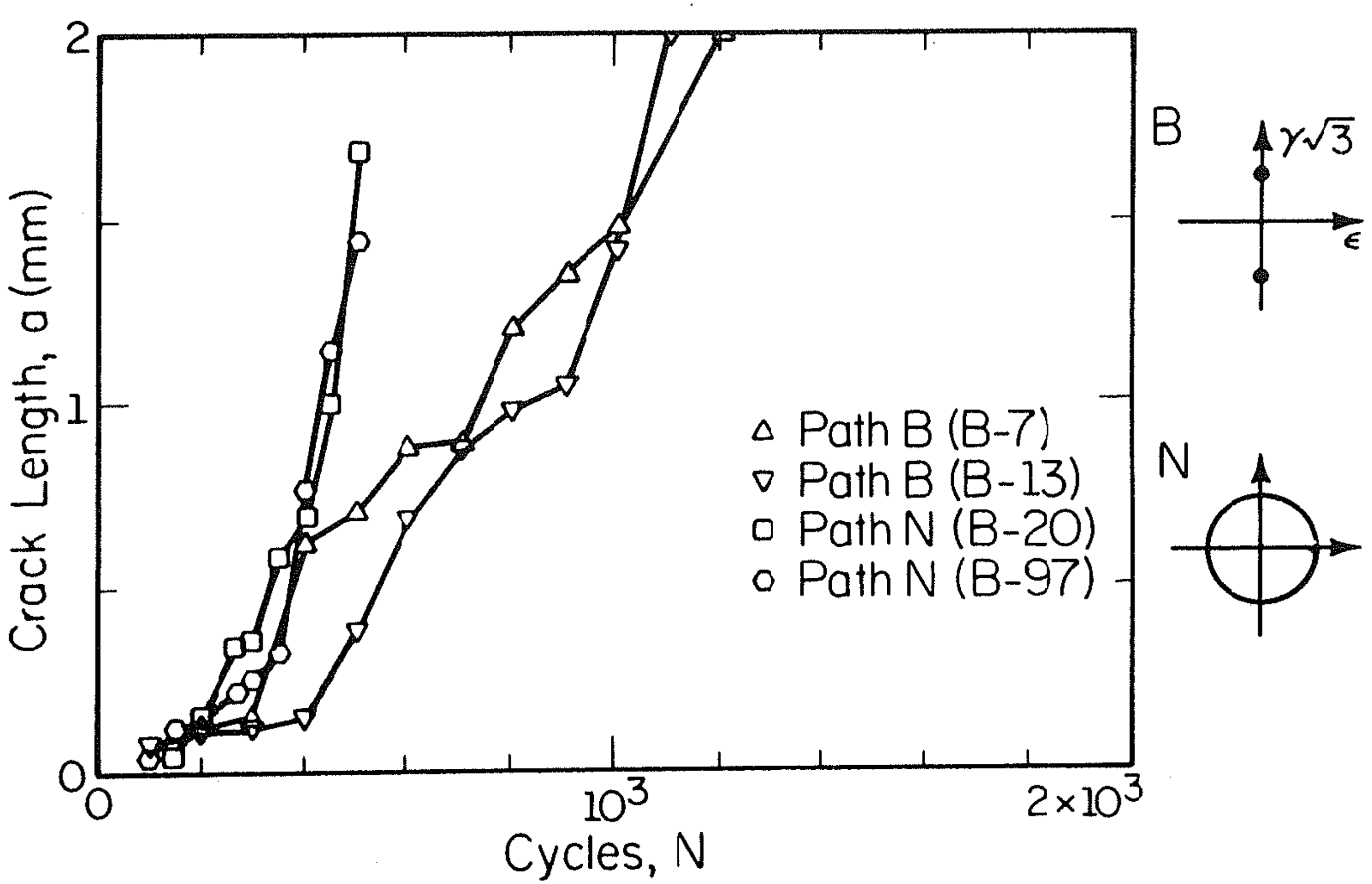

Figure E.18 Strain Paths B and N, $\overline{\epsilon}$ = 0.010

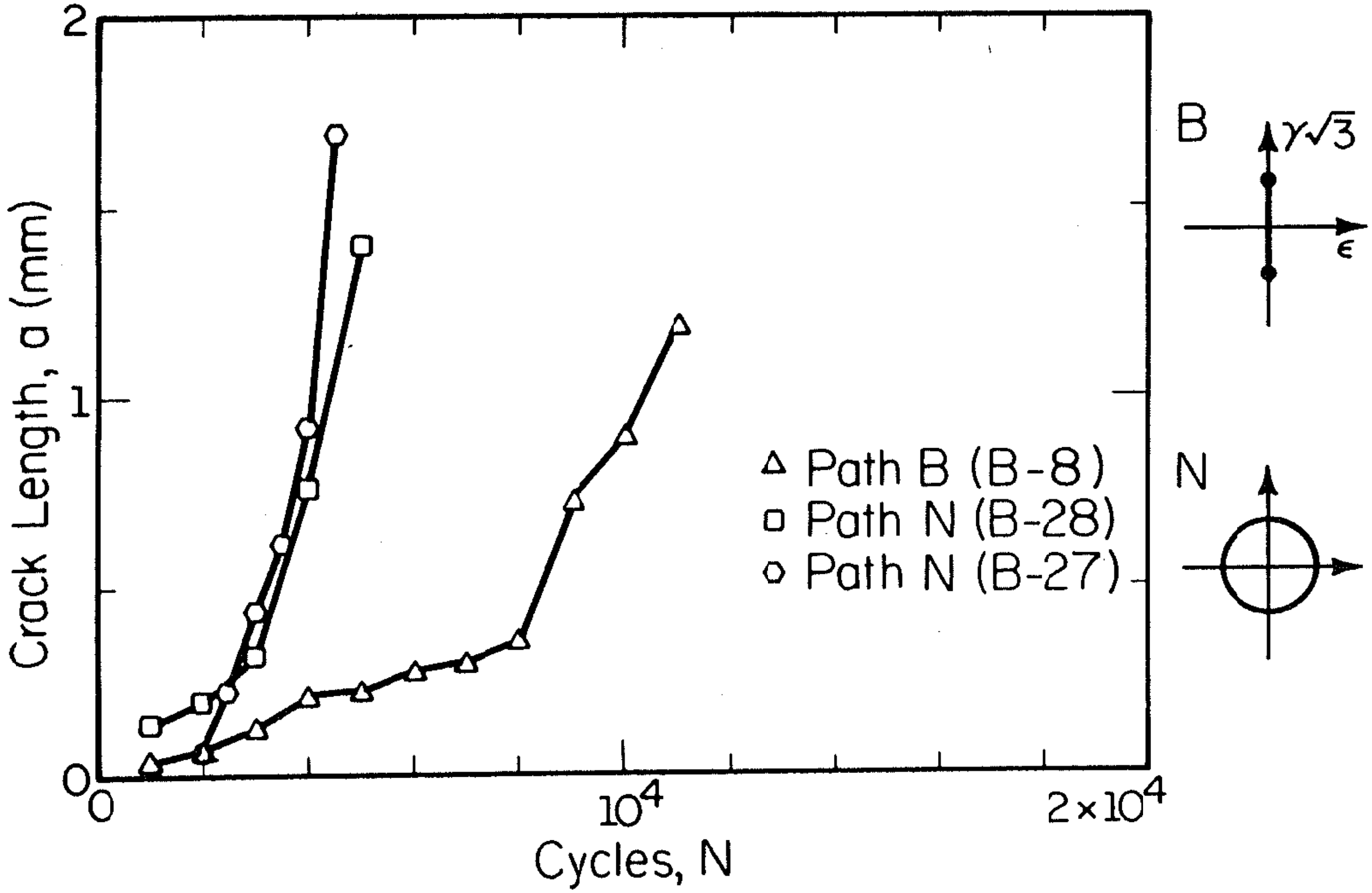

Figure E.19 Strain Paths B and N, $\bar{\epsilon} = 0.005$

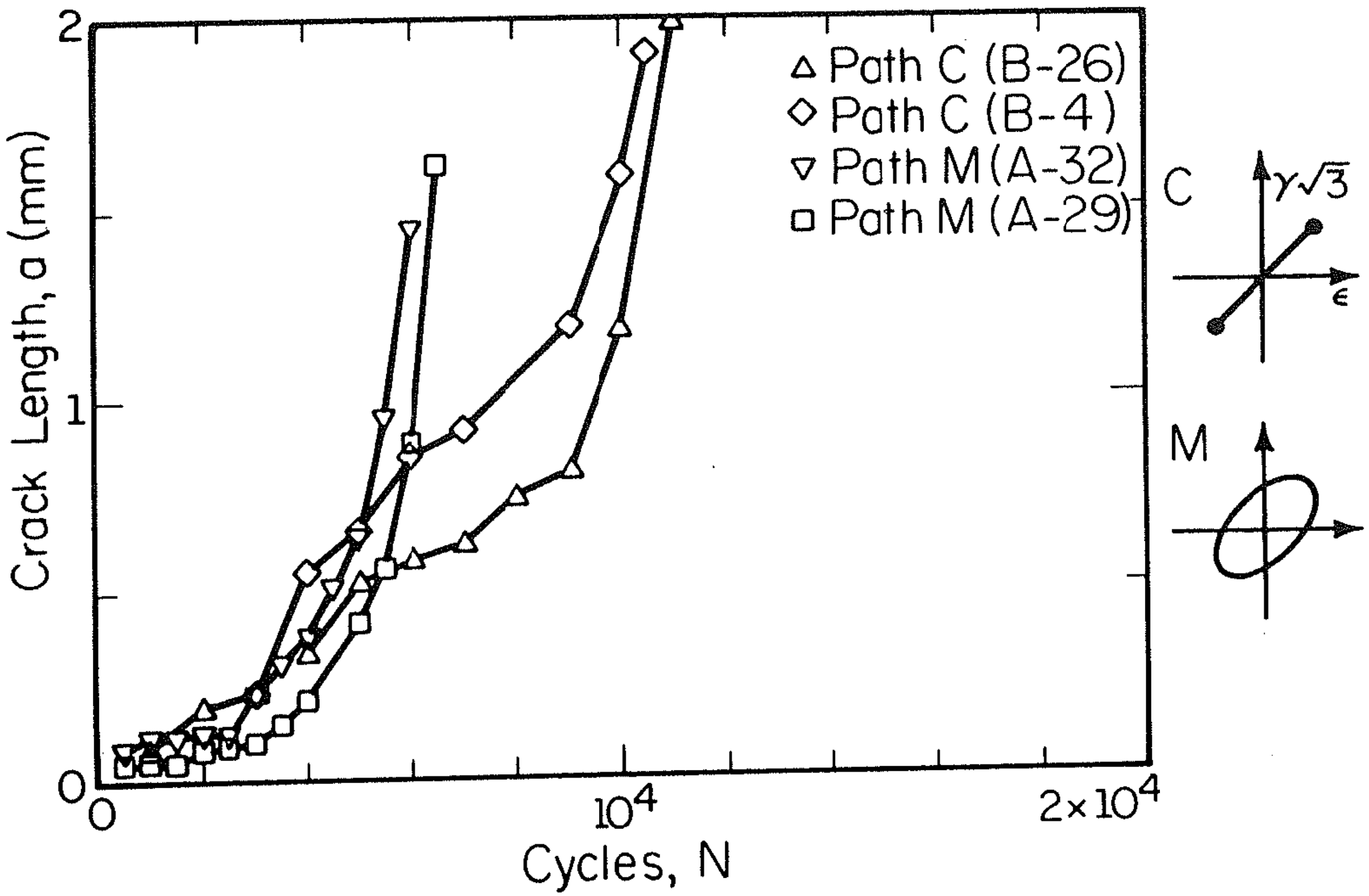

Figure E.20 Strain Paths C and M, $\bar{\epsilon}$ = 0.005

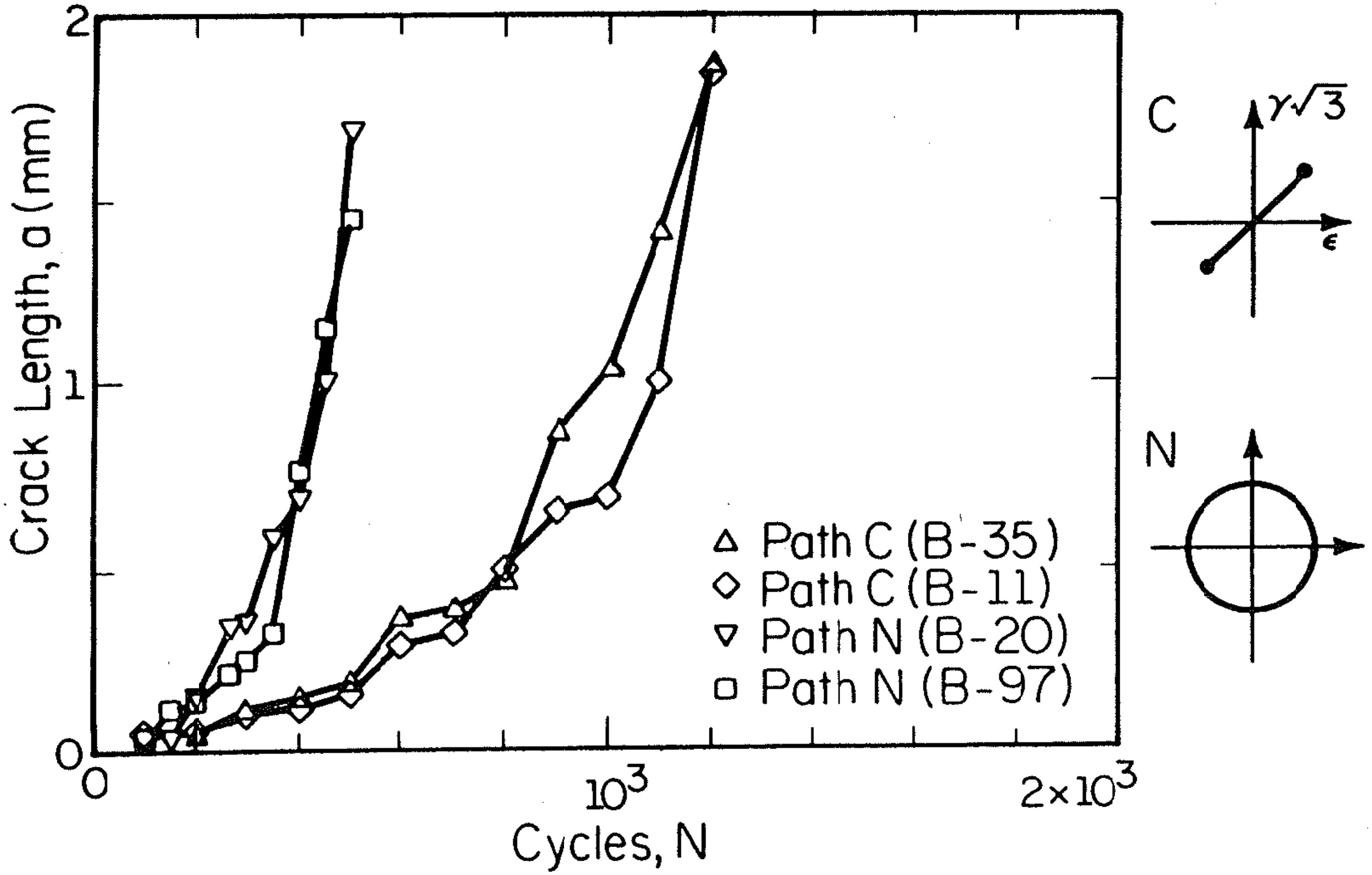

Figure E.21 Strain Paths C and N, $\bar{\epsilon} = 0.010$

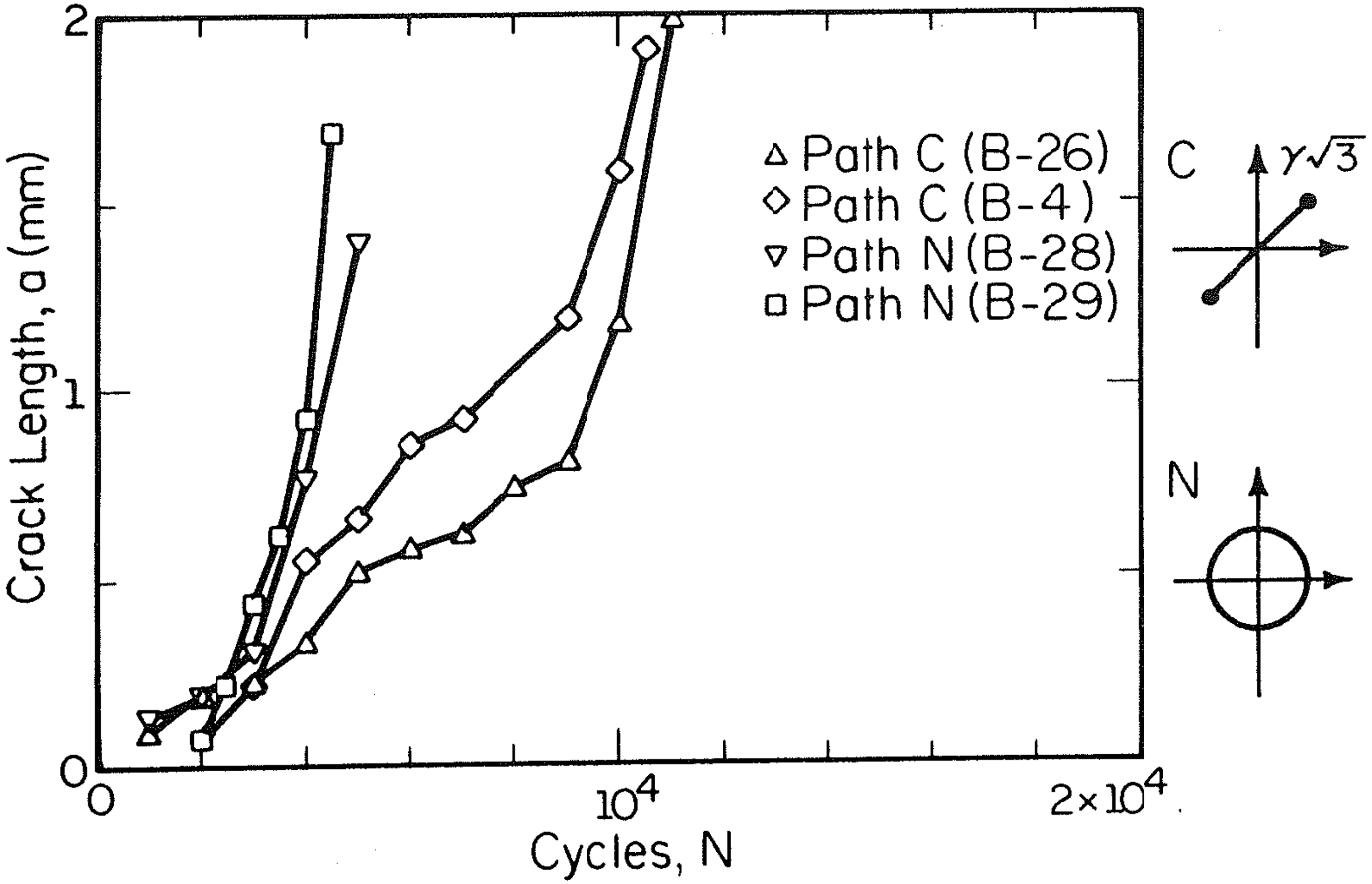

Figure E.22 Strain Paths C and N, $\overline{\varepsilon} = 0.005$

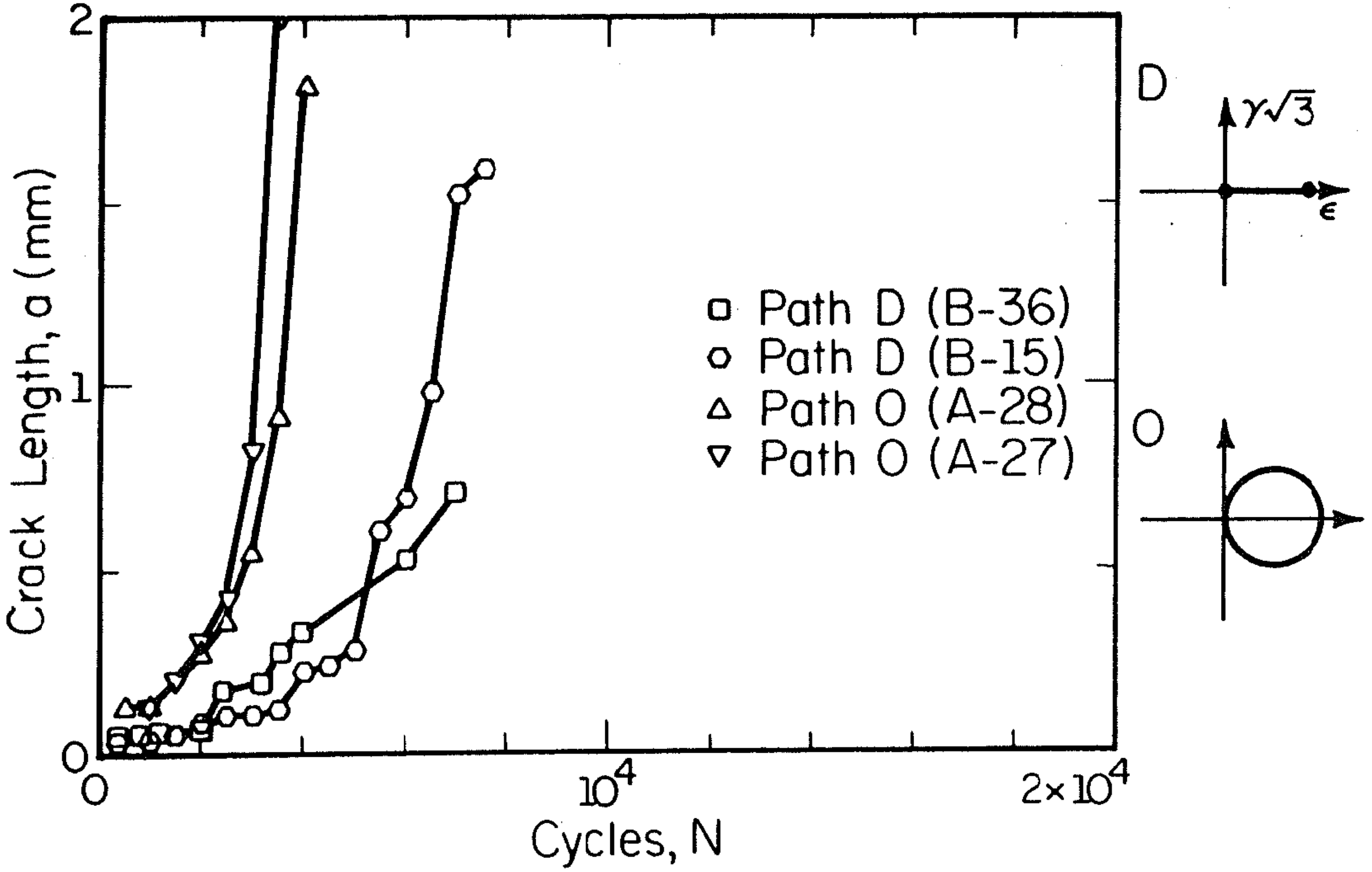

Figure E.23 Strain Paths D and O, $\bar{\epsilon}$ = 0.005

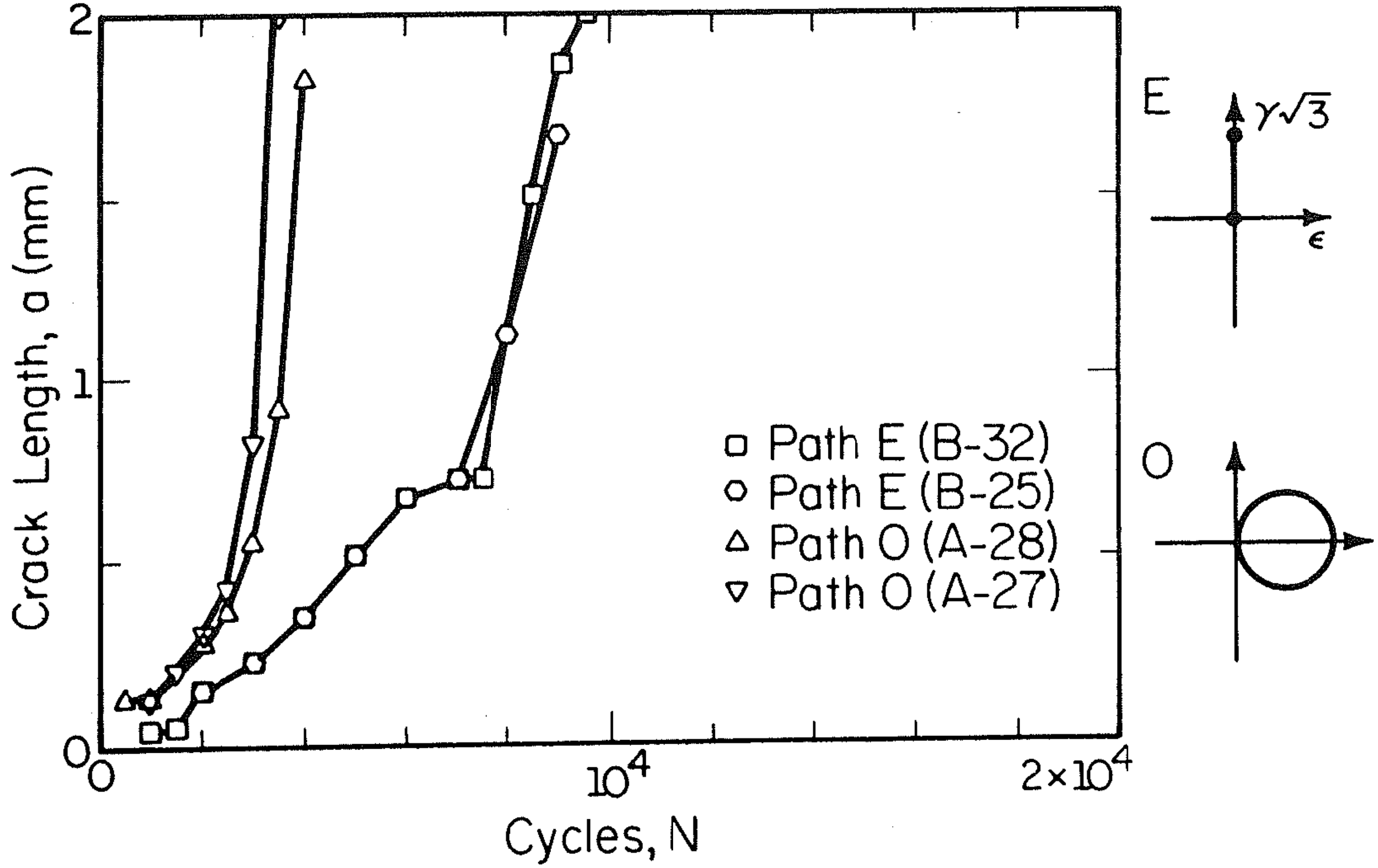

Figure E.24 Strain Paths E and O, $\overline{\epsilon}$ = 0.005

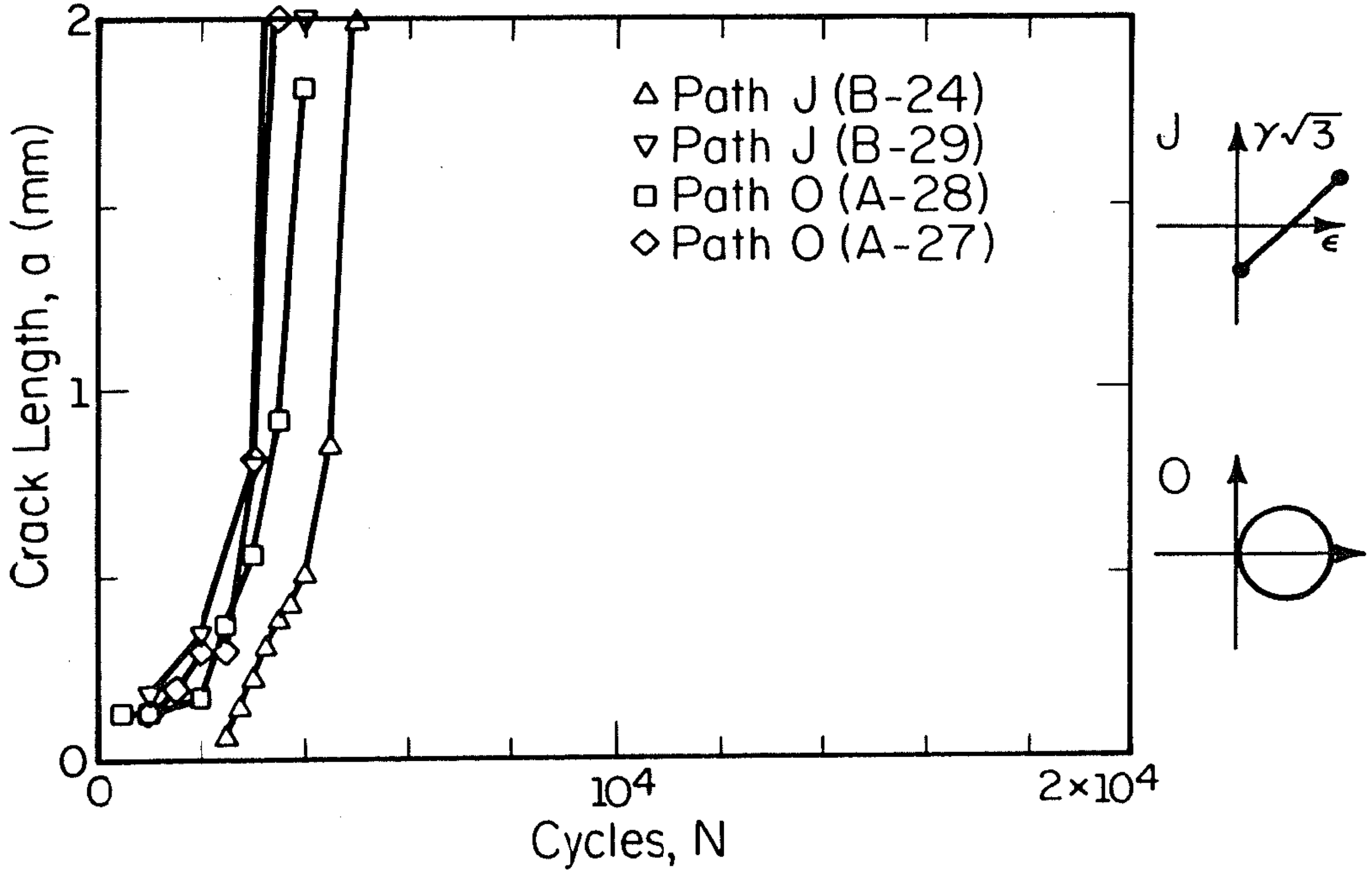

Figure E.25 Strain Paths J and O, $\bar{\varepsilon} = 0.005$

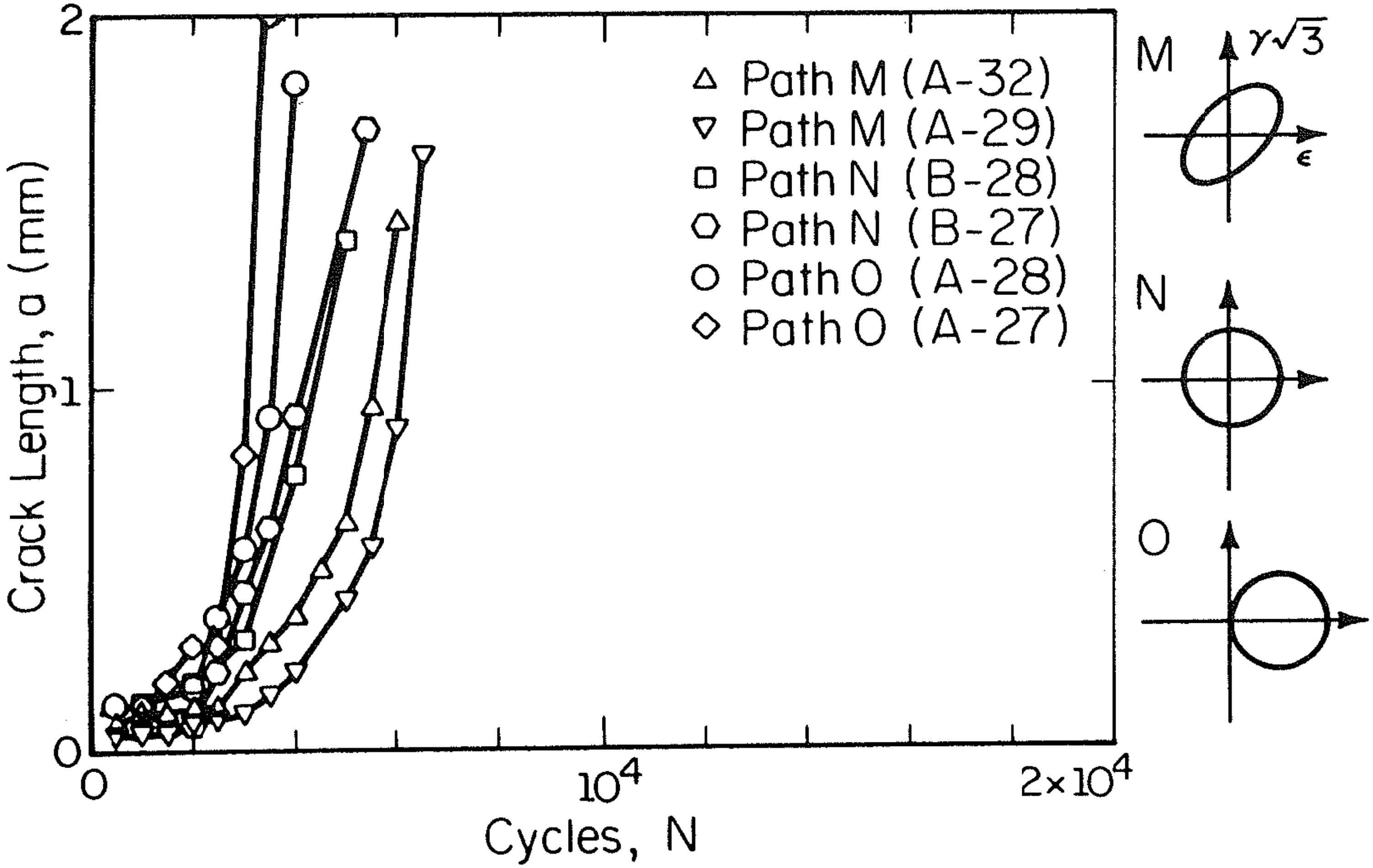

Figure E.26 Strain Paths M, N, and O, $\overline{\epsilon} = 0.005$

REFERENCES

1. Garud, Y. S., "Multiaxial Fatigue: A Survey of the State-of-the-Art," J. of Testing Evaluation, American Society for Materials and Testing, Vol. 9, No. 3, 1981, pp. 165-178.

2. Brown, M. W., and Miller, K. J., "A Theory for Fatigue under Multi-Axial Stress-Strain Conditions," Proc., Inst. Mech. Engr., Vol. 187, 1973, pp. 746-755.

3. Krempl, E., The Influence of State of Stress on Low Cycle Fatigue of Structural Materials, ASTM, STP 549, American Society for Testing and Materials, 1974, 46 pp.

4. Coffin, L. F., Jr., "A Study of Cyclic Thermal Stresses on a Ductile Metal," Trans. ASME, Vol. 76, 1954, pp. 931-950.

5. Manson, S. S., "Behavior of Materials under Conditions of Thermal Stresses," Proc., Heat Transfer Symposium, University of Michigan Engineering Research Institute, 1953, pp. 9-75.

6. Ewing, J. A., and J.C.W. Humphrey, "The Fracture of Metals and Repeated Alternations of Stress," Philosophical Trans. of the Royal Society of London, Series A, Vol. 200, 1903, Part 1, pp. 241-250.

7. Forsyth, P.J.E, "A Two-Stage Process of Fatigue Crack Growth," Proc., Crack Propagation Symp., Cranfield, 1961, pp. 76-94.

8. Miller, K. J., "Initiation and Growth Rates of Short Fatigue Cracks," unpublished manuscript, 1984, 24 pp.

9. Kurath, P., Socie, D. F., and Morrow, J., "A Non-arbitrary Fatigue Crack Size Concept to Predict Total Fatigue Lives," Technical Report AFDL-TR-79-3144, Air Force Flight Dynamics Laboratory, Wright-Patterson AFD, Ohio, December, 1979.

10. Dowling, N. E., "Notched Member Fatigue Life Predictions Combining Crack Initiation and Propagation," Fatigue of Engineering Materials and Structures, Vol. 2, No. 2, 1979, pp. 129-138.

11. Smith, R. A., and Miller, K. J., "Prediction of Fatigue Regimes in Notched Comments," Int. J. of Mech. Science, Vol. 20, 1978, pp. 201-206.

12. Kurath, P., and Socie, D. F., unpublished data.

13. Fash, J. W., "Fatigue Crack Initiation and Growth in Gray Cast Iron," Fracture Control Program, Report No. 35, College of Engineering, University of Illinois, 1980, pp. 47-50.

14. Waill, L. E., "Crack Observations in Biaxial Fatigue," M.S. Thesis, Department of Mechanical Engineering, University of Illinois at Urbana-Champaign, Urbana, IL, 1983, 61 pp.

15. Nadia. A., Plasticity, A Mechanics of the Plastic State of Matter, McGraw-Hill Book Co., Inc., New York, 1931.

16. Findley, W. N., P. N. Mather, and D. E. Martin, "Fatigue Failure under Combinations of Stresses," Theoretical and Applied Mechanics Report No. 61, University of Illinois, 1954.

17. Orowan, E., Dislocations in Metals, The American Institute of Mining and Metallurgical Engineers, Inc., New York, NY, 1954, pp. 188-194.

18. Kandil, F. A., Brown, M. W., and Miller, K. J., "Biaxial Low-Cycle Fatigue Fracture of 316 Stainless Steel at Elevated Temperatures," Vol. 280, The Metals Society, London, 1982, pp. 203-210.

19. Lohr, R. P., and Ellison, E. G., "A Simple Theory for Low Cycle Multiaxial Fatigue," Fatigue of Engineering Materials and Structures, Vol. 3, 1980, pp. 1-17.

20. Socie, D. F., Waill L. A., and Dittmer, D. F., "Biaxial Fatigue of Inconel 718 including Mean Stress Effects," ASTM STP 853, 1984.

21. Socie, D. F., and Shield, T. W., "Mean Stress Effects in Biaxial Fatigue of Inconel 718," J. of Engineering Materials and Technology, Vol. 106, 1984, pp. 227-232.

22. Peterson, R. F., "Fatigue Cracks and Fracture Surfaces--Mechanics of Development and Visual Appearance," Chap. 14, Metal Fatigue, G. Sines and J. L. Waesman, editors, McGraw-Hill Book Co., Inc., New York, 1959, pp. 68-86.

22. Sines, G., "Behavior of Metals under Complex Static and Alternating Stresses," Metal Fatigue, Engineering Extension Series, University of California, 1959, pp. 145-169.

23. Beer, T. A., "Crack Slopes During Biaxial Fatigue," M.S. Thesis, Department of Mechanical Engineering, University of Illinois at Urbana-Champaign, Urbana, IL, 1984, 69 pp.